

LA-7686-MS

Informal Report

c.3

CIC-14 REPORT COLLECTION

**REPRODUCTION
COPY**

**A Conceptual Design of the Fast-Liner
Reactor (FLR) for Fusion Power**

University of California



LOS ALAMOS SCIENTIFIC LABORATORY

Post Office Box 1663 Los Alamos, New Mexico 87545

This work was supported by the Electric Power
Research Institute.

This report was prepared as an account of work sponsored by the United States Government. Neither the United States nor the United States Department of Energy, nor any of their employees, nor any of their contractors, subcontractors, or their employees, makes any warranty, express or implied, or assumes any legal liability or responsibility for the accuracy, completeness, or usefulness of any information, apparatus, product, or process disclosed, or represents that its use would not infringe privately owned rights.

OFFICE MEMORANDUM

TO : Holders of LA-7686-MS

DATE April 6, 1979

FROM : ISD-6 Editorial Section

SUBJECT : Erratum

SYMBOL :

MAIL STOP: 188

Please substitute the attached title page in the above report.



LA-7686-MS
Informal Report
UC-20d
Issued: February 1979

A Conceptual Design of the Fast-Liner Reactor (FLR) for Fusion Power

**R. W. Moses
R. A. Krakowski
R. L. Miller**

MAJOR CONTRIBUTORS

G. E. Cort (heat transfer), R. A. Gerwin (physics), R. L. Hagenson (plasma engineering, costing), J. D. Jacobson (blast confinement), T. R. Jarboe (physics), R. C. Malone (physics), T. A. Oliphant (numerical techniques), P. D. Soran (neutronics), and C. E. Swannack (energy storage and transfer).

This work was supported by the US Department of Energy, Office of Fusion Energy, and in part by the Electric Power Research Institute.



LA-7686-MS
Informal Report
UC-20d
Issued: February 1979

A Conceptual Design of the Fast-Liner Reactor (FLR) for Fusion Power

R. W. Moses
R. A. Krakowski
R. L. Miller



CONTENTS

ABSTRACT	1
I. INTRODUCTION AND SUMMARY	1
II. SUMMARY DESCRIPTION OF REACTOR OPERATION	3
III. PHYSICS AND TECHNOLOGY DESIGN BASES	7
A. Reactor Physics	7
1. Plasma Model	7
a. Radial Transport	9
b. Axial Transport	10
c. Burn Dynamics	11
2. Liner Model	11
a. Stability	12
b. Dynamics	13
3. Numerical Methods	14
4. Development of Physics Operating Point	14
B. Reactor Engineering/Technology	20
1. Energy Balance	21
2. Plasma Preparation	23
3. Energy Storage, Switching, and Transfer	24
4. Liner Leads	26
5. Neutronics Analysis	32
6. Blast Containment	39
7. Heat Transfer	46
C. Costing Model	50
D. Design Point	52
IV. PRESENT KNOWLEDGE IN PHYSICS AND TECHNOLOGY	65
A. Physics Confidence	67
1. Plasma Preparation	67
2. Transport	67
3. Liner	68
B. Technology	68
1. Liner/Leads Fabrication	68
2. Plasma Preparation	70
3. Containment	70
4. Energy Transfer and Storage	71
5. Leads/Liner Replacement	71
6. Primary Heat-Transfer System	72
V. SUMMARY CONCLUSIONS	73
ACKNOWLEDGMENTS	74
APPENDIXES (Including Tables and Figures)	75
A. Description of LNRBRN Code	75
B. Optimization of Coaxial Leads Structure	78
C. Optimization of Interleaved Leads Structure	88

D. Description MCNP Monte Carlo Calculation	93
E. Use of the Virial Theorem and a Simple Shock Model to Estimate Blast Effects in Vacuum and Two-Phase Media	95
F. Costing Guidelines, Accounting System, and Data Base	107
REFERENCES	120

A CONCEPTUAL DESIGN OF THE FAST-LINER
REACTOR (FLR) FOR FUSION POWER

by ¹⁹⁶³

R. W. Moses, R. A. Krakowski, and R. L. Miller

ABSTRACT

The generation of fusion power from the Fast-Liner Reactor (FLR) concept envisages the implosion of a thin (3-mm) metallic cylinder (0.2-m radius by 0.2-m length) onto a preinjected plasma. This plasma would be heated to thermonuclear temperatures by adiabatic compression, pressure confinement would be provided by the liner inertia, and thermal insulation of the wall-confined plasma would be established by an embedded azimuthal magnetic field. A 2-to 3- μ s burn would follow the $\sim 10^4$ m/s radial implosion and would result in a thermonuclear yield equal to 10-15 times the energy initially invested into the liner kinetic energy. For implosions occurring once every 10 s a gross thermal power of 430 MWt would be generated. The results of a comprehensive systems study of both physics and technology (economics) optima are presented. Despite unresolved problems associated with both the physics and technology of the FLR, a conceptual power plant design is presented.

I. INTRODUCTION AND SUMMARY

The use of magnetically driven, metallic liners for the adiabatic compression of D-T plasmas to thermonuclear conditions has been studied by a number of investigators.¹⁻⁴ The largest imploding-liner programs to date have been at the Kurchatov Institute in the USSR² and at the Naval Research Laboratory (NRL) in the United States.³ The approach taken by the Kurchatov group has emphasized fast (10^3 - 10^4 m/s) implosions of thin metal shells in a variety of configurations, whereas the NRL group has been concerned primarily with slower ($\sim 10^2$ m/s) implosions of more massive, cylindrical systems. The

Los Alamos Scientific Laboratory has proposed⁵ and is conducting experiments on $\sim 10^4$ m/s imploding liners; this approach is similar to that followed ten years ago by Alikhanov et al.⁶ Consideration of liner buckling and Rayleigh-Taylor stability,⁷ particle and energy confinement, and the desire for very compact systems exhibiting high power densities have led to the choice of the fast mode. Fast implosions that are driven by an azimuthal field should alleviate the Rayleigh-Taylor instability and suppress the plastic-elastic (buckling) instability⁸ in addition to allowing wall-confinement of the plasma pressure. The technological problems associated with GJ-level energy transfers and releases over microsecond time intervals are severe,⁹ and to a great extent the magnitude of these problems is related directly to the non-ideal behavior of a fast-liner/plasma system (i.e., liner compressibility, liner stability, field diffusion, plasma turbulence, thermal conduction, and radiation) as reflected by constraints imposed by a realistic engineering energy balance.

The Fast-Liner Reactor (FLR) concept combines the favorable aspects of inertial confinement and heating with the more efficient energy transfer associated with magnetic approaches to yield a conceptual fusion system based on the pulsed burn of a very dense D-T plasma. A thin metal cylinder or "liner" of ~ 0.2 -m initial radius, ~ 3 -mm initial thickness, and ~ 0.2 -m length is imploded radially to a velocity of $\sim 10^4$ m/s by self-magnetic fields resulting from large currents driven axially through the liner. The liner implodes onto a ~ 0.5 -keV, $\sim 10^{24}$ -m⁻³ D-T plasma that is initially formed in or injected into the liner. As the liner implodes in ~ 20 - 40 μ s, adiabatic compression raises the plasma to thermonuclear temperatures, and a vigorous fusion burn ensues for ~ 2 - 3 μ s. During the implosion the plasma pressure is confined inertially by the metal liner and endplug walls. An imbedded azimuthal magnetic field, generated by an axial current driven through the plasma, provides magnetic insulation against radial and axial thermal conduction losses. The energy released by each implosion is sufficient to destroy the liner assembly and a few meters of adjacent electrical leads. Between implosions (~ 10 - 20 s) the previously destroyed liner and leads are replaced by a fresh assembly. The FLR would require a relatively small (~ 2.5 -to 3.0 -m radius) containment vessel and would operate with high engineering power density (~ 5 - 10 MWt/m³). The recirculating

power fraction is anticipated to be in the range 0.15-0.30.

On the basis of detailed physics modeling an FLR operating point is reported, and a conceptual reactor embodiment is described. The major engineering and technology problems associated with the FLR concept, in order of perceived importance are a) the economics of recycling routinely destroyed leads and liners, b) the means of plasma preparation, c) the containment of repeated blasts, d) the switching and transfer of large quantities of fast-pulsed energy (1-2 GJ, 20-30 μ s) to the liner, e) the means by which liners and leads are replaced every 10-20 s. Although the limited scope of this study does not allow a comprehensive or self-consistent analysis of each of these problem areas, an assessment of both physics and technology is presented, and possible solutions to each problem area are proposed.

Section II gives a summary description of the FLR operation and the physics operating point selected on the basis of a cost analysis. Although the physics operating point represents an optimum, insofar as the liner dynamics and achievable technology is concerned, no attempt was made to optimize fully on the basis of cost. Comprehensive descriptions of the physics, engineering/technology, and costing bases are found in Sec. III, which concludes with a detailed description of the reactor point design (Sec. III.D). Since many of the analytic tools required to arrive at the FLR design point had to be "invented" and/or developed specifically for this study, the evolution and implementation of these design tools are discussed in detail in appropriate appendixes. Section IV concludes this report with an assessment of present knowledge associated with both physics and technology issues for the FLR approach.

II. SUMMARY DESCRIPTION OF REACTOR OPERATION

The computational base used to arrive at the FLR design point is described in Secs. III.A-B. Trade-off studies (Sec. III.A.4) have identified two nearly optimum physics design points, which are summarized in Table II-I. First a "low-yield" case relaxes the requirements anticipated for the energy transfer and storage (ETS) system and blast confinement: this low-yield case is marginally acceptable from the viewpoint of recirculating power and economics; the "high-yield" case reverses this emphasis.

On the basis of the physics and energy-balance design point selected for the low-yield case in Table II-I, a number of blast-containment schemes^{9,10,11}

TABLE II-I
INTERIM FLR PHYSICS OPERATING POINTS

<u>Design Parameter, symbol (units)</u>	<u>Low Yield</u>	<u>High Yield</u>
Initial liner inner radius, r_{10} (m)	0.2	0.3
Initial liner thickness, Δ_0 (mm)	3.0	4.5
Initial azimuthal field, B_{10} (T)	13.0	13.0
Initial liner energy, W_L (GJ)	0.336	0.756
Liner Q-value, Q	10.7	14.7
Pure fusion yield, QW_L (GJ)	3.56	11.11
Enhanced fusion yield (MW_{N+W_α}) (GJ)	3.92	12.22
Engineering Q-value, $Q_E^{(a)}$	3.94	5.28
Recirculating power fraction, $\epsilon = 1/Q_E$	0.25	0.19
Cycle time, τ_c (s) ^(b)	10.0	10.0
Total thermal power, P_{TH} (MWt)	430.	1300.
Gross electric power, P_{ET} (MWe)	172.	520.
Recirculating power, P_c (MWe)	43.	99.
Net electric power, P_E (MWe)	129.	421.
Thermal power density, (MWt/m ³) ^(c)	5.8	19.9
Number of units for 1000 MWe (net)	7.8	2.3
Revenue per shot at 40 mills/kWeh (\$)	14.27	46.79
Net plant efficiency, $\eta_p = \eta_{TH}(1-\epsilon)$	0.30	0.32

- (a) All quantities needed to determine Q_E have been specified in the text, except for η_{INT} . On the basis of a preliminary economic optimization of the leads structure (Sec. III.B.4) $\eta_{INT} = 0.9$.
- (b) Chosen on the basis of an estimate of the time needed to replace leads and liner.
- (c) The system power density is based on the total volume enclosed by a 2.6-m-radius containment vessel of wall thickness 0.3 m. The size of the blast radius is based on structural calculations given in Sec. III.B.6.

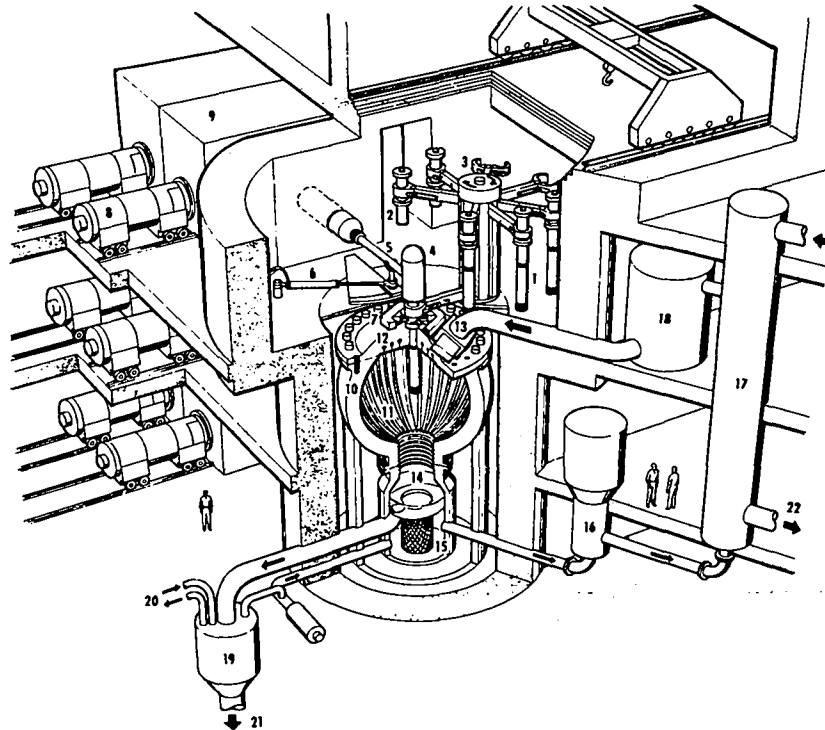


Fig. II-1. Isometric drawing of Fast-Liner Reactor nuclear island for the low-yield case given on Table II.I. Component identification: (1) liner/leads assembly ready for implosion; (2) remains of imploded-liner/leads assembly; (3) liner/leads carousel; (4) plasma preparation; (5) power leads; (6) hydraulic arm to move power connection; (7) blast vessel head and liner/leads feedthrough; (8) homopolar motor/generator; (9) inductive transfer element, transfer capacitor, and switches; (10) blast vessel (2.6-m radius, 013-m wall thickness); (11) shock extending ribs; (12) lithium-spray spargers; (13) lithium inlet and control valve; (14) solid debris skimmer; (15) lithium sump and storage; (16) lithium pump; (17) Li/Na heat exchanger; (18) lithium surge and storage tank; (19) solid debris separation; (20) lithium drag stream to tritium recovery; (21) solids debris to recovery and refabrication; (22) secondary sodium coolant.

were conceived and are described in Sec. III.B.6 and Sec. IV.B.3. A lithium (or lithium-lead) spray was adopted by this study as a coolant/blast-mitigating/breeder medium and used to project the FLR embodiment further. The essential operating components of this approach are shown in Fig. II-1 and are described below. A conceptual 1000-MWe (net) power plant that is based on this concept is described in Sec. III.D.

The liquid-metal spray concept is similar to a scheme proposed by Burke et al.¹² for an electron-beam pellet fusion scheme. Referring to Fig. II-1, fresh liner/leads assemblies [1] coming from a refabrication facility (not shown) are transported to the FLR core as spent liner/leads assemblies [2], and

are removed for reprocessing by the rotating liner manipulator [3]. A liner/leads assembly is inserted through a port in the blast-containment header, and the plasma source and the connector module for the energy transfer and storage (ETS) system [4], which is attached to the external ETS leads arm [5], is moved into place [6]. The liner/leads assembly is clamped to the containment vessel by a latching assembly [7]. The ~450-MJ power supply consists of a bank of homopolar generators [8], an intermediate storage inductor, intermediate transfer capacitors and switches [9], all of which are shown approximately to scale. The nearly spherical FLR pressure vessel [10] with the shaped inner surface, incorporating shock suppression ribs [11] is nominally 0.3-m-thick stainless steel designed to contain repetitive explosive releases of ~1-2 GJ. Blast mitigation, tritium breeding, and heat transfer to the external thermal cycle are provided by a molten Li (or LiPb) spray or "rain" that is injected from the upper inlet manifold [12] through the reactor cavity as the liner implodes. Flow control is provided by the isolation valve [13]. During and after each liner shot a mixture of heated Li coolant and liner/leads debris falls to the debris trap [14] and thermal storage sump [15] below. The mixed-mean temperature rise in the ~50 vol% lithium spray contained within the blast vessel amounts to ~60 K, the temperature difference ultimately appearing across the primary Li/Na heat exchanger [17]. The primary coolant pump [16] continuously draws off the Li coolant for circulation through the primary heat exchanger [17], surge tank [18], and back to the blast cavity. The debris removal system [19] returns insulator and liner/leads material to the refabrication facility [21] for reconstitution into new assemblies. The leads structure is composed of solid Li or LiPb conductor and a glass-like insulator; the conductor material is recovered and extruded into a new leads assembly, but the glass-like electrical insulator is discarded as slag. A tritium recovery system [20] draws off a fraction of the circulating Li coolant. An intermediate coolant loop [22] isolates the nuclear island from the turbogenerator (not shown). For economic reasons an FLR plant may consist of several reactor cavities operating sequentially and sharing a common ETS system and balance of plant. Approximately eight of the 130-MWe(net) units depicted in Fig. II-1 would be required to deliver 1000 MWe(net); this modular approach has been adopted by the costing analysis and is discussed further in Sec. III.D.

III. PHYSICS AND TECHNOLOGY DESIGN BASES

This section quantitatively describes the computational basis for both the burn physics and the engineering design. Because of the unique approach of the inertially confined, magnetically insulated FLR, many of the computational tools had to be developed specifically for this study. Although these models represent the state of the art for this concept, these approximate models are nevertheless preliminary, have yet to be tested against experiment, and remain in a developmental stage.

A. Reactor Physics

Figure III-1 depicts a cylindrical liner configuration as it implodes onto a preinjected plasma in which is embedded an insulating azimuthal magnetic field B_θ , whereas Fig. III-2 depicts a more schematic view. Typical dimensions for an unimploded liner would be 0.2-m radius and 0.2-m length. The field B_θ is created by an axial plasma current I_p as the liner is imploded with a radial velocity v_r by an external azimuthal field caused by an axial drive current I_d (Fig. III-1). A radial, time-dependent computer code LNRBRN has been developed to model both the plasma burn and liner implosion dynamics. Both the physics basis and the numerical procedures embodied in the LNRBRN code are described in this section; a description of the LNRBRN code is found in Appendix A.

1. Plasma Model. The plasma is treated as a single-fluid gas in cylindrical geometry with an embedded magnetic field B_θ ; a radially uniform axial current is assumed to establish this embedded field. The LNRBRN model computes radial thermal conduction and field diffusion in the MHS approximation* while incorporating an analytic approximation for axial thermal conduction as a function of radius. Bremsstrahlung and D-T burnup are computed at the plasma midplane as functions of radius. Alpha-particle heating of the plasma is not considered, since the alpha-particle mean-free-path for thermalization is several times the plasma radius at peak compression. The plasma and field pressures are computed at the plasma-boundary and are dynamically coupled to the plasma-liner motion.

*The magnetohydrostatic (MHS) model treats all but the inertial terms in the MHD approximation.

LINER ASSEMBLY WITH ANNULAR PLASMA INJECTION

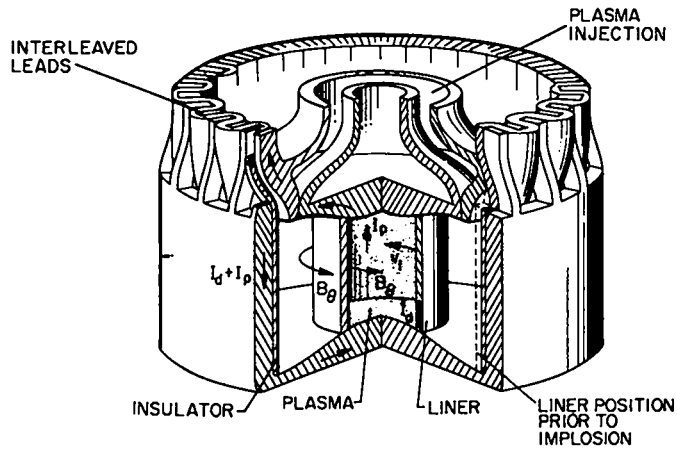


Fig. III-1. Schematic diagram of 0.2-m initial radius and 0.2-m-long liner assembly showing (a) plasma current I_p that generates internal azimuthal field B_θ for thermal insulation between plasma (inside inner vessel) and liner wall, (b) liner drive current I_d that causes the external azimuthal field B_θ to drive the liner inward with a velocity v_d . A "force-reduced" interleaved leads structure and a port for coaxial plasma injection are shown.

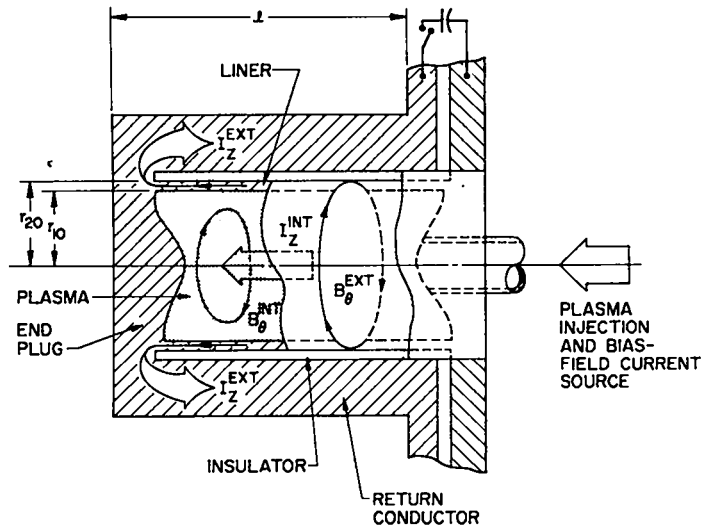


Fig. III-2. Schematic diagram of 0.2-m initial radius and 0.2-m-long liner assembly showing in more detail the liner per se, the internal axial current I_z^{INT} creating the insulating field B_θ , and the drive current I_z^{EXT} creating the drive field B_θ^{EXT} . Massive return conductors, the electrical insulation, and feedplate leads structure are shown.

a. Radial Transport. LNRBRN is an implicit Lagrangian code. Sound transit times in a typical liner plasma are much less than the implosion time; inertial terms, therefore, can be neglected and plasma motion is determined by pressure balance ($\vec{j} \times \vec{B} = \vec{\nabla} P$) for equal electron and ion temperatures. This MHS pressure balance can be transformed to the following integral equation when the magnetic field exhibits only the azimuthal or "O" direction

$$2nk_B T + B_\theta^2/2\mu_0 = (4/r^2) \int_0^r n k_B T r' dr' \quad , \quad (\text{III-1})$$

where k_B is the Boltzmann constant ($1.6(10)^{-16}$ J/keV), $n(1/m^3)$ is the ion density $\mu_0 = 4\pi(10)^{-7}$ H/m, and T is expressed in keV units.

Plasma parameters are computed as functions of time by a two-step method.¹³ First, the Lagrangian mesh is fixed in space, and all diffusion and loss processes are evaluated for a given time step. The basic equations are

$$2nk_B(\partial T/\partial t) = (1/r) \partial[rk\partial T/\partial r]/\partial r + S \quad , \quad (\text{III-2})$$

$$\mu_0(\partial B_\theta/\partial t) = \partial[\eta(B_\theta/r + \partial B_\theta/\partial r)]/\partial r \quad , \quad \text{and} \quad (\text{III-3})$$

$$\partial n/\partial t = -n^2\langle\sigma v\rangle/2 \quad , \quad (\text{III-4})$$

where k is the thermal conductivity,¹⁴ η is the electrical resistivity,¹⁴ S is a net volumetric power source (or sink), and $\langle\sigma v\rangle$ is the Maxwellian-averaged D-T fusion reactivity. Since the alpha particles are assumed to escape unthermalized from the plasma, charge neutrality requires that two electrons also escape the plasma for each fusion reaction.

The bremsstrahlung power density, as used in the source term S , is taken as¹⁵

$$S_{BR}(W/m^3) = -5.35(10)^{-37} n^2 T^{1/2} \tanh(T/T_W - 1) \quad , \quad (\text{III-5})$$

where T_W is an assumed wall temperature. The hyperbolic tangent has been incorporated into the usual bremsstrahlung expression in order to approximate radiation reabsorption by the dense plasma immediately adjacent to the wall. The plasma performance, as predicted by LNRBRN, is generally insensitive to

the assumed value for T_W . After Eqs. (III-2)-(III-4) are solved for a given time step, the Lagrangian mesh is adjusted in space to reestablish pressure balance (Eq. (III-1)) and these equations are then coupled dynamically to the liner behavior (Sec. III.A.3 and Appendix A). This procedure completes the above-mentioned two-step approach.

b. Axial Transport. An analytic model for axial thermal conduction was derived¹⁶ to give an axial conduction heat-sink term, S_{CZ} , for use in Eq. (III-2). The results from Eqs. (III-2)-(III-4) are representative of the midplane in a liner plasma of length ℓ . Plasma parameters are expected to be nearly constant in the axial direction except near and within the high-density, low-temperature sheath near the endplug (Fig. III-1).

The axial conduction model assumes (a) axial and radial thermal conduction are separable, (b) fields and plasma pressures are independent of axial position, (c) thermal conductivity¹⁴ can be divided into three regions according to the magnitude of $\omega\tau$ for ions and electrons, where ω is the gyrofrequency and τ is the respective collision time.

Region I ($\omega_i\tau_i > 1$)

$$k_i = 8.0(10)^{-39} n^2 \ell n \Lambda / T^{1/2} \quad ; \quad (\text{III-6})$$

Region II ($\omega_e\tau_e > 1, \omega_i\tau_i < 1$)

$$k_i = 2.5(10)^{13} T^{5/2} / \ell n \Lambda \quad ; \quad (\text{III-7})$$

Region III ($\omega_e\tau_e < 1$)

$$k_e = 1.5(10)^{15} T^{5/2} / \ell n \Lambda \quad ; \quad (\text{III-8})$$

where except for $T(\text{keV})$, mks units are consistently used. For $Z = 1$ and an average D-T atom ($A = 2.5$), $\omega_i\tau_i = 4.0(10)^{25} B_\theta T^{3/2} / n \ell n \Lambda$, $\omega_e\tau_e = 1.9(10)^{27} B_\theta T^{3/2} / n \ell n \Lambda$, and $\Lambda = 9.32(10)^{16} T / n^{1/2}$.

Assumption (d) stipulates that Region III is a small and probably turbulent space near the endplug that can be neglected. The transition between Regions I and II is defined by $\omega_i\tau_i = 1$ for each radius; a corresponding transition temperature and axial position, T_t and z_t , can be

defined. On the basis of the constant-pressure assumption the cross-field ion thermal conductivities are given by

$$k_i = C_I T^{-5/2} \quad (\text{Region I}) \quad (\text{III-9})$$

$$k_i = C_{II} T^{5/2} \quad (\text{Region II}) \quad , \quad (\text{III-10})$$

where $C_I = 8.0(10)^{-39} (nT)^2 \ln \Lambda_t / B_\theta^2$ and $C_{II} = 2.5(10)^{13} / \ln \Lambda_t$. Considering only axial thermal conduction and the constant pressure assumption, the axial heat conduction equation can be integrated from the liner midplane ($z = 0$, $\partial T / \partial z = 0$) to any value of z , this result is then integrated over the liner length to give an effective axial conduction power loss per unit volume at a given radius.

$$S_{CZ} (\text{W/m}^3) = - (16/\ell^2) \left[C_I (T^{-3/2} - T_c^{-3/2}) / 3 - C_{II} T_c^{7/2} / 7 \right] \quad . \quad (\text{III-11})$$

The source term S in Eq. (III-2) is equal to the sum of S_{BR} (Eq. (III-5)), S_{CZ} (Eq. (III-11)), and joule heating terms (alpha-particle heating is insignificant).

c. Burn Dynamics. The thermonuclear reaction rate $n^2 \langle \sigma v \rangle / 4$ for a 50/50 DT fuel mixture is computed as a function radial position at the $z = 0$ midplane using tabular values for the D-T, Maxwellian-averaged reactivity, $\langle \sigma v \rangle$. Since the alpha-particle mean free path classically is expected to exceed the (compressed) plasma dimensions, alpha particles are assumed lost and, hence, do not contribute to the plasma energy or pressure. If a significant portion of the alpha-particle energy were to be retained by the plasma, compression would be inhibited, and the fusion yield would be diminished for the optimized physics operating point reported here. Furthermore, the influence on the liner of the thermal flux associated with unthermalized alpha particles is not treated by the LNRBRN model.

2. Liner Model. The pressures and accelerations to which the liner will be subjected are significant, and both compressibility and hydrodynamic stability must be taken into account. Although detailed MHD codes, such as CHAMISA,¹⁷ are available with appropriate equation-of-state data and field-diffusion models, such code systems are too cumbersome for use in the present parametric systems analysis. Consequently, LNRBRN uses a simplified

analytic model of the liner,¹⁷ and has shown good agreement with the predictions of the detailed CHAMISA code system.

a. Stability. Four potentially disruptive effects on liner motion have been considered:⁵ the Rayleigh-Taylor instability, liner buckling, the sausage instability, and manufacturing asymmetry. The Rayleigh-Taylor instability arises when the boundary of two fluids of unequal density or a single fluid with a density gradient is accelerated in the direction of the density gradient. Treating the liner as a fluid, the condition for onset of this instability occurs at the outer surface as the liner is accelerated by the driving magnetic field. A similar instability may develop inside the liner as it is decelerated by the compressed plasma.⁷ The liner physically yields and may be regarded as plastic or liquid shortly after compression by the driving field begins; detailed analysis,⁵ however, indicates the growth rate (relative to the implosion time) of Rayleigh-Taylor modes will be substantially reduced by a high viscosity of the liner metal. Experimental evidence¹⁸ indicates that for aluminum or copper the high pressure of the liner environment increases the viscosity sufficiently to eliminate the need for liner rotation, as is required for the "slow" liner approach.⁷

The buckling instability can occur when an inward force is applied to a stiff convex shell, such as occurs when the drive field acts on the liner. According to preliminary studies^{5,8} the azimuthal or "Z-pinch" drive field is sufficiently stabilizing in the azimuthal or " θ " direction to reduce significantly the potential for liner buckling. Conversely, the Z-pinch field is destabilizing with respect to sausage modes in the axial direction. The latter instability is similar to the Rayleigh-Taylor modes and may be regarded as an additional term in that analysis. Determination of the significance of sausage modes is an objective of the LASL Fast Liner Experiment.^{5,19}

Finally, potentially adverse disturbance of liner motion may arise from manufacturing asymmetry. If, for example, the liner has an uneven thickness, the thinner parts will implode faster, causing an irregular liner shape at peak compression. This effect is more severe for high compression ratios. Experimental studies will undoubtedly lead to increased understanding of the required manufacturing tolerances.¹⁹ It is noted that the fast-imploding-liner experiments performed both in the USA²⁰⁻²² and in the USSR² have encountered no significant liner stability problems.

b. Dynamics. An analytic liner model has been developed on the basis of the impulse-momentum approximation¹⁷ and is used in LNRBRN. In this model, the equation of state for the liner is approximated by

$$P/B_0 = \left[(\rho/\rho_0)^{B'} - 1 \right] / B' \quad , \quad (\text{III-12})$$

where P is pressure, ρ and ρ_0 are densities with and without pressure, respectively, B_0 is the bulk modulus at low pressure, and B' is a dimensionless parameter which is used to fit Eq. (III-12) to empirical data for a wide range of pressures.¹⁷

The inner and outer radii of the liner are defined as r_1 and r_2 , respectively, and the combined plasma and field pressure at the inside surface of the liner is defined as $P_1 \equiv P(r_1)$. The impulse-momentum model gives the pressure within the liner walls as a function of radius

$$P(r) \approx P_1 \left[\frac{r_2 - r}{r_2 - r_1} \right]^{B'/(B'-1)} \quad . \quad (\text{III-13})$$

Likewise, the radial dependence of liner density is given by

$$\rho/\rho_0 \approx \left[1 + (B'P_1/P_0) \left(\frac{r_2 - r}{r_2 - r_1} \right)^{1/B'} \right]^{B'/(B'-1)} \quad . \quad (\text{III-14})$$

The motion for the liner is described by²³

$$d^2(\bar{R})/dt^2 = (2\pi/\rho_0 A_0) \left[P_1 r_1 + \int_{r_1}^{r_2} P dr \right] \quad , \quad (\text{III-15})$$

where A_0 equals $\pi(r_2^2 - r_1^2)$, and \bar{R} is a mass-averaged radius given by

$$\bar{R} = (2\pi/A_0) \int_{r_1}^{r_2} (\rho/\rho_0) r^2 dr \quad . \quad (\text{III-16})$$

Equations (III-15) and (III-16) are coupled to the plasma motion and solved numerically, as described in Sec. III.A.3.

The essential approximations regarding liner dynamics are encompassed in

Eqs. (III-12) and (III-13). The analytic form of the equation of state eliminates the need for a stepwise analysis of the liner over its radial thickness. The impulse-momentum approximation leading to Eqs. (III-13) and (III-14) assumes that relative velocities within the liner are considerably less than the initial liner velocity and that the sound transit time in the liner is short compared to characteristic implosion time. Comparisons between this approximate and analytic method with the CHAMISA code have given excellent agreement.¹⁷

3. Numerical Methods. As noted in Sec. III.A.1.a., LNRBRN is based on a two-step numerical method¹³ in which the transport equations are solved on a fixed Lagrangian spatial mesh; the mesh is subsequently readjusted adiabatically at each time step to satisfy pressure balance (Eq. (III-1)). The plasma is treated as an ideal single-particle gas, and azimuthal flux conservation is imposed. An iterative scheme matches the plasma radius and pressure to the liner radius r_1 computed with the liner dynamics model, Eqs. (III-15) and (III-16). A description of the LNRBRN numerical procedure and logic flow is described in Appendix A. A complete time-dependent description of all liner, plasma, and thermonuclear yield parameters is given by LNRBRN. Generally, the most important final result for a given input (i.e., initial plasma density and temperature, initial plasma beta, liner geometry, and input energy) is the ratio of initial liner energy W_L to the sum of fusion neutron yield W_N and alpha-particle yield W_α . This "liner" or scientific Q-value, $Q = (W_N + W_\alpha)/W_L$, is the object function used in all physics optimizations described in the following section; the liner Q-value represents the essential interface between the liner physics and the FLR engineering design. Section III.B.1 describes the major system efficiencies that relate Q to the engineering Q-value, Q_E (recirculating power fraction $\epsilon = 1/Q_E$).

4. Development of Physics Operating Point. To obtain liner Q-values greater than 10, as required for an economical reactor (Sec. III.B.1), an analytic plasma-liner model was used to estimate a starting point for the optimization of Q; this lossless model indicates liner energies on the order of $W_L = 1-2$ GJ/m and initial plasma line densities of $1-2(10)^{23}$ m⁻¹. Initial liner parameters, that are compatible with these criteria in a copper liner, are inner radius $r_{10} = 0.2$ m, thickness $\Delta_0 = 3$ mm, velocity $v_{10} = 10^4$ m/s, and plasma density $n_0 = 10^{24}$ m⁻³. Other initial conditions

include a plasma temperature T_0 and an initial insulating magnetic field at the plasma/liner interface B_{10} . The analytic model of a lossless plasma¹⁷ predicts $T_0 \approx 0.5$ keV for initial liner conditions specified above. The initial azimuthal magnetic field is assumed to arise from a uniform axial current I_p in the plasma (Fig. III-1).

Since pressure balance (Eq. (III-1)) is always satisfied, the temperature and density cannot be uniform. Hence, T_0 and n_0 are initially specified on the axis; the bulk of the plasma is fixed at T_0 , but near the wall the temperature drops smoothly to T_w . With temperature, field, and density specified, Eq. (III-1) is solved for $n(r, t = 0)$. Equations (III-2)-(III-4) are solved, with the initial profiles so determined, and always maintaining local pressure balance (Eq. III-1). The pressure exerted by the plasma and field on the imploding wall is used as one component in the solution of the liner equations of motion. Figure III-3 gives an example of the time dependence of the inner radius r_1 , fusion power P_f , and total liner losses W ; ohmic heating of the liner is not included in W . The liner dynamics include an analytic approximation to the liner compressibility, this compressibility model being verified by detailed hydrodynamic computations (CHAMISA).¹⁷

Having consistently specified the initial liner dimensions and velocity, a three-parameter search in initial density, temperature, and insulating field was made to determine the optimum liner Q-value. Rather than specifying B_{10} , it is more convenient to vary the initial, global beta β_{10} at the liner wall, where $\beta_{10} = (B_{10}^2/2\mu_0)/(2n_0k_B T_w + B_{10}^2/2\mu_0)$. Figures III-4 and III-5 show the dependence of Q on T_0 and n_0 for two initial liner energies; the initial liner and plasma parameters were adjusted by analytic scaling relationships to preserve Q near optimum. Shown also on Figs. III-4 and III-5 is the relationship between β_{10} and B_{10} , as determined by pressure balance (Eq. (III-1)). For each β_{10} a maximum Q in (T_0, n_0) space is found.

The maxima shown in Figs. III-4 and III-5 result from a complex interaction between the liner and plasma. The liner Q-value decreases with decreasing T_0 because adiabatic compression to thermonuclear temperatures becomes less efficient, resulting in a higher compression and shorter "dwell" or burn time. Furthermore, once the overcompressed state is reached, the higher plasma density at this point results in an increased radiation loss. On the other hand, for high values of T_0 the peak temperature is reached at

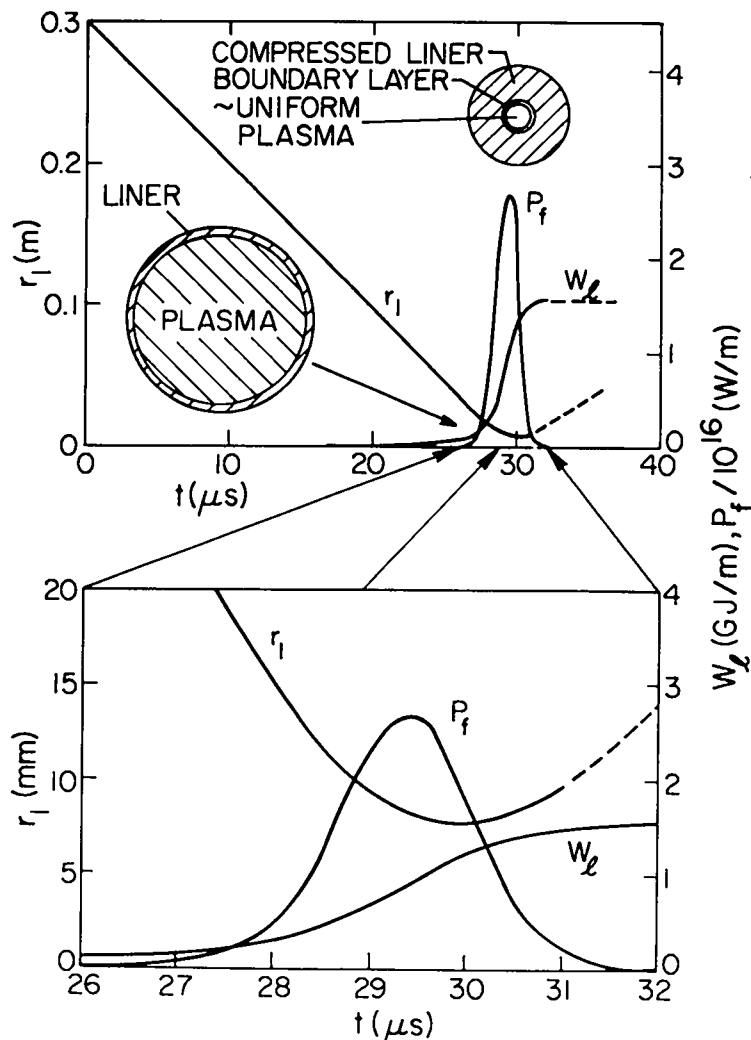


Fig. III-3. Typical response of liner and plasma as predicted by the MHS burn code LNRBRN. Shown is the time dependence of the inner liner radius r_1 , the fusion power per unit length p_f , and the total energy lost during the compression W_l .

lower compressions and densities, and the corresponding peak reaction rate ($n^2 \langle \sigma v \rangle$) decreases faster than the dwell time increases. Since more insulating magnetic field exists at the wall for low values of β_{10} , the increase in Q with decreased β_{10} reflects better magnetic insulation.

Similar processes give rise to a maximum Q at fixed T_0 as the initial density n_0 is varied. At low values of n_0 , the compression is high, the dwell time is short, and the decrease in line density results in lower thermonuclear yields. For larger values of n_0 the final compressed temperature decreases and again the thermonuclear yield decreases. Throughout this process the complications of axial and radial thermal conduction, radiation

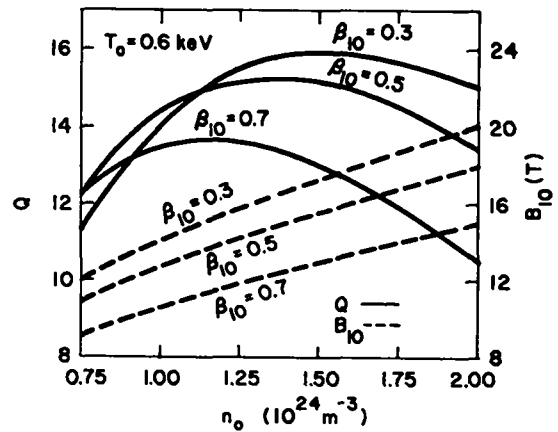
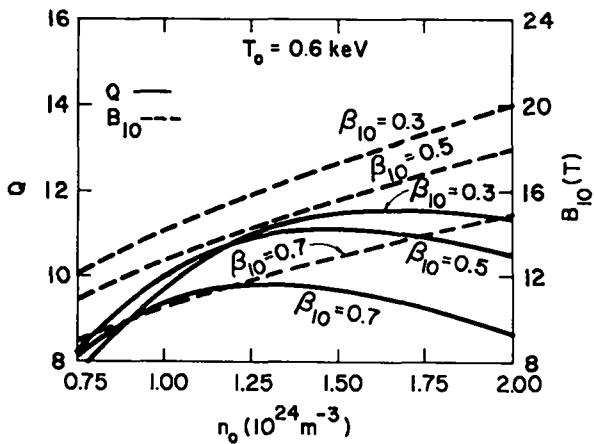
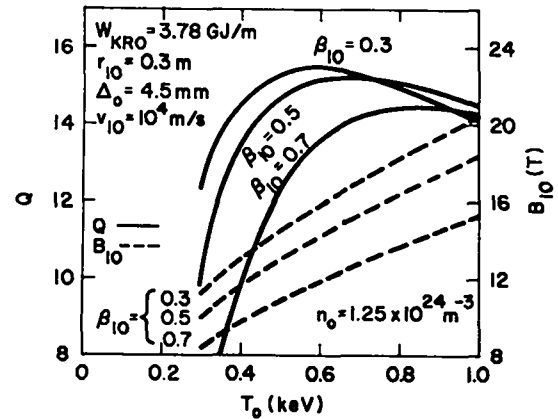
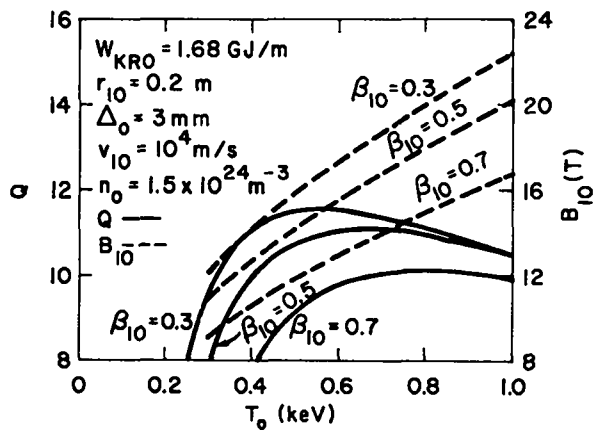


Fig. III-4. Dependence of the liner Q-value Q , and the insulating field at the wall B_{10} , on initial plasma temperature T_0 and density n_0 . These curves have been computed for the low-yield case with W_{KRO} , r_{10} , and v as shown and global beta values at the wall of $\beta_{10} = 0.3, 0.5$, and 0.7 .

Fig. III-5. Dependence of the liner Q-value Q , and the insulating field at the wall, B_{10} , on initial plasma temperature T_0 and density n_0 . These curves have been computed for the high-yield case with W_{KRO} , r_{10} , and v as shown and global beta values at the wall of $\beta_{10} = 0.3, 0.5$, and 0.7 .

loss, and liner compression play varyingly important roles. For example, Fig. III-4 shows Q plotted along two orthogonal lines in (T_0, n_0) space ($n_0 = 1.5(10)^{24} \text{ m}^{-3}$, $T_0 = 0.6 \text{ keV}$). For $\beta_{10} = 0.5$ the intersection of these lines closely approaches the peak of a three-dimensional "hill" at $Q_{\text{max}} = 11.1$. Simple extrapolation indicates that for $\beta_{10} = 0.3$, $Q_{\text{max}} = 11.6$ at $T_0 = 0.5 \text{ keV}$ and $n_0 = 1.6(10)^{24}$, and for $\beta_{10} = 0.7$, $Q_{\text{max}} = 9.9$ at $T_0 = 0.8 \text{ keV}$ and $n_0 = 1.3(10)^{24} \text{ m}^{-3}$.

The optima determined up to this point are based on a fixed liner velocity, although two liner energies were considered. Before a trajectory in velocity space can be constructed, values of β_{10} , n_0 , and T_0 must be selected that are technologically achievable insofar as a final reactor operating point is concerned. A low value of β_{10} would be desirable, since the associated high fields at the wall provide good thermal insulation. Based on a qualitative judgment as to the maximum initial field (and current) that can be achieved, $\beta_{10} = 0.5$ was chosen. The associated values of n_0 and T_0 for both energy cases depicted on Figs. III-4 and III-5 were selected slightly to the left of the point of optimum Q in order to reduce the plasma injection requirements while still preserving a near optimum Q . For both liner energy cases the chosen values of n_0 and T_0 are depicted on the plots of Q versus initial liner velocity v_{10} , given in Fig. III-6; the effects of liner compression and plasma losses (radiation and conduction) are also shown.

For the case of an incompressible liner and a lossless plasma shown in Fig. III-6, Q drops with increasing initial liner velocity v_{10} at constant liner energy (thinner liners) because of a decreased burn time. When the liner compressibility is included, but the plasma remains lossless, very low velocities require thick liners (constant initial energy), and an appreciable fraction of the initial liner energy is involved in compressing the liner material. As expected, the incompressible case is retrieved for thin fast liners. The inevitable optimum in Q for compressible liners is higher than the Q -value for the incompressible liner because of the longer burn times that can result from liner compression; this increased burn time increases the thermonuclear yield to an extent that overcomes the associated liner compression losses. For the case of a compressible liner with conduction and radiation losses, the plasma losses can become significant when the implosion and burn times are long, thereby reducing substantially the plasma energy at

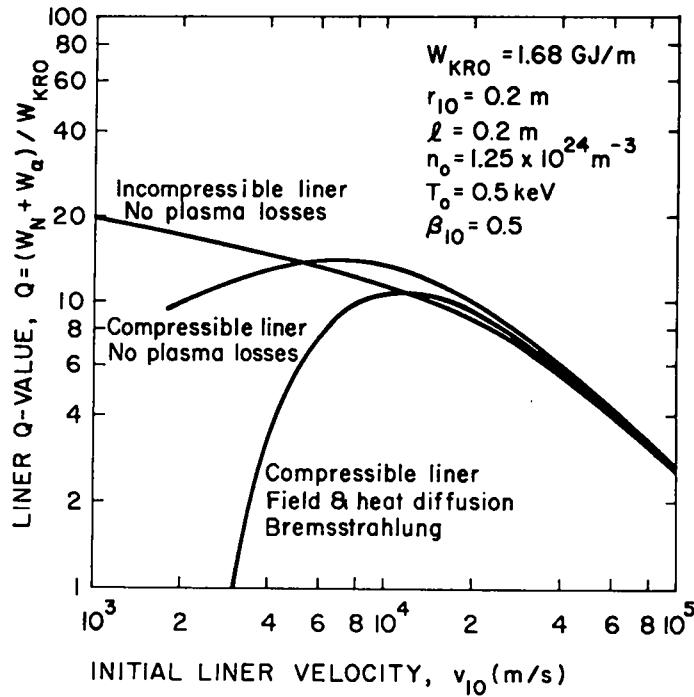


Fig. III-6A. Dependence of liner Q-value, Q , on the initial liner velocity v_{10} for the near optimum cases shown on Fig. III-4. The effects of plasma losses and liner compressibility are illustrated.

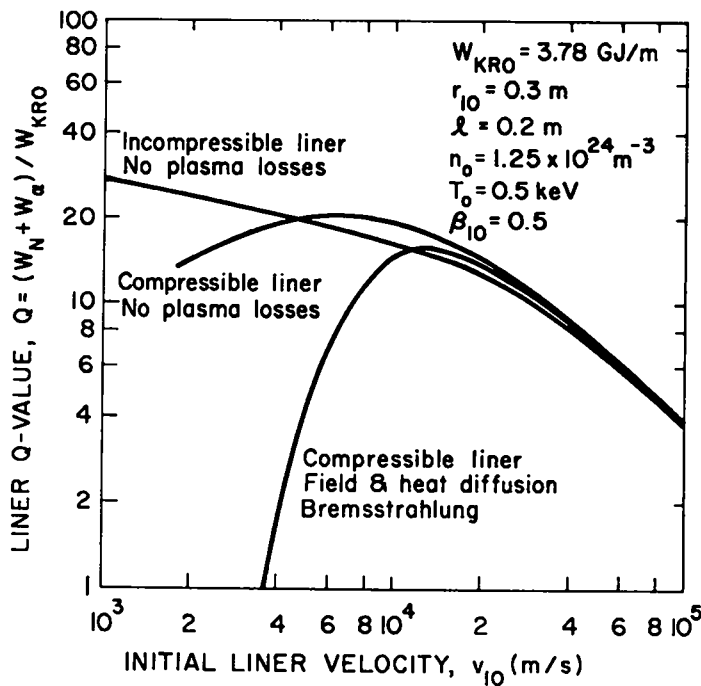


Fig. III-6B. Dependence of liner Q-value, Q , on the initial liner velocity v_{10} for the near optimum cases shown on Fig. III-4. The effects of plasma losses and liner compressibility are illustrated.

peak compression. This behavior has been depicted in Fig. III-3, which shows that most losses occur during the short burn time. As the liner velocity is increased, Q increases and exceeds the Q -value predicted for the lossless-plasma, incompressible-liner case because of the previously described damped liner motion. At high liner velocities, the dependence of Q on v_{10} becomes identical to the incompressible-liner, lossless-plasma case. The optimum velocities are very close to the v_{10} values assumed in arriving at the near optimum values of n_0 and T_0 in Figs. III-4 and III-5. The optimum Q can be shifted to different values of v_{10} by changing initial conditions T_0 and n_0 .²⁴

Based on these trade-off studies, two near-optimum FLR design points have been identified in order to pursue scoping calculations of the relevant reactor technology and economics. These interim design points are, first, the "low-yield" case, which relaxes the ETS and blast-confinement constraints but may not be attractive from the viewpoint of economics; the "high-yield" case reverses this emphasis. The essential features of these operating points are summarized in Table II-I. For both cases $v_{10} = 10^4$ m/s, $\beta_{10} = 0.5$, $T_0 = 0.5$ keV, $n_0 = 1.25(10)^{24}$ m⁻³, and $\ell = 0.2$ m. Other parameters, such as the neutron energy multiplication $M = 1.1$, the thermal conversion efficiency $\eta_{TH} = 0.4$, the external ETS efficiency η_T^{EXT} , the internal (leads) ETS efficiency η_T^{INT} , the fraction of the ETS energy W_{ETS} needed for plasma preparation $f_{p0} = 0.04$, and the similar fraction $f_{AUX} = 0.06$ associated with auxiliary power requirements, depend on the overall FLR system energy balance. This aspect of the FLR study is addressed in the following section.

B. Reactor Engineering/Technology

Aside from the energy transfer and storage (ETS) requirements, the FLR power system portends the overall simplicity of "a pot, a pipe, and a pump." Similar to the FLR physics, however, the engineering technology in most respects is not conventional and represents an extrapolation, despite an inherent simplicity and compactness. Key technological and economic issues envisaged for the FLR are summarized below in the context of the overall FLR power system. The more crucial technological issues have been quantified where possible, although the level of effort devoted to FLR engineering has not permitted a detailed, self-consistent design. After describing the

engineering energy balance upon which the point design summarized in Table II-I is based, the following technologies are addressed in order of perceived importance and/or difficulty: plasma preparation, ETS, liner leads, neutronics, containment, and heat transfer.

1. Energy Balance. The FLR energy balance is described schematically on Fig. III-7. The total energy transferred from the ETS system is $W_{ETS} = W_L / \eta_T^{INT} \eta_T^{EX}$, where η_T^{EX} is the efficiency of energy transfer from the ETS system to the containment vessel. The electrical energy entering the containment vessel is W_L / η_T^{INT} ; of this energy $W_L(1/\eta_T^{INT} - 1)$ is dissipated ohmically in the connecting leads within the containment vessel, and W_L reaches the liner itself. The fusion yield is composed of the neutron energy W_N and the alpha-particle energy W_α . Neutron energy multiplication in the sprayed "blanket" (coolant, blast mitigation, tritium breeder) increases the effective neutron energy to MW_N .

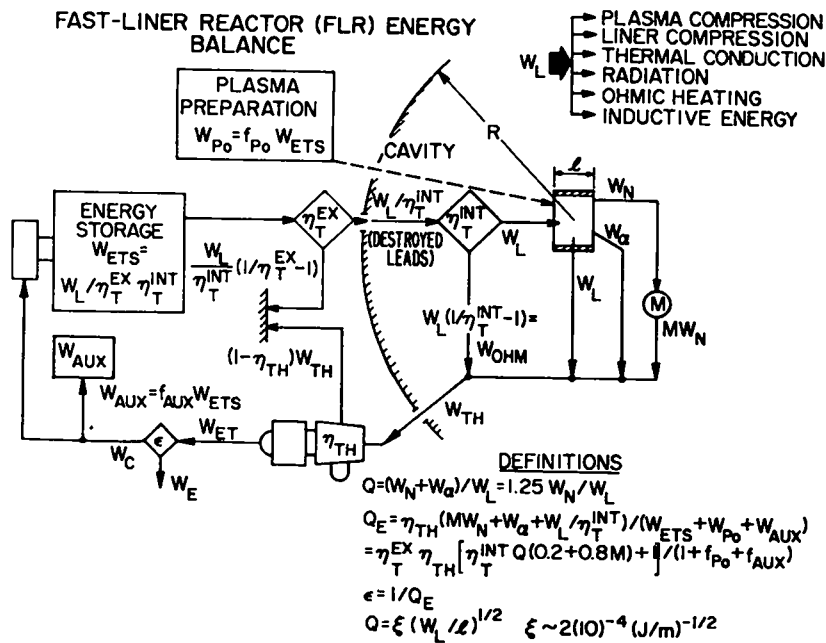


Fig. III-7. Schematic diagram of Fast-Liner Reactor energy balance, showing the partition of the energy that is delivered to the liner among the various liner energy loss mechanisms. Shown also is the relationship between the plasma or liner Q-value Q , and the engineering Q-value Q_E . The external transfer efficiency η_T^{EX} is assumed to be 0.95 and the internal transfer efficiency η_T^{INT} is computed on the basis of a cost optimization. The relationship between Q and W_L depicted has been numerically and analytically.¹⁷

After each shot the high-grade thermal energy removed from the containment vessel is $W_{TH} = W_L/\eta_T^{INT} + MW_N + W_\alpha$. This energy is converted to electricity with a thermal conversion efficiency η_{TH} .

The liner or "scientific" Q-value is defined as $Q = (W_N + W_\alpha)/W_L = 1.25 W_N/W_L$. The liner Q-value depends primarily on physics considerations of liner performance, as discussed in Sec. III.A.4, and has accordingly been "optimized." In contrast, the engineering Q-value, Q_E , measures the total electrical energy produced as compared to the energy required to operate the plant. That is

$$Q_E = \eta_{TH}(MW_N + W_\alpha + W_L/\eta_T^{INT})/(W_{ETS} + W_{PO} + W_{AUX}) \quad , \quad (III-17)$$

where the plasma preparation energy is W_{PO} , and W_{AUX} is the auxiliary plant requirement. Defining $f_{PO} = W_{PO}/W_{ETS}$, $f_{AUX} = W_{AUX}/W_{ETS}$, and $W_L/W_{ETS} = \eta_T^{EX INT}$ leads to the following relationship between Q_E and Q

$$Q_E = \eta_T^{EX} \eta_{TH} \left[\eta_T^{INT} (0.2 + 0.8 M) Q + 1 \right] / \left[1 + f_{PO} + f_{AUX} \right]. \quad (III-18)$$

For the conditions depicted on Table II-I, $f_{PO} = 0.04$, and f_{AUX} is taken to be 0.06. The description for a 40-50 vol% lithium spray in Sec. III.B.5 indicates that $M = 1.1$, and for all computations η_{TH} is taken to be 0.4. The high-yield case (Table II-I) gives a physics-optimized Q of 14.7, whereas the low-yield baseline case selected for the technology assessment gives $Q = 10.7$. The internal and external ETS transfer efficiencies, η_T^{EX} and η_T^{INT} , remain to be specified. It is noted the reversible recovery of the ETS energy is not required by the FLR concept.

The ETS system must supply $W_{ETS} \approx 400$ MJ in 20-30 μ s with high efficiency η_T^{EX} to the containment vessel. This external circuitry would be cycled millions of times each year, and considerable flexibility and expense would be evoked to assure that $\eta_T^{EX} \gtrsim 0.95$ could be achieved; the parasitic energy $W_{ETS}(1-\eta_T^{EX})$ generally represents both a loss in revenue as well as

added capital expenditures needed for the incremental ETS system. In contrast, a major portion of the leads structure located within the containment vessel would be destroyed each shot; the configuration of these internal leads determines the ultimate value of η_T^{INT} . Hence, the design values of η_T^{INT} must be determined by an optimization procedure that balances the cost of destroyed leads structure, leads energy loss (recovered by the thermal cycle), and the effects on plant revenue/cost as reflected by the dependence of Q_E on η_T^{INT} (Eq. (III-18)). This latter issue is addressed in Sec. III-B.4; generally $\eta_T^{INT} \approx 0.9$ is required. On this basis, Table II-I indicates $Q_E = 3.94$ for the low-yield case, which corresponds to a recirculating power fraction $\epsilon = 1/Q_E = 0.25$.

2. Plasma Preparation. According to Table II-I for the low-yield case, the optimized initial plasma requirements are $T_0 = 0.5$ keV, $n_0 = 1.25(10)^{24} \text{ m}^{-3}$, and an initial azimuthal magnetic field at the wall $B_0 \approx 13 \text{ T}$ ($\beta_{10} \approx 0.5$); these parameters correspond approximately to 3.4 MJ of plasma energy delivered to the $\sim 0.025\text{-m}^3$ initial liner volume ($r_{10} = 0.2 \text{ m}$, $l = 0.2 \text{ m}$) on a $\sim 1\text{-}\mu\text{s}$ time scale. The field energy corresponds to $\sim 1 \text{ MJ}$, which for a uniform current density amounts to 100 MA/m^2 or 13 MA . Four potential plasma-preparation schemes are under consideration: coaxial gun injection,²⁵ shock-tube injection,²⁶ exploding D-T threads,²⁷ and in situ plasma formation by laser²⁸ or relativistic-electron²⁹ beams. As an example of the first case, a coaxial gun would be located outside the blast zone to inject the plasma along a magnetic guide field to the liner. The guide tube and field would be located inside the liner/lead structure. Plasmas have been produced with densities of $2(10)^{23} \text{ m}^{-3}$ and directed energies of $\sim 0.2 \text{ keV}$, and these plasmas are believed to contain embedded poloidal fields.²⁵ Substantial development is required, however, to create plasmas at the temperature, density, and field required by the FLR. The problem of transporting such a plasma is also unsolved.

The electromagnetic shock-tube and exploding-wire techniques would produce the plasma inside the liner, thereby eliminating the need for transport from an external source. The plasma source in this case must be simple and inexpensive, since it must be replaced by each shot. For the case of the electromagnetic shock tube, a high current passing through a conductor along the liner axis produces a strong poloidal field near the conductor. The short

field risetime ($\sim 1 \mu\text{s}$) causes an electromagnetic shock to propagate radially from the conductor, heating the surrounding DT gas to the required plasma temperature. Plasmas with 0.5-keV temperatures and $\sim 10^{22}\text{-m}^{-3}$ densities have been produced by this method; much more work, however, is needed to reach the projected reactor parameters.

An example of the exploding-wire technique would have a solid (cryogenic) DT filament placed along the liner axis. A strong axial current would cause the thread to explode and to form the required plasma in situ. Deuterium threads with the appropriate dimension (300- μm diameter) have been produced,²⁷ but whether the necessary plasma condition can be reached must still be demonstrated. Like the shock-tube and DT filament approaches, laser or electron beams could produce the required temperatures and densities in situ. The use of beams, however, could eliminate the need for delicate or expensive apparatus that must be located in the vicinity of the liner. CO_2 laser beams have routinely produced the required $\sim 0.5\text{-keV}$ temperatures at $\sim 10^{24}\text{ m}^{-3}$ density,²⁸ but these plasmas have not been produced in the required volumes (0.025 m^2). Although the question of beam transport remains for the relativistic-electron-beam approach, the generation of the required insulating magnetic fields may be more straightforward than for laser beams.

In summary, both the theoretical and experimental state of the art for FLR plasma preparation is embryonic but developing. Although more computation can be made on the various techniques suggested above, detailed design of this aspect of the FLR is expected to remain vague until related experiments are performed. The primary contribution that this systems study can make at this point in the development of fast-liner fusion is to quantify from the reactor viewpoint the optimal initial conditions (n_0 , T_0 , β_{10}) and to indicate the consequences of not achieving these optimal conditions in the laboratory (i.e., Fig. III-5). Plasma preparation is viewed as one of the more crucial physics and technological issues for the FLR concept, and consequently, is being subjected to early experimental study.¹⁹

3. Energy Storage, Switching, and Transfer. The liner drive in a typical, low-yield FLR (Table II-I) will require $\sim 250\text{ MA}$ at $\sim 200\text{ kV}$ in 200-300 μs for an energy transfer of 450 MJ. This energy transfer W_{ETS} is $\sim 10\%$ greater than deduced from Table II-I in order to account for resistive losses in the liner, which are not included in the LNRBRN model (Appendix A).

Both inductive and capacitive energy storage were considered in a preliminary study of a much lower yield FLR⁵ ($W_L \approx 70$ MJ); Figure III-8 schematically depicts these two ETS options. In the inductive ETS system a homopolar generator would transfer energy to a normal conducting inductor in a few milliseconds; current would then be switched to the liner, transferring energy on a 20- μ s time scale. For a capacitive ETS a large capacitor bank would be discharged directly to the liner.

Although inductive energy storage is considerably less expensive³⁰ than comparable capacitors, inductive ETS nevertheless requires a substantial transfer capacitor to eliminate resistive energy losses incurred during the transfer and to couple efficiently the source (ETS) and load (liner). In preliminary FLR studies⁵ 45% of W_L was held in the transfer capacitor at the end of the transfer cycle. An inductive system, therefore, would show little advantage compared to a capacitive ETS unless the required transfer capacitor could be made substantially smaller than the total energy storage.

Another advantage of capacitive energy storage arises because switches must only close a circuit during a given cycle rather than requiring high-current opening or interrupting switches. Although the switching problem has not been thoroughly studied for the FLR application, the magnitude of both power and energy transfer is far beyond the capability of the present commercial sector. Without a considerably more detailed study, the cost of switching on this scale cannot be predicted accurately.

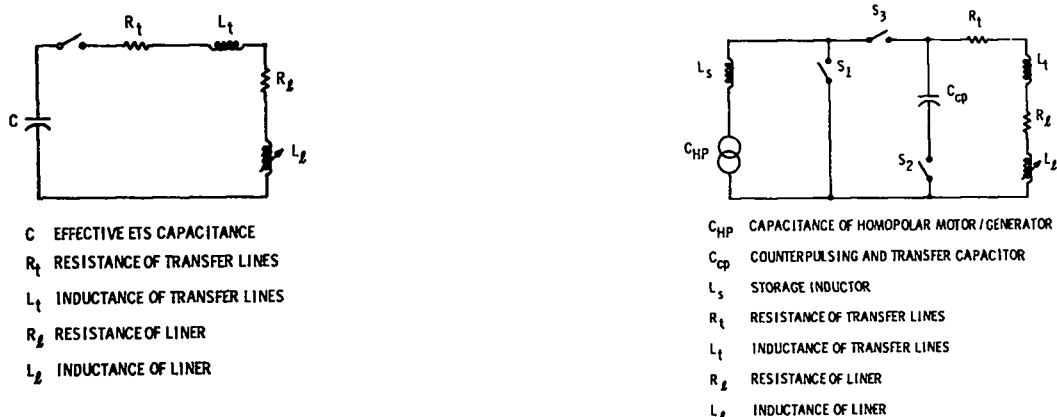


Fig. III-8. Schematic diagrams of capacitive and inductive energy transfer and storage (ETS) systems being considered to drive the FLR liner implosion.

Considering the magnitude of ETS power requirement, the nature of transmission lines should be reexamined. A new interleaved liner leads structure is described in the following section for energy transfer inside the containment vessel. A similar conductor could be envisaged for the permanent external circuitry to provide a compact, low-inductance carrier superior to coaxial cables.

4. Liner Leads. During the initial formulation of the FLR concept⁵ it was assumed that electrical power would be transferred to the liner by a coaxial lead structure or perhaps by circular parallel plates separated by an insulator; these leads concepts are shown schematically in Fig. III-9. Several reasons were subsequently identified that make these approaches unattractive, if not unacceptable, for an FLR.

Typically, the liner must be supplied with ~ 250 MA at 200 kV for ~ 20 μ s. The transfer of near gigajoule energies on a 20- μ s time scale implies that lead inductances between the ETS/switching system and the liner must be small; unacceptable amounts of parasitic energy would otherwise be stored, increasing

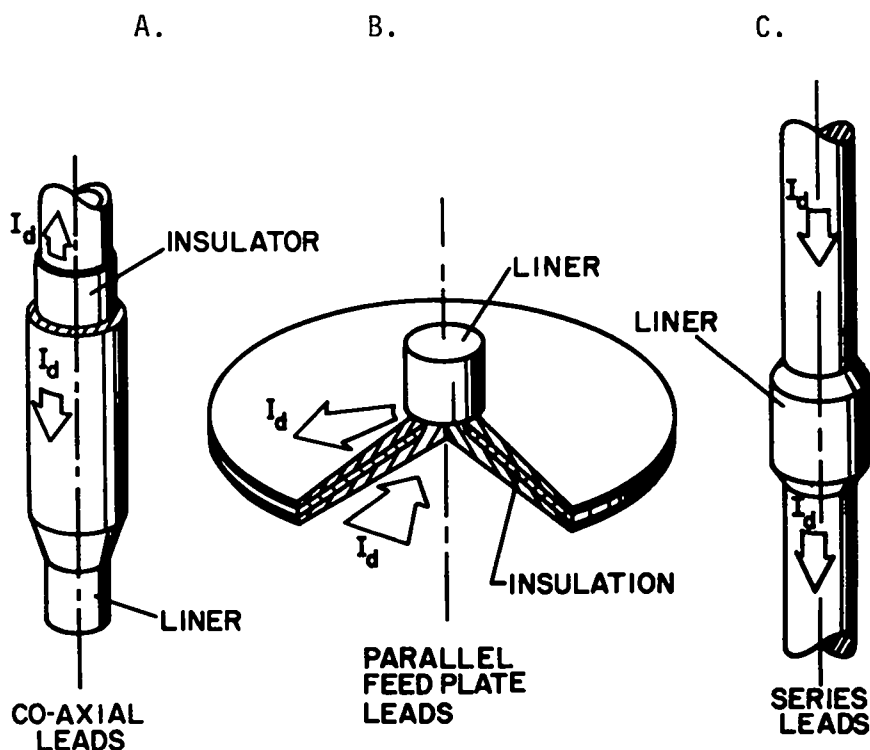


Fig. III-9. Schematic diagram of a range of possible leads configurations using a general coaxial approach. Cost optimization of this general class of leads structure is given in Appendix B.

the ETS energy and voltage requirements. In order that parasitic inductances be maintained small compared to the liner inductance, the distance separating the two conductors must be as small as possible to reduce field energy between conductors. These constraints largely eliminated the concepts shown in Fig. III-9-C, where separate probes of opposite polarity enter the confinement chamber from opposite directions and converge on the liner. One exception would incorporate the switch in the shape of a cylinder that encases the liner at its outer surface. Current would build up in the probes and eventually would be switched during a long pulse; in this case the confinement cavity itself would act as a magnetic energy storage element. The switch around the liner would then be opened and would quickly transfer current to the liner. To date, however, no switch has been conceived that could sustain the high currents and forces required for this approach.

Three additional problems can be identified with the simple coaxial approach depicted in Fig. III-9-A. First, unless the conductors are large and massive, magnetic field pressure between the conductors would rapidly drive the conductors apart, thereby dissipating a substantial fraction of the input power as leads kinetic energy. Second, the optimum leads radius can be computed, which minimizes the expense of recycling conductor and insulator mass as well as energy losses associated with both joule heating and acceleration of the conductor. Generally, as shown in Appendix B, the optimum radius is inconveniently large in comparison to the desired size of the containment vessel. Third, at a point ~ 2 m from the liner, the leads structure that is normally destroyed must be connected to an input conductor that is designed to survive the explosive forces attendant to the liner implosion. A coaxial conductor of radius r_c and carrying a current I_d encounters a field pressure of $\mu_0 I_d^2 / 8\pi^2 r_c^2$. Taking the yield strength of steel to be ~ 400 MPa (58 kpsi) and $I_d = 250$ MA, the reusable coaxial conductor must have a radius in excess of 1.6 m, which is an unreasonably large value and generally is not compatible with the optimization results given in Appendix B. From the viewpoint of energy and materials cost the radial feedplates shown in Fig. III-9-B would be more desirable than the coaxial conductors described above. Serious problems related to joule heating and conductor motion, as well as the difficulty of rapidly handling such an object still exist. These issues are addressed quantitatively in Appendix B.

The overall leads size can be greatly reduced and serious conductor motion alleviated if the interleaved lead structures shown in Fig. III-10 are used. In the interleaved leads concept alternate conductors carry current to and from the liner; insulation, shown in Fig. III-11, is woven between conductors of opposite polarity. The conductor thickness in the azimuthal direction should be no thicker than twice the skin depth, $\Delta = \sqrt{2 \eta \tau / \mu_0}$, for a pulse length τ and resistivity η . The radial thickness $\Delta r = r_o - r_i$ of the conductor is determined by a trade-off between Joule-heating costs ($\propto 1/\Delta r$) and material costs ($\propto \Delta r$). Appendix C describes a quantitative treatment of this optimization between energy and materials costs. As noted in Sec. III.B.1, it is this cost optimization that primarily determines the internal transfer efficiency, η_T^{INT} .

The interleaved conductor can be compared to the coaxial leads through an apparent radial field pressure on each conductor. The coaxial conductor has a field pushing the two conductors apart with a pressure

$$P_{cl} \approx \mu_0 I^2 / 8\pi^2 \langle r \rangle^2 \quad , \quad (III-19)$$

where $\langle r \rangle$ is the average of the two conductor radii. If the interleaved conductors are wider in the radial direction so that $\Delta r = r_o - r_i > \Delta$, it can be shown that the average outward radial pressure on the conductors is given by

$$P_{il} \approx \mu_0 I^2 / N^2 (r_o^2 - r_i^2) \approx \mu_0 I^2 / 2N^2 (\Delta r) \langle r \rangle$$

where N is the total number of conductors. The condition $r_o - r_i > \Delta$ implies $N(r_o - r_i) > \pi(r_o + r_i) \equiv 2\pi \langle r \rangle$. This condition leads to an upper bound on the interleaved conductor pressure given by

$$P_{il} \leq \mu_0 I^2 / 4\pi N \langle r \rangle^2 \quad . \quad (III-20)$$

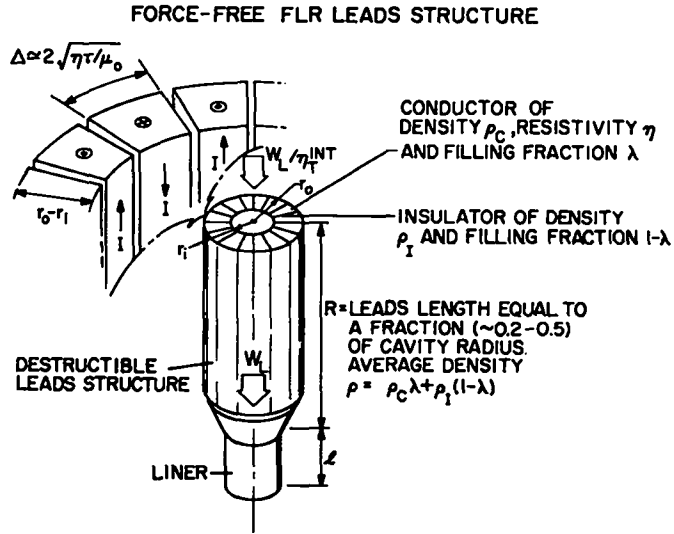


Fig. III-10. Schematic diagram of "force-reduced" interleaved leads structure (Fig. III-1) showing extruded conductor material that would be destroyed each shot and become part of the primary coolant (Li or LiPb). The energy transfer to the liner per se, W_L , is transferred with an efficiency η_{INT} from the containment vessel feedthrough. This geometry and the value of η_{INT} is determined on the basis of optimal costs (Appendix C).

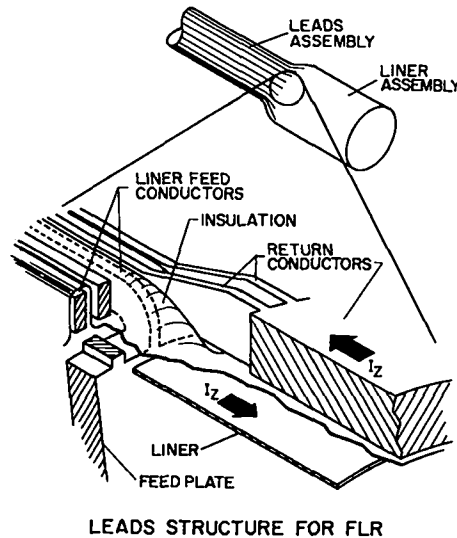


Fig. III-11. Detailed view of attachment of "force-reduced" interleaved leads structure to the liner.

The radial pressures on the two systems are related as follows

$$P_{i\ell} < (2\pi/N)P_{c\ell} \quad , \quad (III-22)$$

when the average radii for both the coaxial and interleaved systems are equal. Typically, N can be made on the order of 100, and the radial pressure on interleaved leads, therefore, can be made negligible when compared to coaxial leads. Likewise the kinetic energy imparted to interleaved leads would be insignificant.

The interleaved leads approach eliminates the leads kinetic energy as a design constraint, and the crucial constraints become the costs of ohmic heating (i.e., added ETS requirement or decreased η_T^{INT}) and materials destruction (i.e., cost of materials fabrication and replacement). Although this cost optimization is described in detail in Appendix C, given below is a brief description of the energy versus materials trade-off for the "force-reduced," interleaved leads concept.

The resistance R_L per unit length of leads is given by (Fig. III-10)

$$R_L (\text{ohm/m}) \approx 4\eta/N\Delta(r_o-r_i) = 2\eta(\Delta+\Delta_I)/\pi\Delta\langle r \rangle (r_o-r_i), \quad (III-23)$$

where Δ must be twice the skin depth, and Δ_I is the insulator thickness. Assuming a sinusoidal pulse, the ohmic heating per meter of lead length is

$$W_{OHM} \approx R_L I_d^2 \tau / 2 \approx \eta(\Delta+\Delta_I) I_d^2 \tau / \pi\Delta\langle r \rangle (r_o-r_i) \quad . \quad (III-24)$$

The conductor mass requirement per meter of lead is given by

$$M_C = 2\pi\rho_C\Delta\langle r \rangle (r_o-r_i)/(\Delta+\Delta_I) \quad , \quad (III-25)$$

and the mass of the leads insulator is given by

$$M_I \approx 2\pi\rho_I \langle r \rangle \Delta_I [1 + (r_o - r_i)/(\Delta + \Delta_I)] \quad , \quad (\text{III-26})$$

where ρ_C and ρ_I are conductor and insulator densities. Cost factors can be assigned to W_{OHM} , M_C , and M_I , and the radial thickness $(r_o - r_i)$ can be adjusted to minimize the total leads cost; this optimization is described in Appendix C. It should be noted that within reasonable limits, the average radius, $\langle r \rangle$, can be fixed, and an optimization can be performed with respect to $r_o - r_i$; it is no longer necessary to optimize using the overall size, as in the cost of coaxial conductor (Appendix B).

Figure III-12 gives the results of the simple cost optimization described in Appendix C. Under the assumption that materials costs are not incurred for the leads conductor beyond the initial capital investment and that the

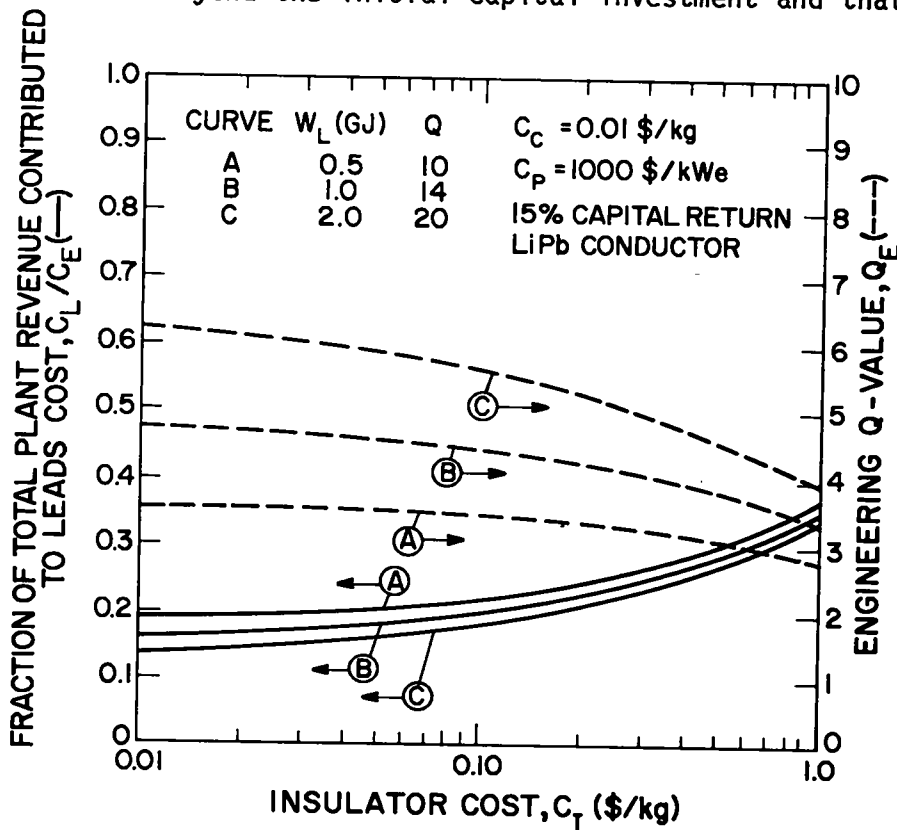


Fig. III-12. Dependence of leads cost C_L (relative to net power cost C_E) and the engineering Q-value Q_E on the unit cost of leads insulator C_I (\$/kg) for a leads conductor recycle cost C_C of 0.01 \$/kg. The liner energies W_L and liner Q-value Q are constrained (Re: Appendix C).

conductor can be recovered and recycled at a cost of 0.01 \$/kg, Fig. III-12 gives the dependence of the total leads cost, relative to the net plant revenue, on the total cost of the insulator. Figure III-12 also gives a similar dependence for the engineering Q-value Q_E and a range of liner yields (W_L, Q) . In deriving these curves the relationship $Q = \xi(W_L/\ell)^{1/2}$ has been used to relate analytically the liner Q-value and the liner energy per unit length W_L/ℓ ; the constant ξ is derived from the impulse-momentum theorem and shows good agreement with the predictions of both the LNRBRN and CHAMISA codes.¹⁷ Generally, if the insulator costs can be held below ~ 0.10 \$/kg, the total leads cost will be comparable to a "fuel cost," amounting to $\sim 20-30\%$ of the plant revenue, and the decrease in plant efficiency required to optimize the plant revenue is not significant.

The optimization procedure used to arrive at Fig. III-12 is based on an optimum cross-sectional area of the interwoven leads structure that will maximize total plant revenue (re: Appendix C). Generally, the optimum leads area is sufficiently small to cause melting sometime during the energy transfer. Appendix C treats the case where the leads are constrained to remain solid throughout the implosion, rather than selecting a conductor area that maximizes plant revenue. These results generally are more pessimistic than those presented in Fig. III-12 and are discussed in Appendix C.

Last, it is emphasized that the results presented here represent a local or "point" optimization that focuses on the leads and treats all other plant costs as a lumped parameter ($C_p = 1000$ \$/kWe with 15% capital return). Once more detailed designs are available for all crucial components, a comprehensive cost optimization must be performed.

5. Neutronics Analysis. Like other technology areas for the FLR, only scoping studies have been made with respect to the neutronics design. The purpose of the neutronics studies performed to date is threefold: (a) to resolve the relationship between tritium breeding in the Li (or LiPb) blanket spray that would surround the liner prior to implosion, the composition and volume fraction of the spray, and the size of the containment vessel as dictated by stress considerations; (b) to determine the energy density profiles in both the Li spray and at the first structural wall; (c) to resolve the degree to which nuclear heating occurs within the liner and leads structure and to determine the effects of this heating on the liner dynamics and the amount of destroyed leads. Because of the complex geometry associated with

the liner leads, liner/leads penetration, and blast containment (Fig. II-1), a Monte Carlo approximation was adopted; this approach sacrifices spatial resolution for more flexibility in describing the time-dependent, asymmetric problem.

The continuous-energy Monte Carlo code MCNP³¹ was used for the idealized neutronics analysis. This code employs any number of cells and uses standard variance reducing techniques (optional), which include particle splitting, Russian roulette, and path-length stretching. Provisions are also made for forcing collisions in designated cells, obtaining flux estimates at point detectors, and for calculating reactions in small regions using track-length estimates. Specification of a source particle consists of a geometry location, angular description, energy, time, and particle weight, with probability distributions being designated for any of these variables. Additional information on the MCNP calculational procedure is found in Appendix D.

Figure III-13 depicts the MCNP geometry used to model the liner, leads, leads penetration, lithium-spray cavity, and the containment walls; Table III-I identifies each region used in the neutronics approximation. A vacuum

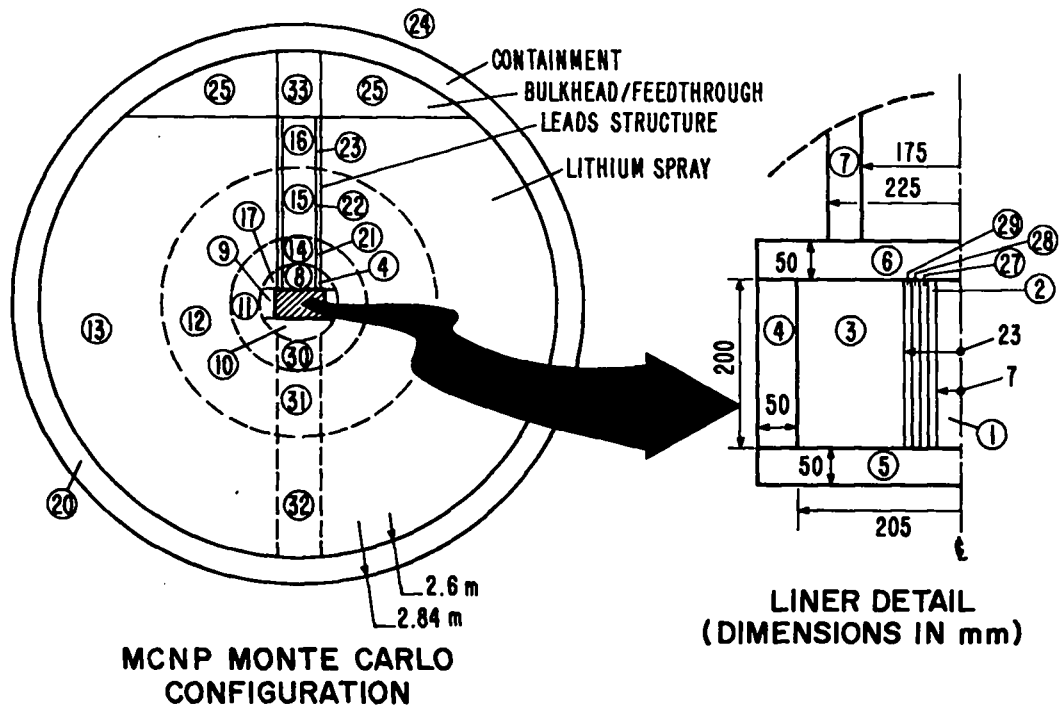


Fig. III-13. Neutronics model used to compute nuclear heating via MCNP Monte Carlo code. Refer to Table III-I for zone characteristics.

TABLE III-I
DESCRIPTION OF FLR REGIONS USED IN MCNP MONTE CARLO
NEUTRONICS CALCULATION (FIG. III-13)

<u>Region</u>	<u>Description</u>	<u>Composition</u>
1	Compressed Plasma	Void (Source)
2	Liner	Cu (2.5 theoretical density)
3	--	Void
4	Return Conductor	Cu or LiPb
5	Bottom Endplug	Cu or LiPb
6	Top Endplug	Cu or LiPb
7	Electrical Lead	Cu or LiPb
8-17	Lithium	Li (25-50 v/o)
18-19	No Designation	--
20	Containment Vessel	Fe
21-23	Electrical Lead	Cu or LiPb
24	--	Void
25	Feedthrough/Top	Fe
26	No Designation	--
27-29	Liner	Cu (2.5 theoretical density)
31-32	Lithium	Li (25-50 vol%)
33	Feedthrough/Top	Fe

boundary condition was imposed outside the containment vessel, since shielding computations are not of primary interest here. Gamma/neutron heating and tritium breeding were computed for each Monte Carlo cell. The time-dependent 14.1-MeV neutron source from cell region [1] was generated by the LNRBRN code (Appendix A) and is depicted on Fig. III-14, which also gives the cumulative gamma-ray and neutron energy deposition for a Cu/LiPb liner assembly; for all cases the liner per se was copper. The liner configuration depicted on Fig. III-13 corresponds to condition expected at peak compression with the massive return conductors (Cu or LiPb) assuming the initial (~ 0.2 -m radius) position. Taking the melting energy as that needed to melt a liner starting from room temperature (610 MJ/m^3 for LiPb and 5.92 GJ/m^3 for Cu), Fig. III-14 indicates that melting of the liner from nuclear heating alone will probably occur prior to peak compression; this inference is approximate

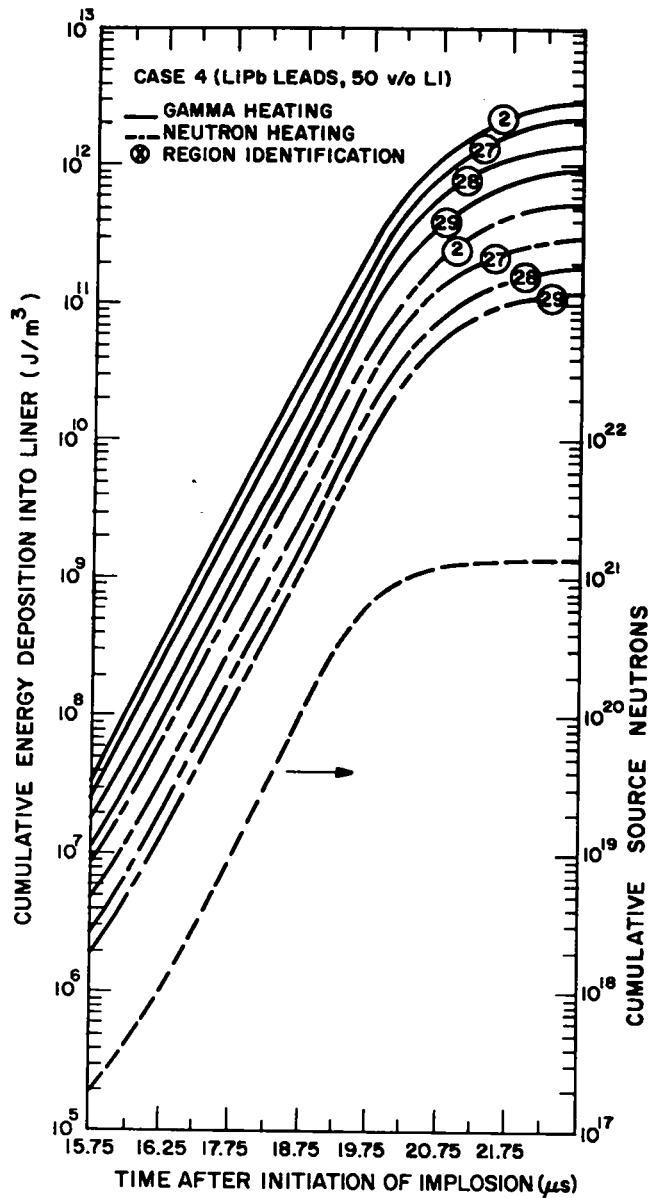


Fig. III-14. Time-dependence of integrated neutron and gamma heating in a compressed copper liner for the regions indicated (Table III-I). Shown also is the cumulative neutron source (14.1-MeV) integrated in time. Time is measured relative to the beginning of the liner implosion.

in that MCNP does not model the liner dynamics, but pessimistically assumes a thickness and density at peak compression. Figure III-I5 gives the radial distribution of total nuclear heating in a copper liner for cavity volume fractions of lithium equal to 0.25 and 0.40.

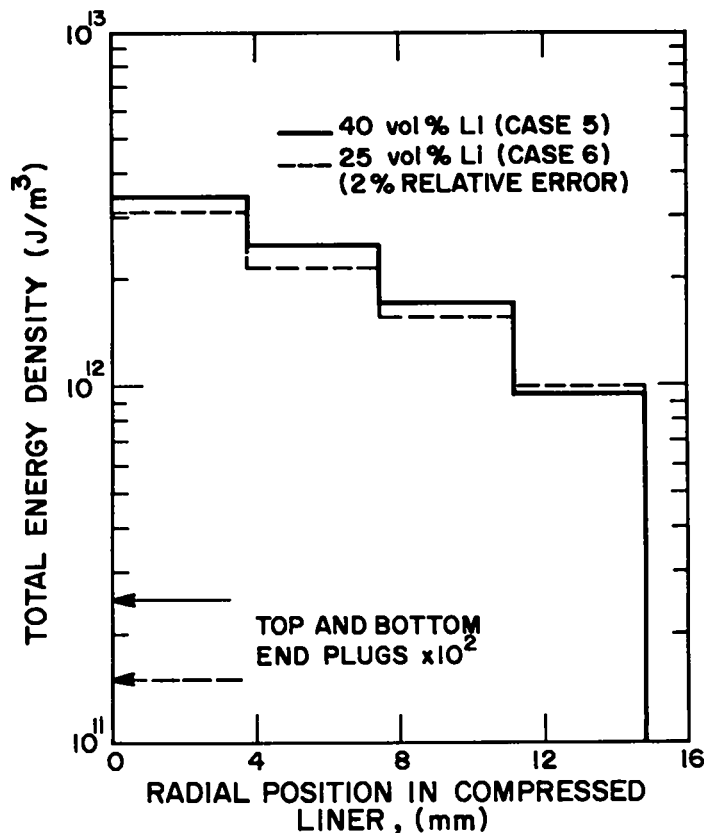


Fig. III-15. Radial distribution of total energy density deposited into a copper liner at peak compression for the volume percentages of Li-spray coolant shown. The 50 vol% case follows closely the distribution shown for the 40 vol% case. The energy density in the top and bottom endplug region is also shown (Re: Fig. III-13).

Table III-II summarizes the key results for the six MCNP calculations. Generally, tritium breeding in a lithium spray of volume fraction in excess of 0.25 presents no problem. As expected, the lithium spray itself is a poor energy multiplier, but some variation is seen with the liner assembly material (LiPb versus Cu); this variation is seen primarily in the tritium breeding ratio and reflects the higher (n,Nn) reaction cross section for lead. The net number of neutron crossings at the steel vessel is also shown on Table III-II, and the lithium spray is seen to be inadequate as an efficient neutron shield/absorber for the containment vessel. For instance 7.8% and 14.0% of the starting neutrons leave, respectively, the outer boundary or cross the inner boundary of the steel vessel for case 4 (50 vol% lithium in the cavity, LiPb lead/liner structure). Table III-III gives the spectrum and the track length per unit volume (i.e., neutron flux) at the steel containment

vessel: this flux generally peaks in the 10-to 100-keV energy range. For a 10-s pulse rate, average neutron fluxes in the range $\sim 5(10)^{18}$ n/m²s with this energy spectrum (Table III-III) would be expected.

TABLE III-II
SUMMARY OF SIX MCNP (MONTE CARLO) NEUTRONICS COMPUTATIONS
MADE FOR FLR CONFIGURATIONS DEPICTED IN FIG. III-13(a)

Case	Liner/Leads Material	Lithium Volume Fraction in Cavity	Tritium Breeding Ratio	Total Neutron Multiplication	Fraction Starting Neutrons Leaving System	Net Number of Neutrons Crossing Inner Surface of Vessel 10^{20}	Total Energy Multiplication
1	Cu	50	1.247	1.379	0.090	1.441 (0.15) ^(b)	1.111
2	Cu	40	1.113	1.340	0.130	2.845 (0.21)	1.121
3	Cu	25	0.904	1.375	0.293	5.475 (0.43)	1.040
4	LiPb	50	1.472	1.263	0.078	1.718 (0.14)	1.113
5	LiPb	40	1.365	1.270	0.141	2.410 (0.21)	1.099
6	LiPb	25	1.098	1.270	0.294	8.994 (0.43)	1.040

(a) Statistical variations are small, amounting to significant variations only in the third place.
(b) Fraction of starting neutrons.

TABLE III-III

ENERGY SPECTRA FOR THE LiPb LINER ASSEMBLY AND 50 vol% LITHIUM CAVITY (CASE 4, TABLE III-II), AND FOR THE Cu LINER ASSEMBLY AND 25 vol% LITHIUM CAVITY (CASE 3, TABLE III-I)

Upper Energy Limit (MeV)	Track Length Estimate of Flux (n/m ² /shot) 10^{14} (Case 3)	(Case 4)
10-4	13.175	--
10-3	23.073	8.715
10-2	50.141	20.48
10-1	149.58	48.08
10 ⁰	101.60	23.29
101	7.741	1.975
15	1.618	0.1808
Total	346.85	102.71

The radial distribution of both neutron and gamma-ray heating in the lithium spray and leads structure is shown in Fig. III-16 for cases 3 and 5 depicted on Table III-II. The first ~ 0.7 m of LiPb leads structure is expected to melt solely from nuclear heating, but little or no vaporization of the leads structure is anticipated. The total heating (nuclear, liner kinetic energy, alpha particle, radiation) within a 2.6-m-radius cavity filled to 40-50 vol% with liquid lithium spray is expected to raise the lithium temperature on the average by 55-60 K with little or no local vaporization. The spatially resolved dynamics of the pulsed energy transfer to a liquid spray in the possible presence of hydrodynamic shocks and shock-mitigating processes, however, has not been fully resolved. This subject is addressed by preliminary computation in the following section.

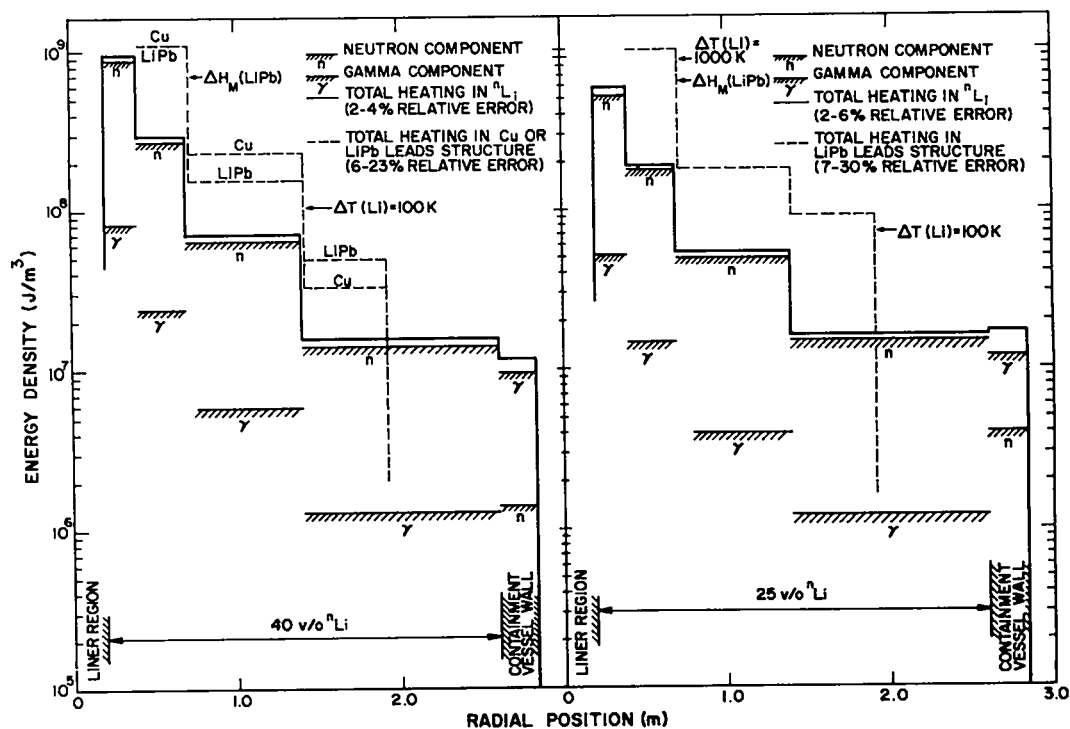


Fig. III-16. Radial distribution of total neutron and gamma energy density within a 40 vol% and 25 vol% lithium-spray blanket (cases 5 and 6, Table III-II). Shown also is the total energy density deposited into the Cu or LiPb leads structure. The quantity $H_M(\text{LiPb})$ indicates the energy density required to melt the conductor material, whereas $T(\text{Li}) = 100$ indicates the energy density required to raise the coolant 100 K. All energy densities correspond to the total region volume.

6. Blast Containment. As described in the summary description of the FLR (Sec. II) and as indicated in the neutronics section (Sec. III.A.5), a Li (or LiPb) spray or "rain" would be injected around the liner to absorb a major part of the nuclear and kinetic energy release. A close coupling exists, therefore, between the requirements of radiation shielding, tritium breeding, thermal energy extraction, and blast containment/mitigation. Insofar as the latter issue is concerned, a number of coolant/blast-mitigating configurations have been considered:⁹ bubble-impregnated liquid-metals, vacuum detonations, fluidized beds of blast-mitigating powders, liquid-metal first-walls, and liquid-metal sprays. Although the blast containment requirement shows a number of similarities with beam/pellet fusion concepts,³²⁻³⁴ the following significant differences are noted: a) the primary energy input to the liner is from one direction and does not require vacuum; b) the implosion time scales are considerably longer (μ s versus ns); c) greater quantities of mass are disturbed and set into motion by the liner implosion; d) the possibility of large pieces of debris impacting structural components is greater for the FLR.

Approximately 20% of the fusion energy from the ~ 2 - μ s burn would be deposited in and near the liner by alpha particles and radiation. In addition, roughly 20% of the neutron energy is given directly to the dense, compressed liner (Sec. III.B.5). Last, approximately 1/Q of the fusion yield is retained as liner kinetic energy. Consequently, an energy equal to $\sim 50\%$ of the fusion yield will appear in the general vicinity of the liner; this corresponds to ~ 1.5 GJ for the low-yield case given on Table II-I. The remaining $\sim 50\%$ of the released thermal energy would be deposited in the lithium spray according to the distribution given by Fig. III-16. Although the sudden but distributed release of neutrons can lead to shocks in a liquid or liquid-gas mixture,³² the $\sim 50\%$ release near the liner position will probably present a more serious containment problem and, consequently, has been made the focus of the blast-containment computations.

As a first step in quantifying the blast-containment problem, existing experimental data³⁵ have been employed in conjunction with a simple analytical model based upon the "virial theorem."^{36,37} This simple approach is described in Appendix E and has been used primarily to examine sudden, large energy releases in either vacuum or gas-bubble-laden liquids. For the latter case, substantial masses of liquid can be set in motion, leading to

considerable pressure amplification at the containment walls (Appendix E). After a brief description of the simple containment models, this section describes the results of more detailed structural/mechanical computations.

In the simplest containment model the blast energy W_B deposited at the initial liner position is assumed to thermalize uniformly as an ideal gas within the spherical containment vessel of radius R and wall thickness ΔR . The circumferential stress in a spherical, thin-shell pressure vessel is given by

$$\sigma_{\theta} = W_B / 4\pi R^2 \Delta R \quad , \quad (\text{III-27})$$

and the corresponding strain is³⁸

$$\epsilon_{\theta} = [(1-\nu) \sigma_{\theta} + \nu \sigma_r] / E \quad , \quad (\text{III-28})$$

where E is Young's modulus, ν is Poisson's ratio, and σ_r is the radially directed stress. In this discussion σ_{θ} is taken as tensile and σ_r is compressive (both positive). These expressions predict well the results of experiments which used small explosive charges (few kg) in relatively small spherical vessels ($R \approx 0.5$ m) under vacuum (Appendix E). If, however, similar tests were performed either at atmospheric pressure or in the presence of blast-mitigating media (e.g., vermiculite), significant deviations from the virial-theorem approach (Eq.(III-27)) are observed. For the range of W_B , R , and ΔR investigated, detonations carried out in air at atmospheric pressure gave shock-induced stresses, that were about four times the predictions of Eq. (III-27). The use of energy-absorbing materials reduced the stresses approximately by a factor of two. It is emphasized here that although blast-mitigation is invoked for the FLR, theoretical understanding of these processes is meager. Whether or not a blast-mitigating mechanism is available in the liquid-metal spray evoked for the FLR remains to be demonstrated. If blast-mitigation proves unfeasible with the Li spray the use of "vermiculite-like" materials which are lithium bearing (Li_2O , LiAlO_2 , etc.) may be required in the form of a fluidized bed.⁹

Of primary interest to quantifying the blast-containment problem, beyond the limits of the simple models described in Appendix E, are the time-resolved shock spectra produced at the vessel wall by the equivalent blast-energy release W_B . The computer code PAD³⁹ was used to compute in one-

dimensional (spherical) Lagrangian coordinates the motion of explosive gases and the mechanical response of the spherical container. Radiation heat transfer and thermal conduction within the ~ 1 -GJ blast created at the initial liner location were not considered, nor were asymmetry effects that may be induced by the liner-leads structure. Consistent with the sample operating points summarized in Table II-I, blast energies W_B in the range 0.70 to 2.26 GJ were considered. The results of the PAD computations can be accurately scaled to other vessel sizes and energy releases according to Eqs. (III-27) and (III-28), or the results of a more detailed analytic formulation given in Appendix E could be used.

For most computations $W_B = 1.4$ GJ. This energy was assumed to be deposited in a sphere with the density of solid copper ($8.92(10)^3$ kg/m³) located at the center of containment vessel. For the purposes of this analysis M is defined as the mass of destroyed liner and leads structure that shares the energy W_B and contributes ultimately to the shock spectrum at the container walls. Based upon the scaling of experimental data from blasts in evacuated vessels (Appendix E), the radius R of the containment sphere is estimated to be 2.6 m if its wall thickness ΔR is 0.15 m when $W_B = 1.4$ GJ. The density and Young's modulus of the containment vessel are taken to be those of 304 stainless steel ($\rho = 7.86(10)^3$ kg/m³, $E = 160$ GPa). The vessel was not allowed to yield in the PAD computations. When the yield stress is exceeded in a computational result, ΔR is scaled according to Eq. (III-27) to reduce the stress to acceptable levels.

The first PAD computations were made for $W_B = 1.4$ GJ in an evacuated sphere. Two time histories of radial and circumferential stresses (σ_r and σ_θ , respectively) are shown in Fig. III-17 for blast-product masses M of 25 kg and 200 kg, respectively. The vessel oscillates at a frequency of $f_v = 475$ Hz that is independent of ΔR in accordance with the thin-shell approximation. The reverberating gas within the vessel oscillates at a frequency f_g proportional to $M^{-1/2}$. Since energy losses are not included in these computations, the radial stress asymptotically approaches the equilibrated pressure corresponding to a uniform distribution of the initial blast energy W_B .

The maximum circumferential or hoop stress, σ_θ , is plotted as a function of M in Fig. III-18. This stress is nearly constant for small values of M , where $f_g \gg f_v$. For this situation the gas pressure at the vessel wall,

σ_r , oscillates and is ultimately damped to the pressure of a quiescent gas with energy W_B . Meanwhile, the vessel moves nearly as a harmonic oscillator from a condition of zero hoop stress to a maximum stress. The average hoop stress will support the pressure of a quiescent gas of energy W_R (Eq. (III-27)). Since the shell oscillates harmonically from zero to a maximum, the

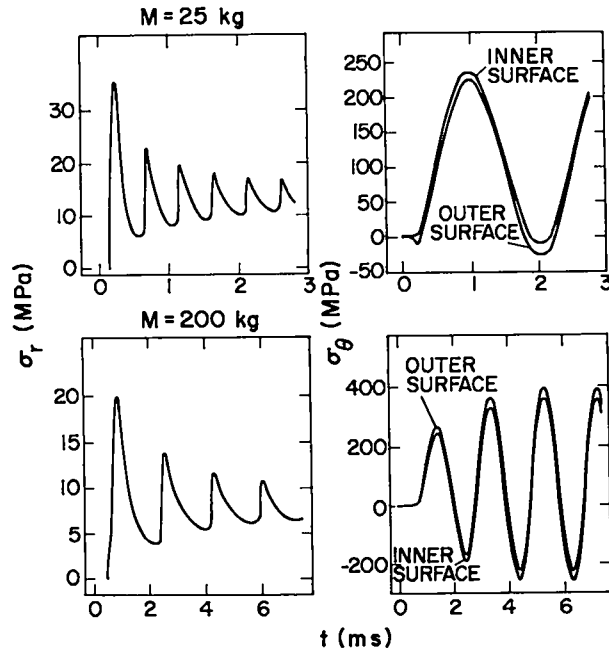


Fig. III-17. Time dependence of radial (σ_r) and hoop (σ_θ) stress for a vacuum energy release of 1.4 GJ in a spherical vessel of 2.6-m radius and 0.15-m wall thickness. The mass that contains this energy is M . These results can be scaled to other vessel dimensions ($R, \Delta R$) by Eq. (III-27).

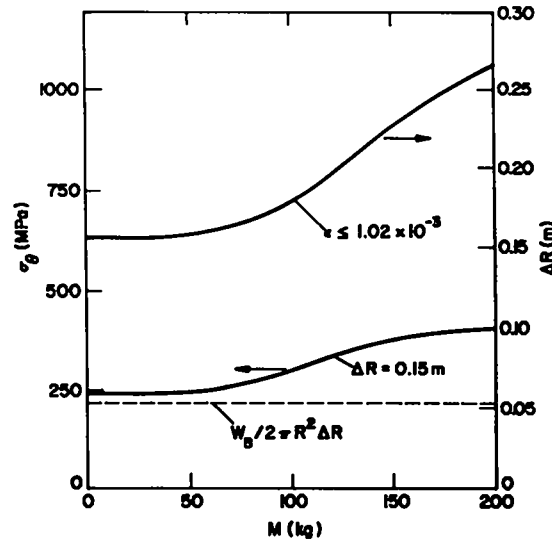


Fig. III-18. Dependence of maximum hoop stress on mass M assigned to a vacuum release of 1.4 GJ energy for either fixed maximum strain ϵ or a fixed vessel thickness ΔR . The vessel radius is $R = 2.6\text{m}$. Dashed line indicates virial theorem prediction, Eq. (III-27).

peak stress is approximately twice the average stress. This approximation fails when the explosive gas and shell come into resonance at $f_g \approx f_v$, as seen for the $M = 200$ -kg case in Figs. (III-17) and (III-18). In this case the maximum stress is 77% higher than the value given by the above-mentioned approximation.

Based on fatigue data for stainless steel,⁴⁰ as interpreted for liner blast containment,⁹ a peak strain of $\epsilon_\theta = 1.016 \times 10^{-3}$ appears acceptable for a 10-yr life ($2.5(10)^7$ shots for an 80% plant factor) at 800 K. By taking $\nu = 0.29$, $\sigma_r = 20$ MPa, and $E = 160$ GPa, Eq. (III-28) is used to give the maximum acceptable circumferential stress σ_θ ; the vessel wall thickness ΔR is then scaled to an appropriate value. For the $M = 25$ and 200-kg cases in Fig. III-17 the ΔR values with acceptable fatigue strain are 0.16 and 0.27 m, respectively.

The PAD code was also used to model blast containment in a liquid-gas mixture. It has been proposed that both liner³ and laser³² fusion reactors be immersed in a Li (or LiPb) spray for tritium breeding and neutron moderation. If a fast liner were immersed in a purely liquid environment, the shock wave created in the liquid would present intolerable stress amplification at the containment walls (Appendix E). On the other hand the shock may be substantially mitigated by mixing a compressible gas with the liquid.³² The time histories of three PAD computations are shown in Fig. III-19. The blast energy W_B is again fixed at 1.4 GJ, and the 304 stainless steel vessel parameters are, again, $R = 2.6$ m and $\Delta R = 0.15$ m. A LiPb mixture of $9.4(10)^3$ kg/m³ density at ~ 870 K is dispersed through the vessel with a volume fraction of f . The volume fraction $1-f$ is filled with helium at atmospheric pressure. The liquid is assumed to be incompressible, and the helium is regarded as an ideal gas with the heat capacity ratio γ treated as a free parameter. Hence, the helium gas when subjected to a volumetric compression κ would obey the following relationships: $P/\kappa^\gamma = \text{constant}$ and $T/T_0 = \kappa^{\gamma-1}$, where T_0 is the initial (pre-shot) helium temperature. An artificial viscosity term in the PAD computation produces non-adiabatic heating across the shock fronts which traverse the LiPb/He mixture.

The radial and hoop stresses as functions of time are shown in Fig. III-19 for three γ - f couplets. These results show the sensitivity of the vessel stress response to the assumed value of liquid volume fraction f and

the γ values of the gas phase. For $\gamma = 5/3$ all compressive energy entering the gas-liquid mixture would ultimately heat the gas. Correspondingly, compression of the gas would be isothermal if $\gamma = 1$, simulating an immediate transfer of thermal energy to the liquid metal. The first example in Fig. III-19 ($\gamma = 1.4$ and $f = 0.2$) results in a peak hoop stress of $\sigma_{\theta} = 1200$ MPa for $\Delta R = 0.15$ m or a requirement that ΔR be increased to 0.9 m, according to Eq. (III-28), if a 10-yr fatigue constraint at 800 K is imposed. Unlike the vacuum containment cases (Fig. III-17), the greatest wall stresses occur in a short pulse followed by smaller oscillatory stresses.

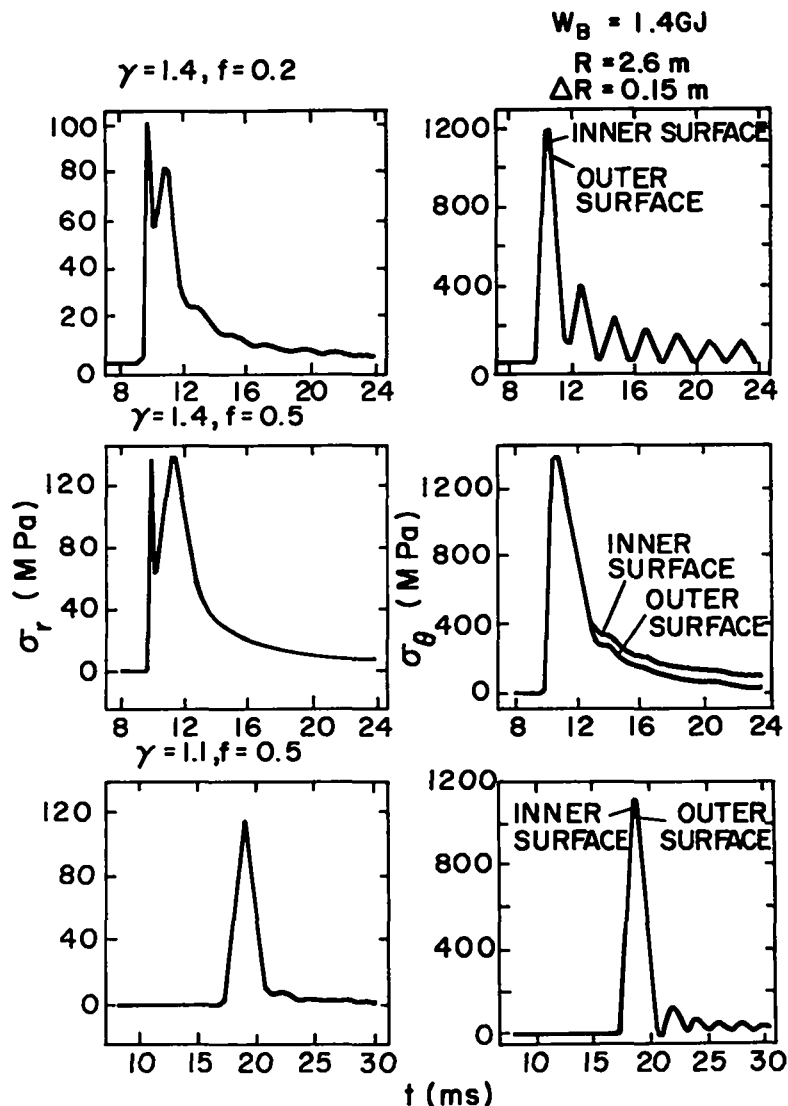


Fig. III-19. Time-dependence of radial (σ_r) and hoop (σ_{θ}) stress for 1.4 GJ released to a $M = 25$ -kg mass in a gas (He)/liquid (LiPb) mixture contained in a $R = 2.6$ -m, $\Delta R = 0.15$ -m spherical vessel that is initially pressurized to 0.1 MPa. The initial volume fraction of liquid is f , and γ is the heat capacity ratio for the gas.

For the second case given on Fig. III-19, γ is again taken to be 1.4, but the liquid volume fraction is increased to 0.5. The peak hoop stress increases to 1400 MPa for $\Delta R = 0.15$, or a requirement of $\Delta R = 1.2$ m results if a 10-yr fatigue constraint is imposed at 800 K. Simple scaling arguments indicate that the momentum impulse at the wall, $\int \sigma_r dt$, will increase roughly as $f^{1/2}$, but the associated increase in impulse duration makes σ_θ relatively insensitive to f . This prediction is borne out by the 17% increase in σ_θ when f increases by 150%.

The third example in Fig. III-19 shows the effects of a reduction in γ from 1.4 to 1.1 while f is held at 0.5. This model simulates the rapid transfer of shock energy to the liquid metal (i.e., the $\gamma \rightarrow 1$ limit). Since the temperature rise in the helium is smaller for a given compression when γ is decreased from 1.4 to 1.1 the liquid-gas mixture is more easily compressed. A somewhat smaller momentum is transferred to the liquid metal, and a reduced stress occurs at the vessel wall; this hoop stress equals 1100 MPa, and corresponds to $\Delta R = 0.9$ m for an acceptable stress.

All cases shown in Fig. III-19 exhibit a sharp stress pulse that lasts about 3 ms. This intense, initial pulse could be reduced in peak intensity and spread out in time by a blast-attenuating structure attached to the inside wall of the containment vessel as indicated in Fig. II-1. For example, the shock velocity is ~ 100 m/s and the particle velocity is ~ 50 m/s at the time the shock impacts the structural wall. By placing rib-like structures on the inner walls that are 0.3 m high and filling 50% of the local volume, the duration of impact may be increased by a factor of ~ 2 , which in turn would cause the maximum σ_θ to be reduced by a comparable amount. Therefore, blast attenuators may significantly reduce the overall structural requirements placed on the containment vessel. The concept of physical shock attenuators, however, must be examined by more detailed analysis.

The foregoing examination of blast containment is based on a number of simplifying assumptions. Present theoretical predictions and extrapolation of the existing data base should be treated as imprecise until experimental tests are made for much higher blast energies. The general scale of blast requirements has been quantified, however, and appears to be technologically feasible. Generally, 2.5-to 3.0-m-radius containment vessels with 0.3-to 0.5-m-thick walls appear adequate to contain the ~ 1.5 GJ of thermal energy expected to be released every ~ 10 s by the FLR; these dimensions appear

adequate for a ~ 10 -yr fatigue life at 800 K for stainless steel. By proper vessel design (physical shock attenuators) and selection of blast-mitigating media, the uncertainties associated with the models used to generate these results can be reduced; based on present knowledge it is doubtful that either R or ΔR will be decreased for the low-yield design point given on Table II-I. The need to build more conservatism into the vessel design will become more apparent when the effects of long-term radiation damage and the realities of actual engineering structures (penetrations, weldments, etc.) are examined.

The neutronics computations given in Sec. III.B.5 are based on a lithium-helium mixture inside the containment vessel rather than a LiPb-He system. Blast computations have not been made for the Li case, but results from such an exercise would surely fall between the vacuum versus LiPb extremes considered above. Although the lithium density is much less than that of the LiPb (475 kg/m^3 versus 9400 kg/m^3), the stress expected for the Li-He mixture would not be correspondingly close to the vacuum case, since a shock wave is established even in a light-weight fluid. As noted previously, blasts in air may produce four times as much stress as vacuum contained blasts. For simplicity it is assumed that a 1.4-GJ blast in pure lithium and helium at atmospheric pressures and volume fraction $f = 0.4$ requires a wall 0.3 m thick with a ribbed inner wall. It is also assumed that the scaling of Eq. (III-27) applies for other energies.

7. Heat Transfer. As seen from Table III-I the following distribution of thermal energy release to the blast cavity is expected for the low-yield case: enhanced fusion yield = 3920 MJ; liner kinetic energy = 336 MJ; leads losses = 37 MJ; plasma preparation = 7.5 MJ, which gives a total thermal release of 4.3 GJ to the blast cavity. Figure III-20 gives the radial distribution of the nuclear energy density (neutrons plus gamma rays) deposited into a lithium spray of three possible volume fractions (25, 40, and 50 vol%), as determined by the MCNP Monte Carlo calculations described in Sec. III.B.5. Approximately 1.5 GJ would be deposited in or near the initial liner volume (Sec. III.B.6), which amounts to $5.9(10)^{10} \text{ J/m}^3$ in the region $r = 0$ to 0.2 m indicated on Fig. III-20.

Neglecting the heat of fusion associated with the leads structure, 4.3 GJ is capable of uniformly increasing the 50 vol% lithium in the 2.6-m-radius vessel by 59 K. As indicated in Sec. III.B.6, however, the means by which this highly anisotropic energy-density distribution nondestructively relaxes

to an isothermal state that is 59 K higher in temperature is by no means resolved, and considerably more analytical work is required. The shocks set up in the lithium spray will play an important role in distributing the coolant temperature rise; the question remains as to the degree to which both mechanical and thermal energy is transferred to the containment vessel.

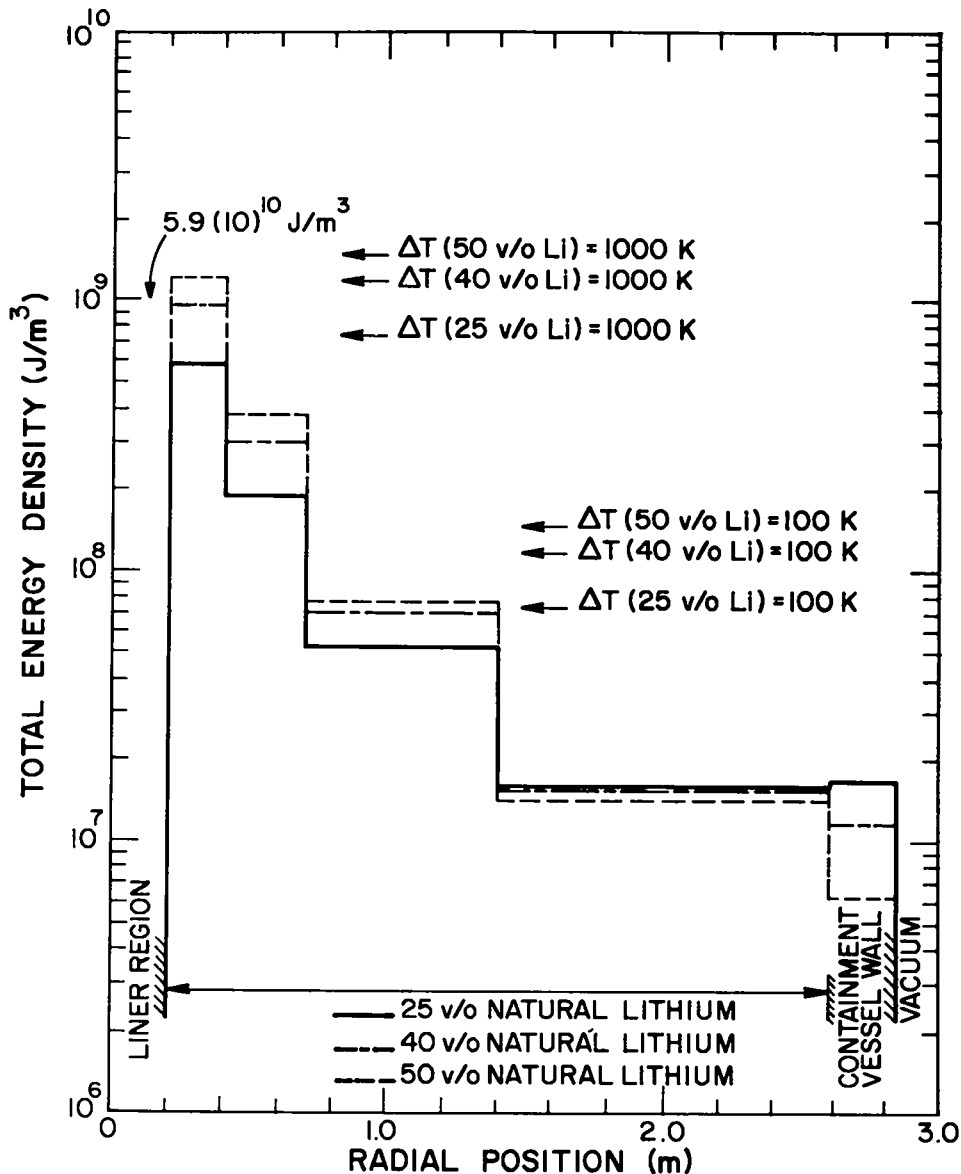


Fig. III-20. Radial distribution of total neutron and gamma-ray energy density in the lithium spray for three volume fractions of lithium (cases 4-6, Table III-II). All energy densities correspond to the total region volume. Indicated for the three cases are the energy densities corresponding to 100 and 1000 K adiabatic temperature rise. The energy density averaged over the initial liner volume is $5.9(10)^{10} \text{ J/m}^3$ for the low-yield case in Table II-I.

Although the complex processes which govern the pulsed heat transfer within the FLR blast cavity have not been subjected to quantitative analysis, a qualitative description is given below, which could serve as the basis of analytic modeling. The exponentially decreasing neutron and gamma-ray heating rate in the lithium-spray blanket causes a large (~ 300 K) radial temperature gradient in the dispersed lithium coolant spray. This large thermal gradient is further aggravated by the high heat flux at the lithium surface near the vaporized liner. A portion of the lithium in the region adjacent to the liner could also be vaporized to a depth of about 0.20 m from this heat flux. This hot "bubble" of vaporized Li and liner materials could expand radially outward. The cooler lithium droplets would be accelerated radially by the ensuing shock wave, which also compresses the interstitial gas until complete contact with the containment vessel wall occurs. As the impact pressure loading is absorbed in the vessel, it will rebound, throwing the lithium toward the center of the cavity. The compressed gas would expand as the pressure is relieved and would tend to accelerate the liquid in all directions, although it is expected that dispersion as droplets towards the cavity center would principally occur. The liquid lithium would traverse the vaporized material at the center, mixing and condensing the vapor on the droplets. The coolest liquid adjacent to the vessel wall may not participate fully in this stage of mixing, but will tend to fall more rapidly into the sump (Fig. II-1) than the less dense central region. Further mixing will take place in the shear layer between this cooler and the hotter (perhaps a still partially vaporized) material at the center. With proper design of spray nozzles, it should be possible to tailor the lithium volume fraction as a function of vessel radius in order to optimize the efficiency of energy absorption and subsequent mixing. A void space adjacent to the liner would give a larger heat transfer area at this point and may lead to reduced heat fluxes, thereby reducing the vapor fraction. A low lithium fraction near the vessel wall would increase the volume of compressed gas and the "rebound" potential from the wall. The violence of these processes should lead to very complete mixing on a short time scale. If necessary to complete condensation of the vaporized lithium at the center, a small "afterspray" could be directed at this area commencing at the end of the burn. An "afterspray" would also serve to protect the liner insertion mechanism and vessel head from the hot lithium "bubble," if it should form.

An analytic resolution of these processes would require computer codes not unlike computer codes used to model fission reactor melt-down accidents. In addition to understanding the complex interaction between heat-transfer, shock, and irreversible blast-mitigation processes, the actual heat deposited onto the blast vessel walls remains an issue that should be examined in more detail.

For the purpose of this study it is assumed that the dynamics of the lithium spray and the time of each liner shot can be correlated to an extent where all thermal energy releases are absorbed by a vessel inventory of 50 vol% lithium (74 m^3 or 18 tonne) spray coolant. This lithium, therefore, is heated 58 K and falls into a reservoir or sump (15, Fig. II-1) of lithium with a similar temperature (500 K). Lithium is circulated by a centrifugal pump (16, Fig. II-1) to an intermediate sodium/lithium heat exchanger (17, Fig. II-1), and eventually to a storage tank (18, Fig. II-1) prior to re-injection into the blast cavity. Approximately 1.75 tonne/s of lithium coolant flow would be required to remove the 4.3 GJ of thermal energy deposited once every 10 s. The dynamics of the energy transfer within the

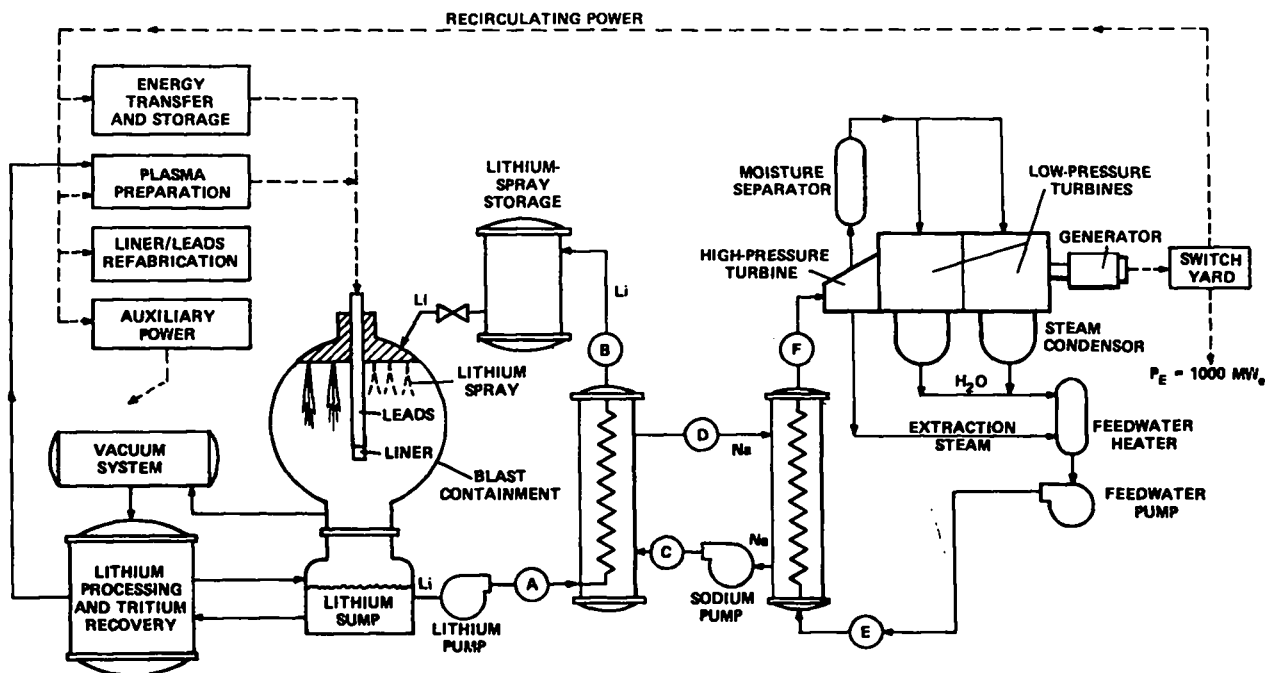


Fig. III-21. Schematic diagram of major coolant flows for the FLR system using the lithium-spray primary coolant. Table III-VI gives the stream conditions.

blast containment is assumed to be sufficiently rapid to preclude a significant thermal excursion at the walls of the blast containment. A schematic diagram of the FLR coolant and heat-extraction systems is shown in Fig. III-21, and Sec. III.D.1 gives a brief summary of key engineering parameters based thereon.

TABLE III-IV
SUMMARY OF STREAM CONDITIONS FOR FLR SYSTEM (FIG. III-21)

<u>Stream</u>	<u>Temperature (°C)</u>	<u>Flow Rate (kg/s)</u>	<u>Pressure (MPa)</u>	<u>Number of Blast Cavities</u>
A	500	1750	0.11	1
B	440	1750	0.0	1
C	288	4700	0.68	2
D	435	4700	0.68	2
E	219	930	6.8	4
F	286	930	6.8	4

C. Costing Model

Economic guidelines developed by Battelle Pacific Northwest Laboratories^{41,42} are used for the costing framework. The difficulties in comparing various cost models has led to the development of this common costing procedure and should provide the needed uniformity in assessing different concepts. The costing guidelines describe uniform accounting categories and procedures, although a uniform cost data base is yet to be adopted. A cost data base, therefore, has been generated by LASL to provide an interim optimization tool and to facilitate comparisons. It is emphasized that absolute cost values are intended only for the intercomparison of reactor designs and are not intended for absolute comparisons with existing energy technologies on the basis of present costs.⁴³ The cost accounting procedure, costing guidelines, and the cost data base are given in Appendix F. Figure III-22 gives a schematic diagram of the LASL interactive costing procedure which interfaces directly with the reactor design code.

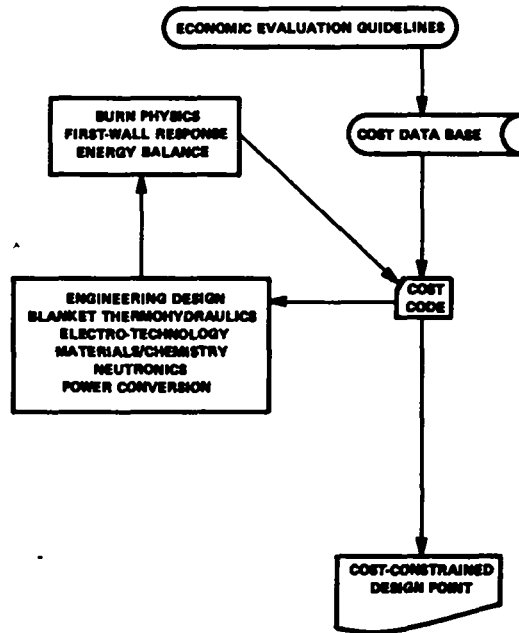


Fig. III-22. Schematic diagram of LASL Interactive Costing Program used to determine FLR power cost.

The total capital cost of the plant is composed of direct, indirect, and time-related (escalation and interest) costs. Direct costs are quoted in 1978 prices, result from the purchase of materials, equipment, and labor, and take into account allowances for spare parts and contingencies. Indirect costs, taken as a percentage of the direct costs, result from support activities necessary to complete the project and are divided into three major accounts: 15% for construction facilities, equipment, and services; 15% for engineering and construction management services; and 5% for taxes, insurance, staff training, and plant startup. Escalation and interest are computed as a percentage of the direct plus indirect costs assuming a 10-yr construction period. Aggregate percentages of 33.8% and 64.4%,⁴³ respectively, result in an escalation rate of 5% and interest rate of 10%. Having determined the total capital cost c_D (\$/kWe), the power cost c_p (mills/kWeh) is computed on the basis of a 15% return on capital investment, an added 2% of the total capital cost for operating expenses, and a plant factor of 0.85.

The FLR leads and liner replacement cost represents a unique operating cost for this concept that is not unlike a fuel cost. As noted in Sec. III.B.4 and Appendix C, if conductor recycle costs and insulator fabrication costs can be kept below 0.01 \$/kg and 0.10 \$/kg, respectively, the leads/liner cost should amount to no more than $\sim 20\%$ of the plant revenue for the low-yield design point summarized on Table II-I. The level of the liner/leads design is not adequate to permit the detailed costing of the associated refabrication plant, and the costing of the leads/liner assembly, therefore, is based on the assumed materials and handling cost using the optimized leads geometry described in Appendix C; specifically, the leads cost is treated as an increment to the plant operating cost.

D. Design Point

Sections III.B.1 through III.B.7 and the associated Appendix material summarized the scoping calculations that have been used to assess the major areas of technology and engineering anticipated for the FLR concept. These computations were guided primarily by the physics optimization and design point that emerged from the analyses discussed in Sec. III.A. As noted previously, the FLR concept portends a relatively simple high-power-density system, aside from the problems associated with a relatively rapid and large energy transfer and storage requirement. Because of the non-conventional physics and technological requirements identified for the FLR approach, much of the foregoing analysis had to be developed specifically for this study; the range of operating points projected to date has little basis in experiment. For these reasons the specific design point embodied in Table II-I and the extension of this design point into a more detailed estimate of engineering and cost parameters should be viewed as indicative; the engineering design point summarized in this section must be viewed as the best guess available at this time on the basis of the complex analytic task and absence of a relevant experimental base.

Central to the development of a reactor-embodiment for the FLR is the blast-confinement and primary heat exchange systems. A liquid-lithium spray was adopted and subjected to engineering evaluation in Secs. III.B.5-III.B.7. Other confinement/heat-transfer schemes have also been considered. Specifically, three FLR confinement schemes have evolved and are depicted in Fig. III-23. First, the liquid-metal LiPb/gas-bubble (He) concept was

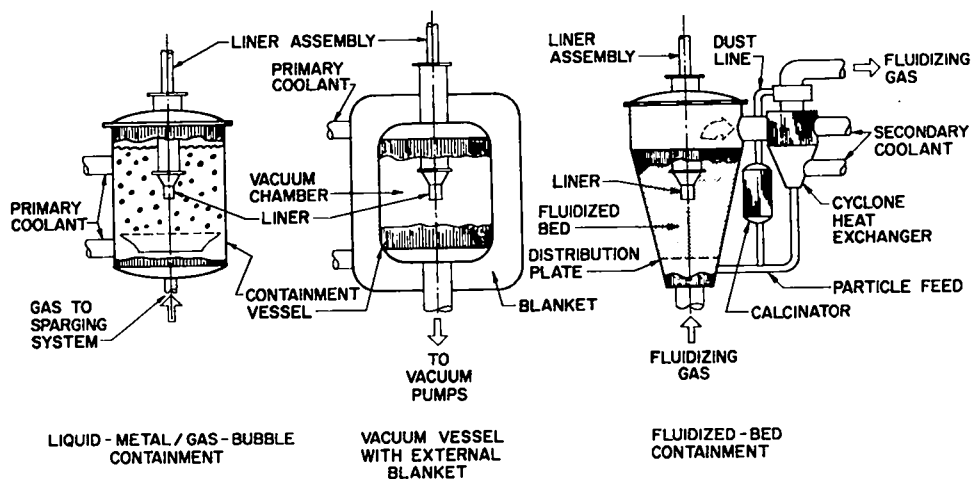


Fig. III-23. Schematic diagrams of several blast-containment and primary coolant schemes considered for the FLR.

developed, wherein a liner/leads assembly would be plunged into the two-phase coolant and detonated in much the same way proposed for certain laser/pellet fusion schemes.^{32,33} Unacceptably high pressure amplification at the container wall by shock reflection was computed (Ref. 9, Appendix E) when the He bubbles occupy a substantially smaller volume fraction than the liquid metal; therefore, liquid-metal schemes employing a small gas fraction were rejected. The favorable scaling of containment vessel size with blast energy, as predicted by the virial theorem,^{36,37} and the agreement that this theory gave with experimental data³⁵ led to the consideration of implosions detonated in vacuo; the vacuum chamber would be surrounded by a neutron-attenuating, tritium-breeding blanket. Although this concept has not been rejected, the potential problem of rapid insertion of liner assemblies, and the use of high voltage in vacuo, and the potential of damage to the vacuum wall by radiation and massive, energetic debris has resulted in consideration being given to a concept wherein the liner/leads assembly would be suspended in a fluidized bed of lithium-bearing particles¹⁰ (oxide or aluminate). Operating at 30%-50% of solid density, the bed would absorb nearly all

neutrons, the particles would be pulverized under the action of the post-implosion shock, would breed tritium, and with the carrier gas (He) would serve as the primary heat-exchange fluid. After the fluidized bed "recovers" from a given shot, the fine, pulverized particles (and thermal energy) would be removed from the system by the carrier gas, cooled, cyclone-separated from the carrier gas, resintered, and cycled back to the fluidized bed. The pulverizing action of the post-implosion shock would also release bred tritium from the bed particles, and the released tritium could easily be recovered from the He carrier gas by oxidation. Large sintered particles generated within the fluidized bed (typically at the container walls) as well as large pieces of liner debris attenuated by the fluidized particles, would fall out and be collected for reprocessing.

A fourth containment scheme, adopted by this study, would be similar to the liquid-metal/gas system noted above, but instead would inject the lithium (perhaps with lead) as a spray or "rain" into the liner cavity. This concept is similar to a scheme proposed by Burke^{12,44} for electron-beam fusion, and has been analyzed in Sec. III.B.6. Both the lithium-spray and the fluidized-bed schemes are considered as viable contenders for the tasks of blast confinement and primary heat transfer, although only the former is discussed here.

On the basis of the low-yield physics design point given in Table II-I and the scoping study of key engineering systems, the point design parameters given in Table III-V have been developed, following the guidelines given in Ref. 45. This engineering design point was evaluated using the costing model described in Sec. III.C. Table III-VI summarizes the capital cost according to a standardized costing account,⁴¹⁻⁴³ and Table III-VII summarizes the bottom-line unit operating and power costs. It is noted that the leads/liner costs have been estimated according to a separate optimization procedure described in Sec. III.B.4 and Appendix C. At the estimated 10.09 mills/kWeh (3.56 \$/shot) (based upon the melting leads option (Appendix C), 0.10 \$/kg for insulator costs, and 0.01 \$/kg for conductor costs) the leads/liner costs amount to 16% of the total power costs. If an upper limit of 30% is established for the percent of total power cost to be assigned to leads/liner expenditures, a maximum of 6.70 \$/shot is allowed.

TABLE III-V
SUMMARY OF KEY FLR DESIGN PARAMETERS FOR THE LOW-YIELD FLR
(TABLE II-I) VALUES GIVEN PERTAIN TO A SINGLE BLAST CAVITY
OF WHICH 8 ARE REQUIRED TO SUPPLY ~1000 MWe(net)

1. POWER OUTPUT	UNIT	VALUE
*1.1 Thermal Power to Power Cycle (Time Average)	MWt	425
*1.2 Direct Energy Conversion (Time Average)	MWe	0.0
*1.3 Plasma Chamber Power Density	MWt/m ³	4.8(a)
1.4 Plant Gross Electrical Output	MWe	170(b)
1.5 Plant Net Electrical Output	MWe	129(c)
2. REACTOR COOLANT SYSTEM		
*2.1 Blanket Coolant Type		Li(liquid)(d)
*2.2 Blanket Outlet Temperature (Hot Leg)	°C	500(d)
*2.3 Blanket Inlet Temperature (Cold Leg)	°C	442
*2.4 Blanket Outlet Pressure	MPa	0.11(e)
*2.5 Blanket Inlet Pressure	MPa	0.00(f)
*2.6 Blanket Coolant Flow Rate	kg/s	1750(d)
2.7 Blanket Coolant Pipe Material		Steel (2.25 Cr-1.0 Mo)
*2.8 First Wall Coolant Type		NA
*2.9 First Wall Outlet Temperature	°C	NA
*2.10 First Wall Inlet Temperature	°C	NA
*2.11 First Wall Outlet Pressure	MPa	NA(g)
*2.12 First Wall Inlet Pressure	MPa	NA
*2.13 First Wall Coolant Flow Rate	kg/s	NA
2.14 Total Number of Blanket Coolant Loops		1 (per two blast cavities)
2.15 Type of Blanket Coolant Circulator		centrifugal
2.16 Power Input to Each Circulator	MWe	1.6 (per two blast cavities)(h)
*2.17 Peak Blanket Temperature in Case of Loss of Coolant Flow	°C	(i)

*Information on items with asterisk to be supplied by LASL designers, whereas undesignated items represent first estimates to be refined by Bechtel Corporation.⁴⁵

TABLE III-V Cont'd.

	UNIT	VALUE
3. INTERMEDIATE COOLANT SYSTEM		(j)
3.1 Coolant Type		Na(liquid)
3.2 IHX Outlet Temperature (Hot Leg)	°C	435
3.3 IHX Inlet Temperature (Cold Leg)	°C	288
3.4 IHX Outlet Pressure	MPa	0.58
3.5 IHX Inlet Pressure	MPa	0.68
3.6 Coolant Flow Rate	kg/s	4.70(10) ³ (2 blast cavities)
3.7 Coolant Pipe Material		316 stainless steel
3.8 Total Number of Coolant Loops		4
3.9 Type of Coolant Circulator		centrifugal
3.10 Power Input to each Circulator	MWe	6.56 (2 blast cavities)
3.11 Number of IHX Per Loop		1 (4 blast cavities)
3.12 IHX Material-Shell/Tube		316 stainless steel
4. STEAM GENERATION SYSTEM UNIT		(j)
4.1 Steam Outlet Temperature	°C(°F)	286(546)
4.2 Steam Outlet Pressure	MPa(psia)	6.8(1000)
4.3 Steam Flow Rate	kg/s(lb/hr)	930(7.37(10) ⁶ , 4 blast cavities, 1 steam generator)
4.4 Feedwater Temperature	°C(°F)	219(425)
4.5 Number of Steam Generators per Loop		1(1700 MWt, 4 blast cavities)
4.6 Number of Modules per SG		NA
4.7 SG Materials, Shell/Tube		Steel
5. SHIELD COOLANT SYSTEM (blast vessel considered as primary "shield")		(k)
*5.1 Total Energy Deposited in the Shield	MWt	15.8
*5.2 Shield Coolant Type		Water
*5.3 Shield Outlet Temperature	°C	80
*5.4 Shield Inlet Temperature	°C	30
*5.5 Coolant Outlet Pressure	MPa	0.3

TABLE III-V Cont'd.

*5.6	Coolant Inlet Pressure	MPa	0.2
*5.7	Coolant Flow Rate	kg/s	75.6
6.	REACTOR AUXILIARY SYSTEMS	UNIT	VALUE
6.1	Vacuum Pumping System		(1)
	*Plasma Chamber Pressure	torr	1
	*Plasma Chamber Volume	m ³	70
	*Number of Pumps		4
	*Capacity of Each Pump	torr-liter/s	17.5(10) ³
6.2	Magnet Cooling System		
	*Cooling Load	Wt	NA
6.3	Plasma Heating System		
	*Cooling Load	Wt	NA
6.4	Tritium Processing and Recovery System		
	*Total Tritium Inventory	kg	18(m)
7.	REACTOR COMPONENTS		
7.1	Blanket/First Wall		
	*Material		Steel(2.25Cr-1.0 Mo)
	*Number of Modules		NA
	*Weight of Each Module	Tonnes	NA
	*Weight of Largest Single Component	Tonnes	200(n)
	*Dimensions of Largest Component	m x m x m	5.2-m(id)x0.3m(wall)
7.2	Shielding(concrete biological shield)		(o)
	*Material		Concrete/steel
	*Number of Modules		NA
	*Weight of Each Module	Tonnes	NA
	*Weight of Largest Single Component	Tonnes	NA
	*Dimensions of Largest Component	m x m x m	NA
7.3	Magnet		
	*Coil Forces Transmitted to Building	Newton	NA
7.4	Reactor Assembly		
	*Total Weight of Reactor Assembly	Tonnes	200(p)

TABLE III-V Cont'd.

	UNIT	VALUE
8. BUILDINGS		
8.1 Containment Building		(o,p)
*Minimum Wall Thickness for Shielding	m	1
*Internal Pressure, Normal/Accident	MPa	atm/atm
*Containment Atmosphere		Argon
8.2 Electrical Energy Storage Building		
*Wall Thickness for Shielding	m	0.0
*Internal Pressure, Normal/Accident	MPa	atm/atm
*Safety Related or Not	Yes/No	yes(q)
9. ELECTRICAL POWER REQUIREMENTS(for 8 units)		
*Cold Start Power from Grid	MWe vs	NA(r)
Auxiliary Power Requirement(Normal Operation)	MWe	
*Electrical Energy Storage		312(r)
*Magnet Power Supply (Other than energy storage)		NA
Blanket Circulators		6.4
First Wall Coolant Circulators		NA
Shield Coolant Circulators		1.0(s)
*Refrigeration System		nil (t)
*Vacuum System		0.2(u)
*Plasma Heating System		8.0(v)
*Miscellaneous Reactor Plant Auxiliaries		14.(w)
Feed Pump System		TBD (Bechtel Corp)
Condensing System		TBD (Bechtel Corp)
Heat Rejection System		TBD (Bechtel Corp)
Misc. BOP Auxiliaries		TBD (Bechtel Corp)
10. REACTOR MAINTENANCE		
10.1 Blanket/First Wall Replacement	Tonnes/yr	20(x)
10.2 Radioactive Material Storage Requirement; Years/Volume	Yr/m ³	UNK UNK
10.3 Description and Sketches of Replacement Concept		(Re:Sec.II,III.B)

TABLE III-V Cont'd.

11. REACTOR ASSEMBLY

*Detailed Dimensional Drawings of Reactor Assembly (Re:Sec.II,III.B)

- (a) Based on volume enclosed and included by blast-confinement vessel. Average power density within initial liner volume is 17.1 Gwt/m^3 .
- (b) Based on thermal conversion efficiency $\eta_{TH} = 0.40$.
- (c) Based on a computed recirculating power fraction $\epsilon = 0.25$ or a net plant efficiency of $\eta_p = \eta_{TH}(1-\epsilon) = 0.30$. In order to generate $\sim 1000 \text{ MWe}$ (net) 8 blast cavities would be required, each cavity being energized by the same ETS system.
- (d) Liquid-lithium spray injected at 40-50 vol% into blast cavity and around liner. For a 2.6-m-radius sphere and the energy released each shot, an average 58 K temperature rise would occur within the lithium spray. The flow rate is adjusted to give one vessel volume ($\sim 70 \text{ m}^3$) recycled each pulse period (10 s).
- (e) Based on a 20-m lithium head. This value actually represents the pressure differential across the lithium pump, the pressure at the spray-coolant inlet per se being zero.
- (f) The lithium spray serves as the blanket, which is injected into the blast cavity under vacuum.
- (g) First wall is considered here to be the blast cavity wall, and is both shielded and cooled by the primary lithium-spray coolant. For this reason items 2.8-2.13 are not applicable (NA).
- (h) Based on 55% efficient pump, 0.11-MPa head, and a $7\text{-m}^3/\text{s}$ average flow rate (half a cavity volume in 10 s).
- (i) The averaged surface energy density if the liner and fusion (alpha-particle) energy were completely unattenuated (i.e., spray blanket did not form) amounts to 13.4 MJ/m^2 . This energy is capable of raising 3.4 mm of the steel vessel to the melting point.
- (j) Both the sodium intermediate loop and the steam cycle for the FLR are scaled from the results reported by J. C. Scarborough ("Competitive Capital Costs for the Prototype Large Breeder Reactor," ANS Winter Meeting, San Francisco, CA, November 27-December 2, 1977, data reported in NUS Corp. publication). The GE/Bechtel Saturated Steam system was used. Each of four 726-MWt intermediate loops gave $T(\text{IN})/T(\text{OUT}) = 288^\circ \text{ C}/435^\circ \text{ C}$; 0.56 MPa pump head at $4.33 \text{ m}^3/\text{s}$ ($4.03(10)^3 \text{ kg/s}$) flow rate, head power = 2.43 MWe; pump power = 5.6 MWe; 1389 MWe s/kg . Two FLR cavities would provide 850 MWt, so the GE/Bechtel loops have been scaled by $850/726 = 1.17$. Four such units would provide 3400 MWt, which gives approximately the design goal of 1000 MWe(net). Two 1700 MWt steam generators are required, each driven by two such sodium loops, which are in turn driven by 4 blast cavities.

TABLE III-V Cont'd.

Footnotes Cont'd.

- (k) The shielding requirements for the FLR will not differ significantly from those envisaged for ex-pressure-vessel regions in LWR systems. For the case of 50 vol% lithium-spray coolant, less than 4% of the total fusion yield is deposited into the walls of the 2.6-m-radius, 0.3-m-thick wall of the containment vessel. For a pulse rate of 0.1 Hz, this amounts to 15.8-MWt or 0.62 MWt/m^3 of vessel volume. The thermal power density within a LWR pressure vessel is $\sim 5 \text{ MWt/m}^3$. The energy deposited into the vessel wall during the lithium-spray blowdown has not been resolved, but, similar to the walls of most internal combustion engines, this energy must be minimized for reasons of system efficiency and vessel lifetime; this "leakage" of fusion energy that is initially deposited into the lithium spray is assumed negligible ($\sim 1\text{-}2\%$ of fusion yield) compared to direct nuclear heating of the blast vessel. The 15.8-MWt low-grade energy deposited by direct nuclear heating into the vessel walls, when expressed on the basis of external surface area of the vessel, amounts to 0.15 MWt/m^2 , which is 10 times the energy naturally convected from a 32-mm-radius, 200-W incandescent light bulb. Although sufficient cooling area probably could be provided for natural- or slightly forced convection cooling of the vessel walls, forced cooling by low-temperature water has conservatively been adopted. The water coolant system is slightly pressurized in event of a shot which is not attenuated by the lithium-spray coolant to an extent predicted by the somewhat idealized neutronics model. Biological shielding located outside the blast vessel should operate with a very low power density, and probably would be cooled by natural convection or circulation occurring within the primary containment system. Since a shielding calculation, per se, has not been performed, the shielding requirement, in general, and the neutronic interaction between the biological shield and the blast vessel, in particular, remains unresolved.
- (l) Vacuum is required only to an extent needed to prevent the generation of gaseous shocks within the containment vessel. Only roughing pumps should be required, and the capacity is estimated on the basis of roughing from 10 to 1 torr in 10 s. The values quoted apply only to each blast vessel.
- (m) Based on 0.049 kg-T/MWt-y and 356 MWt of pure fusion power, to give 17.4 kg/yr tritium consumption, 158 kg/yr cycled (11% burnup), and a 1 month supply.
- (n) Weight of spherical blast containment vessel of 2.6-m inner radius and 0.3-m wall thickness. Although a detailed design of the blast vessel has not been made, the ~ 200 -tonne unit would have a ~ 50 -tonne demountable top head through which both lithium spray and liner/leads assemblies would be injected. The life of this vessel would be $\sim 10 \text{ yr}$, replacement would represent a major effort, but the vessel replacement should be considerably simpler than that for a LWR pressure vessel. Although design of the blast vessel for the plant lifetime ($\sim 30 \text{ yr}$) is

TABLE III-V Cont'd.

Footnotes Cont'd.

certainly possible, the weak design and engineering basis for this system at this time as well as the unique operating environment for this pressure vessel has led to the more conservative choice of a ~10-yr replacement and/or refitting period. In any case, the blast vessel is not considered a module.

- (o) Shielding would be provided by concrete (steel structural support for the blast vessel), not unlike that for the pressure vessel in a LWR system. Only a biological shielding (and a structural support) function would be performed by this system.
- (p) The containment building would include a ~2-m biological shield that encloses the blast vessel per se as well as the ~1-m-thick structural walls that enclose the liner/leads replacement room. These latter walls would have to be thick enough to provide biological shielding from post-shot radiation (from remnants of leads) as well as providing structural support for a ~100-tonne crane. Refer to Fig. III-24.
- (q) If oil/paper capacitors are used as transfer elements the ETS building would have to be provided with an extensive fire-prevention system (e.g., Halon). Aside from the umbilical power feedthrough, the ETS room would not be a part of the containment room.
- (r) Each of the 8 FLR units requires 390 MJ every 10 s; this energy would be delivered from a common homopolar M/G and transfer capacitor unit, the homopolar transferring its energy to a storage inductor in ~0.1 s and the inductor rapidly (~20 μ s) transferring its energy via a transfer capacitor directly to the imploding liner. In a sense, therefore, each liner shot could be viewed as a "cold start" requiring power from the grid, at a level of 390 MJ x 8 units/10 s = 312 MWe. This power, however, would be supplied continually and in proportion to the total plant output. Although a given unit could not accept its ~39-MWe share of this recirculating power during the ~0.1-s period when energy is being transferred from the homopolar M/G set to the storage inductor, appropriate circuitry and switching can be designed that would prevent this short interruption, occurring for ~0.1 s every 10/8 = 1.25 s, from being "seen" by the 312-MWe recirculating power supply. A detailed circuit design of this internal power-handling system has not been made. Generally, the 312 MWe would be switched to a unit that is in a passive or stand-by state when the unit under question is being switched into the liner; otherwise, an electrical ballast or "surge-tank" would have to be used.
- (s) Based on an 8-kWe power requirement to remove and reject 1 MWt of low-grade (~80°C) energy by water cooling.
- (t) The superconducting stator windings on the homopolar M/G sets will require 0.2% for every GJ of stored and switched energy. This loss is embedded in the 95% transfer efficiency assumed for the ETS system.

TABLE III-V Cont'd.
Footnotes Cont'd.

- (u) Based on 100 kWe per 25 000 L/s for Roots blowers.
- (v) The 7.5 MJ required to prepare the plasma prior to a given liner implosion is assumed to be supplied in ~ 10 s with a 75% efficiency. The 1-MWe/unit requirement would be supplied by a continuous 8-MWe supply, subject to an as yet unspecified ballast constraint similar to that described in footnote (r).
- (w) The miscellaneous plant auxiliaries have not been specified, but would include the power requirements of the liner/leads debris-recovery and recycle system. This requirement is taken as 1% of the gross electrical output.
- (x) Based on replacing 200-tonne blast vessel every 10 yr.

TABLE III-VI

ESTIMATED CAPITAL COSTS FOR THE FLR DESIGN
POINT GIVEN IN TABLE III-IV

<u>Account Number</u>	<u>Account Title</u>	<u>Million Dollars</u>
20.	Land and Land Rights	2.500
21.	Structures and Site Facilities	167.987
22.	Reactor Plant Equipment	488.710
23.	Turbine Plant Equipment	156.999
24.	Electric Plant Equipment	85.231
25.	Miscellaneous Plant Equipment	15.364
26.	Special Materials	28.060
90.	Total Reactor Direct Capital Cost	944.850
91.1.	Temporary Facilities	
91.2.	Construction Equipment	
91.3.	Construction Services	
91.	Construction Facilities, Equipment, and Services (15%)	141.728
92.	Engineering and Construction Management Services (15%)	141.728
93.1.	Taxes and Insurance	
93.2.	Staff Training and Plant Startup	
93.3.	Owner's G&A	
93.	Other Costs (5%)	47.243
94.	Interest During 10 Yr Construction (8%/yr=49.4%)	821.453
95.	Escalation During 10 Yr Construction (5%/yr=33.8%)	431.135
99.	Total Reactor Capital Cost	2528.136

TABLE III-VII

SUMMARY OF CAPITAL AND OPERATING COSTS FOR THE
FLR DESIGN POINT GIVEN IN TABLE III-IV

Thermal Power (Mwt)	=	3400.00
Gross Electric Power (MWe)	=	1360.00
Net Electric Power (MWe)	=	1016.00
1/Recirculating Power Fraction	=	3.95
Plant Factor	=	.85
Direct Investment Cost (\$/kWe)	=	929.97
Total Investment Cost (\$/kWe)	=	2488.32
Capital Return 15% (Mills/kWeh)	=	50.33
Operating 2% (Mills/kWeh)	=	6.71
Operating For Leads and Liner(Mills/kWeh)	=	10.09(a)
Power Cost (Mills/kWeh)	=	57.04

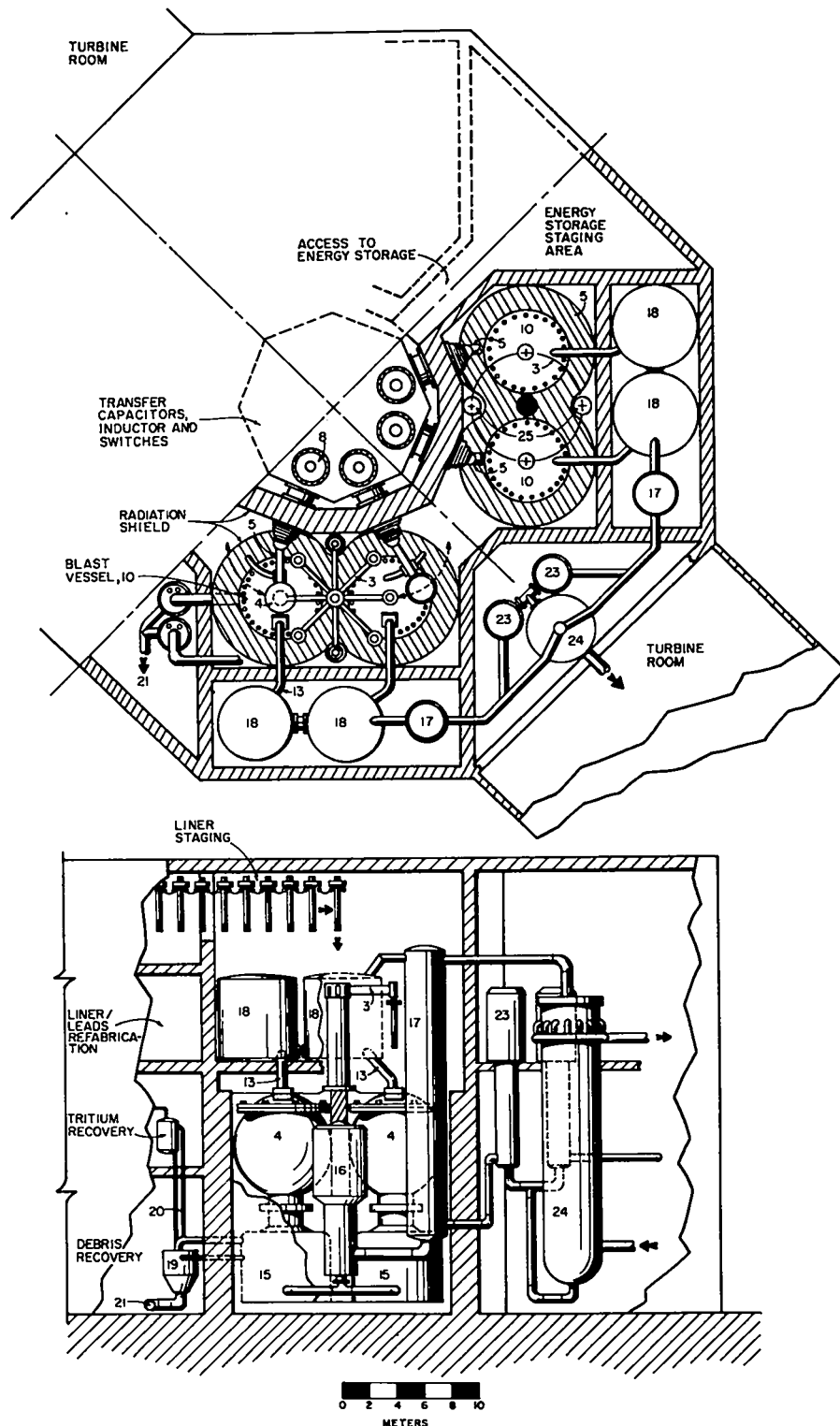
(a) The leads and liner replacement costs have been evaluated separately (Appendix C) using 0.10 \$/kg for insulator costs and 0.01 \$/kg for conductor recycle cost. The leads configuration that separately minimizes investment costs according to the separate algorithm is described in Appendix C (0.2-m radius, 0.01-m thickness, 2.0-m length, 0.7 conductor volume fraction). At these unit costs for insulator and conductor, the leads/liner cost would amount to 3.56 \$/shot.

Following the guidelines established for the intercomparison of alternative fusion concepts,⁴⁵ the net electrical output from the FLR must be in the 1000-MWe range. To accomplish this goal, the low-yield design point requires 8 units of the type depicted in Fig. II-1. Both the values given in Table III-V and the engineering cost estimate is based on an eight-unit, ~1000-MWe(net) system. A definite cost advantage arises by this modular approach, in that the expensive ETS system can now be shared by 8 FLR units of ~130-MWe(net) size each; hence, for a 10-s pulse time per unit the ETS unit must discharge every 1.25 s. The functioning of each unit follows the description given in Sec. II and Fig. II-1, and Fig. III-24 gives a schematic plan/elevation drawing of the total ~1000-MWe(net) system. Two cavities drive a single Li/Na intermediate heat exchanger [17], two Na/H₂O heat exchangers are used, and two steam generators are envisaged. The footnotes associated with Table III-V give the rationale for the engineering parameters summarized thereon.

Because of the scoping nature of this design study many of the items on Table III-V are not based upon detailed computations. Furthermore, this design point has been selected on the basis of a physics optimization that has been tempered by intuitive but realistic technological judgments. Ultimately, more detailed studies should project a design point that is optimized on the basis of a self-consistent and iterative physics, engineering, and costing model. Whether the results from such an analysis differ significantly from those given in Table III-V remains to be seen.

IV. PRESENT KNOWLEDGE IN PHYSICS AND TECHNOLOGY

The primary intent of the FLR study is to quantify the optimum physics operating point, as embodied in Table II-I. Although a complete and self-consistent engineering design is beyond the scope of both this study and present theoretical and experimental knowledge, crucial technological issues were identified and when possible analyzed quantitatively. Engineering computations were performed to an extent necessary to carry out a preliminary estimate of cost as well as to assess required technological development. This section concludes the FLR study by means of an assessment of present knowledge in both physics and technology.



PLAN AND ELEVATION-CONCEPTUAL 8-UNIT FAST-LINER REACTOR (3400 MWt)

Fig. III-24. Plant layout for a nominally 1000-MWe(net) FLR using 8 blast-confinement cavities. Two cavities drive a separate Na/Li heat-transport system, and two such systems drive a single Na/H₂O steam generator (4 cavities per steam generator, or two steam generators) component identification numbers are defined in Fig. II-I. Additionally: 23, Na pump; 24, steam generator.

A. Physics Confidence

Since fast-liner experiments are just beginning⁵ and, relative to the projected FLR requirements, are at a very elementary level, predictions of reactor-grade plasma conditions are necessarily speculative. Naturally, more data are available on liner behavior than on plasma properties for the conditions envisaged for the FLR.

1. Plasma Preparation. As discussed in Sec. III.B.2, gun plasmas have been produced at densities of $2(10)^{23} \text{ m}^{-3}$ with directed energies of $\sim 0.2 \text{ keV}$. A fivefold increase in density and a doubling of energy would reach the necessary plasma conditions for an FLR, assuming an embedded B_θ of $\sim 13 \text{ T}$ can also be achieved. It seems probable that this initial condition can be reached with sufficient effort. It is not clear that the apparatus required can be economically made energy efficient and located sufficiently far from the liner to avoid damage from radiation and shock waves.

2. Transport. Plasma transport computations made to date have indicated that an FLR as envisaged here would work. This perspective could be changed radically, however, by several factors. Perhaps the most serious problem would be plasma turbulence that could sweep high-density material from the liner into the plasma and beyond the sheath of insulating magnetic field; line radiation would then quickly cool the plasma interior below acceptable levels. Lindemuth and Jarboe⁴⁶ computationally observed enhanced thermal conduction to the liner (40%) by small vortices generated near the liner wall. This computational model did not include a mechanism for losses by high-Z line radiation, however.

Another inadequacy of the current plasma model is embodied in the assumption of perfect electrical conductivity within the liner. Prediction of electrical properties of a metal under the extreme temperatures and pressures encountered by the liner is difficult. Best estimates are incorporated into the hydrodynamic code CHAMISA¹⁷ and should give improved estimates in the near future. More important, however, the ongoing series of LASL experiments should shed considerable light on this uncertainty.

Although confidence in general trends and scaling of plasma properties is high (Sec. III.A.4) the physical completeness of these models must be considered moderate to poor. If, for example, transport losses are more severe than anticipated by the present model, present knowledge can help alleviate the problem to the extent limited by economic and technological

(plasma preparation, faster implosions) considerations. If, on the other hand both the conditions assumed for plasma preparation and liner drive prove to be too optimistic, while simultaneously turbulence becomes a major energy loss mechanism, the entire FLR concept may not prove feasible.

3. Liner. The liner itself is probably the best understood component central to the FLR physics. As noted above, liner implosions have been demonstrated experimentally,^{6,7} and a major fast-liner project is under way at LASL.¹⁹ A variety of analytic liner models^{17,24} have shown good agreement in predicting liner dynamics. Perhaps the most serious problems are the attainment of high velocities (10^4 m/s) and the generation and retention of the internal insulating field, B_{θ} . These questions should be largely answered by the LASL experimental program.¹⁹

B. Technology

If the FLR were to function within the physics predictions given in Sec. III.A and assessed in Sec. IV.A, the feasibility of the reactor system as analyzed in Sec. III.B appears technologically or economically difficult. Although the means by which the plasma is prepared, the liner/leads assembly is manipulated, and the blast is contained can be conceptualized, no credibly detailed mechanism by which to perform the crucial operations could be invented within the limits of this study. Superposing realistic economic constraints upon the physics uncertainties renders many of these technological problems/uncertainties even more difficult. Each of these issues is discussed below in decreasing order of perceived importance.

1. Liner/Leads Fabrication. The economic implications of maintaining the cost of leads and liner below ~ 0.04 \$/kg (6.70 \$/shot) if the associated operating cost is to be held below 30% of the total power cost represents a crucial uncertainty for the FLR. Table IV-I summarizes 1977-78 unit costs for both fabricated items and basic materials. Clearly, the required leads/liner unit costs (70% conductor at 0.01 \$/kg, 30% insulator at 0.10 \$/kg) are far below those presently achieved by today's manufacturing industry, with possible exception of the packaging industries. On the basis of unit costs for most metals, it is concluded that the destroyed conductor must be recovered and recycled; the cost of (glass) insulator must approach that of a soft-drink container, the latter cost representing essentially an energy cost associated with the heat of fusion. Although a considerable design effort

must be expended on the basis of more experimental data to resolve this leads/liner cost issue, this economic constraint presently appears very serious.

TABLE IV-I
TYPICAL UNIT COSTS FOR FABRICATED ITEMS AND BASIC MATERIALS

<u>Fabricated Items</u>	<u>Unit Cost (\$/kg)</u>
Commercial jet aircraft	115-133
Nuclear aircraft carrier	55-62
Copier	52-60
Bicycles	31-60
SS or Al piping "tee"	22-40
LWR pressure vessel	11-35
Alternator	16-24
Diesel generator	8.0-8.9
Passenger bus	7.1-8.2
Electric motor	4.4-9.3
Automobile	3.6-5.3
Hamburger	2.2-2.9
Soft drink bottles	0.02-0.04
Basic Materials	
Aluminum	Plate 4.19
	Secondary ingot 1.21
Copper	Plate 2.31
	Wire blank 1.43
Steel	Boiler plate 0.35
	Cold roll 0.31
Lead	Ingot 0.57
	Brick 0.88
Lithium	Commercial (low sodium) 27.49
Lithium	Chemical (99.88%) 259.03
Pyrex	Large-bore tube 2.86
Alumina	Powder 2.20
	Medium-bore tube 32.10
Mulite	Medium-bore tube 22.00

2. Plasma Preparation. The means by which a 0.5-keV, $1.25(10)^{24} \text{ m}^{-3}$ plasma with a total energy of 7.5 MJ is to be efficiently injected into or created within the 2.5-litre liner from a distance of 3-5 m is presently unproven, although a number of schemes have been addressed in Sec. III-B.2. This problem is further complicated by the need to create simultaneously a $\sim 13\text{-T}$, azimuthal insulating field, which corresponds to a uniform current density of 120 MA/m^2 through the injected plasma. Although laser-heated plasmas have been produced that approach these temperatures and densities,²⁸ the required total energy, embedded insulating field, repetitive and remote production, and timing with a simultaneous liner implosion have not been demonstrated. Although an experimental basis that supports the specific needs of the FLR does not exist, the LASL experimental program will address this issue in the next few years.⁵

3. Containment. The data base for the containment of explosive releases in spherical vessels has been reviewed in Appendix E (Fig. E-1). If the scaling projected by these relatively low yield experiments and predicted (for the vacuum case) by the virial theorem (Sec. III.B.6 and Appendix E) applies to the 1.5-GJ releases anticipated for the FLR, to first order, no insurmountable problem for blast confinement is anticipated. In addition to a significant extrapolation of the existing data base, the issues of shock formation in blast-mitigating media, asymmetric blasts and projectile formation, propagation of damage by shocks to "safe" regions of the system (pumps, storage vessels, leads connectors, plasma preparation, etc.), fatigue failure at penetrations and weldments, and focused shocks represent important issues for the containment system. The lithium-spray coolant/blast-mitigator is not an effective radiation shield for the volume fractions, vessel sizes, and chemical compositions selected (Sec. III.B.5); the structural first wall will experience an appreciable, low-energy neutron flux, although this problem is amenable to a number of design solutions. Furthermore, the actual shape and form of the first wall, insofar as the mitigation and/or time-extension of shocks via bow-wave phenomena are concerned, must be resolved by more detailed computation and experiment.

The coupling of the blast-confinement, neutronics (energy deposition, tritium breeding, shielding), and heat-transfer functions of the containment-vessel/lithium-spray system is very strong. Self-consistent calculations that simultaneously couple all these elements together have not been made, nor are

they likely to be made in the near future. Furthermore, the liner physics and blast containment are not independent; if for reasons of turbulence or limits on plasma preparation the liner energy W_L and associated thermonuclear release must be increased to achieve the required liner and/or engineering Q-value, the blast-containment problem will become more difficult.

4. Energy Transfer and Storage. The low-yield design point (Table II-I) requires the transfer of ~ 450 MJ of energy in 20-30 μ s with an external transfer efficiency of 0.95; for a voltage of ~ 200 kV, the required currents lie in the range 250-500 MA. The energy transfer is "one-way," and no reversible recovery is required. Table IV-II summarizes characteristics of potential energy storage systems that may be used. The selection of a slowly discharging homopolar motor generator coupled to an inductive store has been selected on the basis of a potential cost advantage, although the use of high-energy-density electrolytic capacitors may offer additional advantages, since the homopolar/inductor scheme still requires an appreciable fast-transfer capacitor bank. The switching and transfer of the required currents at the voltages needed and the desired risetimes will require significant development, considering the 10-to 20-s pulse rate, energy-focusing, and time-sequencing requirements. Because of the anticipated expense associated with the energy transfer and storage system, a single unit will have to service a number of liner cavity systems at the ~ 10 -to 20-s repetition rate. For each cavity approximately 40 MWe will be required to charge the storage system during the ~ 10 -s period between pulses, and the associated internal power-handling requirements have yet to be addressed.

5. Leads/Liner Replacement. As noted in Sec. IV.B.1, the details of the leads/liner fabrication remain unresolved. Likewise, the means by which a ~ 0.5 -tonne leads/liner assembly is inserted into the blast containment, attached to the driving energy source, fitted with a plasma preparation unit, and subsequently removed has not been resolved. This sequence of operation must occur once every 10-20 s. For an 85% plant factor, each 430-MWt cavity must cycle $2.5(10)^6$ liner/leads assembly each year or 7300 units/d. If a total plant inventory is to remain below ~ 100 liner units (per cavity), the liner/leads fabrication time must be less than 20 minutes. Given that each assembly weighs ~ 0.5 tonne, the total liner throughput amounts to 50 kg/s or $1.3(10)^6$ tonne/yr (Li coolant flow is 1750 kg/s).

6. Primary Heat-Transfer System. The lithium-spray primary coolant system described in Sec. III.B.7, although non-conventional and untried, appears to present no intrinsic difficulties. The coupling of the transient establishment of the spray, the equilibration of the exponential energy density left in the two-phase coolant immediately after the implosion, and the influence of shocks and/or blast-mitigating processes creates some unresolved issues for this untried technology. Given that these problems can be successfully resolved within the containment vessel, no unusual difficulties are envisaged in removing the 50-60 K sensible heat delivered to the continuously flowing lithium coolant. Furthermore, temperature transients at the Li/Na heat exchanger can be virtually eliminated at the expense of an increased lithium inventory (within the sump). Given that the total lithium inventory equals ~ 10 times that required in the blast vessel for a single shot, the lithium inventory would amount to 0.47 tonne/MWt. It should be noted, however, that both lithium (centrifugal) pumps and Li/Na heat exchangers are not commercially available items.

TABLE IV-II
SUMMARY OF POTENTIAL ENERGY STORAGE SYSTEMS

Type of Store	GENERAL FEATURES OF PULSED-POWER SUPPLIES			Largest Installation Existing or Expected (MJ)
	Energy Density (MJ/m ³)	Transfer Time (ms)	Cost (\$/J)	
Capacitive	0.01 - 0.10 ^(a)	10 ⁻⁶	0.10 - 0.25	10
Inductive	10	0.1 - 10.	0.01 - 0.10	10 ²
Fast Inertial (HETS)	100 ^(b)	1 - 100	0.01 - 0.10	10 ³
Slow Inertial (HETS)	100	10 ³ - 10 ⁴	0.001 - 0.01	10 ⁴
Very Slow Inertial (Alternator, SCR-PS)	100	10 ³ - 10 ⁴	0.01 - 0.10	10 ⁴

(a) 0.003 MJ/m³ of bank energy.

(b) 1000 MJ/m³ has been achieved.

V. SUMMARY CONCLUSIONS

This FLR study has not been a multi-man-year effort, and consequently a detailed, self-consistent design has not emerged. Furthermore, on the basis of present knowledge in both physics and technology, it is doubtful whether such a design could be generated at any level of effort at this time; the physics and engineering data base required to be applied to the many unique areas in the FLR concept simply does not exist. Nevertheless, the following conclusions seem apparent.

- Based upon the realistic physics models used to estimate the breakeven and reactor-like conditions for FLR, achievement of these conditions in the laboratory appears promising. Although the effects of thermal loss enhanced by microturbulence have not been modeled, and represent a major physics hurdle, this issue does not appear crucial to the physics success of the FLR concept at this time.
- All physics optimizations are based on a liner with the physical properties of copper, whereas preliminary cost estimates indicate that a once-through usage of copper would be economically unacceptable. Either a means must be found to recover low percentages of copper from the liquid-metal coolant or liner materials and/or configurations with properties similar to copper liners must be found.
- The feasibility and cost of the blast confinement presents no serious barrier. Although this conclusion is based upon results from approximate analytic models, sufficient design flexibility and innovation are available to solve unforeseen blast confinement problems within realistic constraints of cost and technical feasibility.
- Both the design and cost of the FLR leads/liner structure present major problems. Although the bounds and constraints of this problem have been quantified, it is not clear that the present or readily extrapolatable technologies can deal with this problem.
- Both the physics and technology required to prepare the plasma for fast-liner compression are not within reach of present or near-term knowledge. Although four possible methods were suggested, the relevant physics data base is poor, and significant experimentation is required. Since these plasma preparation requirements are specified on the basis of optimal FLR physics, these requirements can be relaxed only by degrading the reactor ergonic performance (within the limits of the models used).

- The energy transfer and storage (ETS) requirements, including transfer efficiencies, are beyond the state of the art. Although no technological limit could be identified that would not allow the ETS goals to be achieved, the costs incurred in achieving these goals may be prohibitive.
- Although the primary heat-exchange system is non-conventional, no intrinsic cost or technological barrier to achieving Li(or LiPb) spray cooling was identified. Insofar as the shielding function of the lithium spray is concerned, the point design presented was not optimal. Questions of repetition rate, thermal load on the structural wall, projectile formation and attenuation, and coupled heat-transfer/shock processes have not been fully resolved, however.

The FLR promises a relatively small (high-power density) and economical power system. If the fast-liner approach can be made to work, breakeven and reactor-like conditions can be demonstrated at a relatively early date with modest expenditures of research dollars. Although the FLR promises reactor-like plasma performance at an early date, the development of the advanced technologies cited above may extend considerably the time to commercial power.

In concluding this study it is emphasized that a rather specific liner/leads configurations has been adopted. The problems and/or uncertainties identified with plasma preparation, materials destruction/recycling, and plasma turbulence, therefore, may indeed be significant to magnetically driven cylindrical liners. Improvement in the reactor embodiment may result with an approach wherein the liner components are electrically accelerated outside the blast radius and subsequently brought together without significant materials destruction. Furthermore, a plasma/liner model that is more complete and/or that has been "calibrated" with relevant experimental results could conceivably lead to enhanced yields. Generally, the rapid adiabatic compression of a wall-confined plasma appears to provide acceptable energy releases without the problems inherent in pure magnetic confinement and the basic concept deserves serious attention and refinement.

ACKNOWLEDGMENTS

We express our appreciation to the LASL personnel who have assisted this study: R. Bartholemew (structural mechanics), D. J. Dudziak (neutronics), G. Gryczkowski (numerical techniques), R. C. Malone (physics), J. Marshall (physics, blast confinement), T. A. Oliphant (numerical techniques), A. R. Sherwood (physics), and C. E. Swannack (energy storage and transfer).

APPENDIX A
DESCRIPTION OF LNRBRN CODE

A flow chart for the LNRBRN code system is shown in Fig. A-1. In addition to data input, printout, and plotting, the main program controls subroutines that perform timewise integration of the transport equations, readjust the Lagrangian mesh for pressure balance, manipulate the liner, and set the time step.

All time-dependent variables are stored in arrays with the subscript $K = 1, 2, 3$ corresponding to the times t_{j-1} , t_j , and t_{j+1} , respectively. In the code the corresponding nomenclature is $JJ - 1 = JM = j$. All functions are known in the JJ loop for $K = 1$ and 2 ; $DT = \Delta t = t_j - t_{j-1}$ is initially assumed as $t_{j+1} - t_j$. For the first step in the JJ loop cycle, subroutine PROJKT linearly projects new variables to the time t_{j+1} , $K = 3$, using data from the preceding two time steps. Included in PROJKT are the coefficients of the transport equations. Subroutine LDRIVE uses known variables at time t_j and projected or iterated variables at t_{j+1} to compute liner deceleration, velocity, position, and compression at time t_{j+1} , $K = 3$. Subroutine STEP implicitly solves the transport equations on a rigid mesh and subsequently calls subroutine ZPB to readjust the mesh and re-establish pressure balance. The newly obtained variables at t_{j+1} , $K = 3$, are used in subroutine COEF to recompute all physical variables and transport coefficients at t_{j+1} . The ITA loop returns to pass through subroutine STEP two more times to improve iteratively the computed data at time t_{j+1} .

The time step is controlled in the ITB loop. Subroutine TIMTST computes the maximum fractional change of the plasma temperature and field variables (T and B) between t_j and t_{j+1} . If this change, f_c , satisfies $4\% \leq f < 10\%$, Δt is not changed. If $f_c \leq 4\%$, Δt is increased by a factor of 2 in the next cycle of the JJ loop. When $f_c > 10\%$, Δt is immediately reduced by 2, and control is returned to the start of the JJ loop. If Δt is reduced 10 times in a JJ cycle, an error message is printed.

Subroutine ENBAL computes all energy-related functions: total plasma and field energy, liner kinetic and compressional energy, and mechanical work done by the liner on the plasma and field. Two energy checks are given for each data printout. One check compares work done by the liner on the plasma to kinetic and compressional energy changes of the liner. The other energy check

PROGRAM LNRBRN

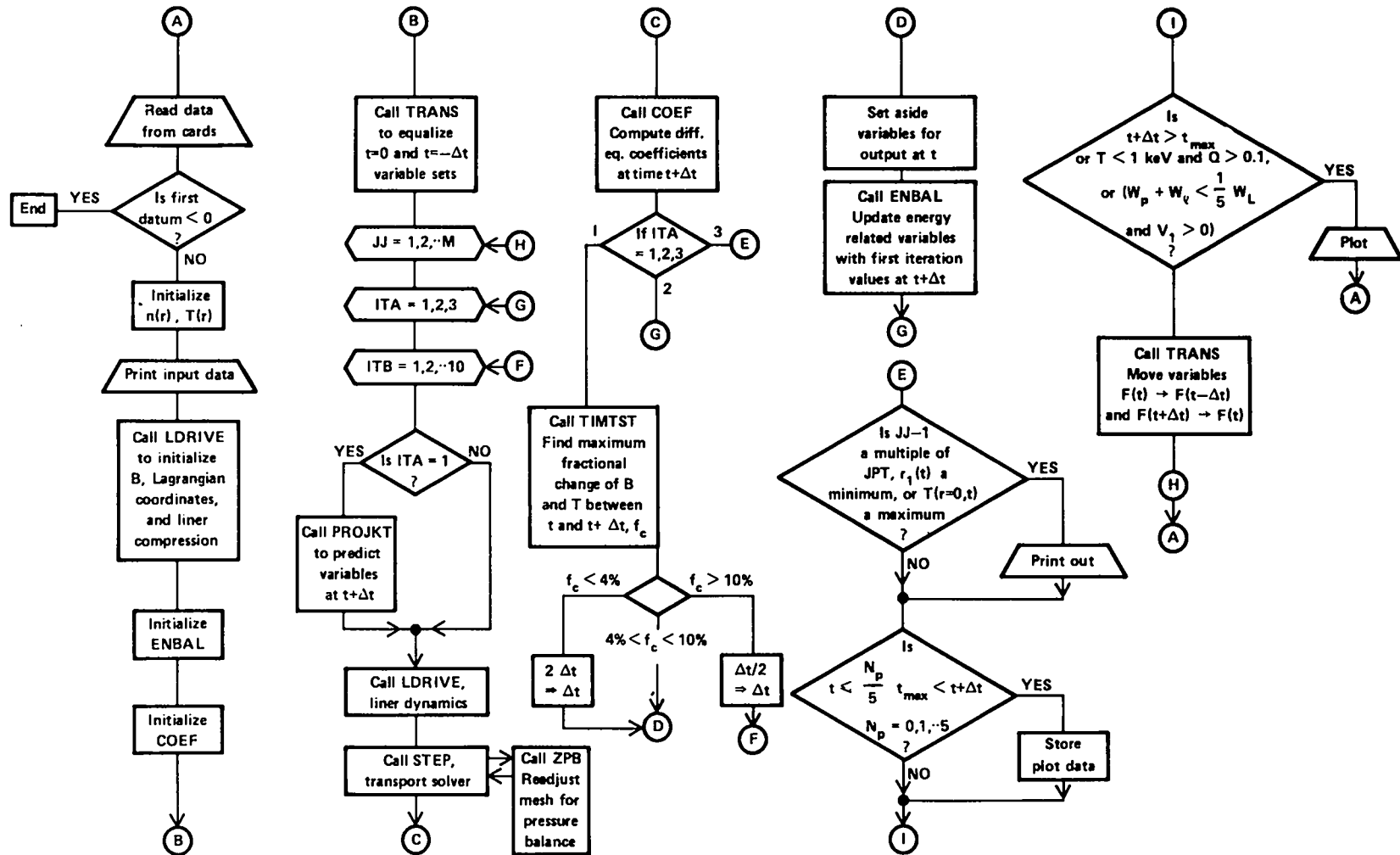


Fig. A-1. Logic flow diagram for LNRBRN: a radial, time-dependent magnetohydrostatic burn code using an analytic model for the liner compressibility.

compares plasma and field energy to work done on the plasma-field system. A third numerical check is made by accounting for particles in the system as compared to the initial total minus D-T burnup.

In addition to a complete, time-dependent description of the liner and plasma parameters, the final result given by LNRBRN is presented in terms of the scientific or liner Q-value $Q = (W_N + W_\alpha)/W_L$, where W_N and W_α are the fusion-neutron and alpha-particle energies, respectively.* The liner Q-value is the object function used in all physics optimizations.

*In this study W_L is the initial kinetic energy of an undriven liner, W_L . When the liner-ETS coupling is considered, W_L is the electrical energy transferred from the current leads to the liner assembly. Typically W_{KRO} is $0.9 W_L$. This effect is not considered here, leading to somewhat optimistic Q-values.

APPENDIX B
OPTIMIZATION OF COAXIAL LEADS STRUCTURE

As discussed in Sec. III.B.6, a "blast radius" can be identified for the FLR inside which no apparatus is expected to survive the shock wave generated by the liner implosion. The electrical power needed to drive the liner must be transmitted from a permanent fixture outside this blast radius through destructible power leads and to the liner. In this section the cost optimization of a destructible coaxial transmission line is described. The results of this analysis of simple, coaxial leads point out a definite problem associated with the leads mass and have led to the adoption of the "force-reduced" interleaved structure described in Sec. III.B.4 and Appendix C.

A generalized coaxial leads structure for a FLR is illustrated in Fig. B-1 and Table B-I. Three unit costs are considered: insulator c_I (\$/kg), conductor c_C (\$/kg), and energy c_e (\$/J). The insulator and conductor costs apply to the manufacture of new components using debris from previous liner shots as well as any make-up materials required. Energy costs apply to all energy entering the destructible transmission line that does not reach the liner assembly. Energy is dissipated in the leads by three mechanisms: (a) joule heating of the conductor, (b) kinetic energy imparted to the conductor by high magnetic fields, and (c) inductive energy remaining in the leads at the time of fusion energy release (unrecoverable energy). For all cases the energy dissipated in or parasitically absorbed by the destructible leads is assumed recovered in the thermal cycle; a portion ($\eta_{TH} = 0.4$) of this energy, therefore, re-appears as electrical power. The leads energy cost, therefore, would be approximated by

$$c_e (\$/J) = (1 - \eta_{TH})c_p + \eta_{TH} c_{ETS} \quad , \quad (B-1)$$

where c_p (\$/J) is the cost of power and c_{ETS} (\$/J) is the amortized, "per-shot" cost of the energy transfer and storage system plus associated power conditioning equipment. Non-recoverable dissipation in the liner and surrounding return conductor, as well as external losses, are assumed here to be negligible. The following simplifying assumptions are made in order to carry out the coaxial leads optimization: (a) the insulator thickness Δ_I is assumed to be the same everywhere even though the voltage would be slightly lower near the liner because of energy deposition along the leads; (b) tensile

strength of the conductor is assumed negligible; c) the lead structure is assumed to be thin compared to the radius; and d) the conductor is thicker than an electrical skin depth, $\Delta_c \Delta$.

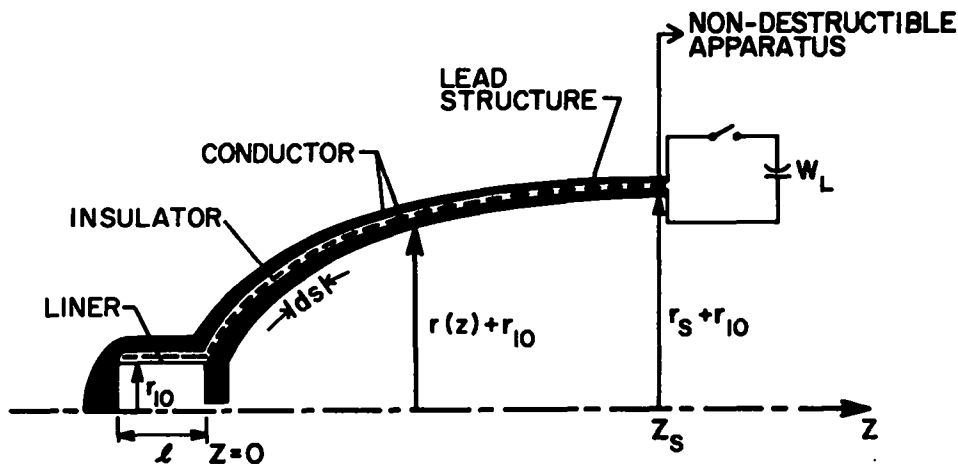


Fig. B-1. Generalized shape $r(z)$ of a coaxial leads structure used to optimize the leads structure on the basis of cost.

TABLE B-I

SUMMARY OF VARIABLES AND DEFINITIONS USED TO ARRIVE AT OPTIMUM COAXIAL LEADS CONFIGURATIONS

<u>Symbol</u>	<u>Definition</u>
$r(z)$	Lead radius at axial position z measured from liner
Δ_B	"Energy effective" conductor separation (Eq. (B-8))
$\Delta_C(z)$	Actual conductor thickness as a function of axial thickness
Δ_C^*	Optimum conductor thickness (Eq. (B-17))
Δ_I	Insulator thickness
Δ	Electrical skin depth in conductor = $(2\eta/\mu_0\omega)^{1/2}$
ΔM	Movement of conductor during a pulse (Eq. (B-13))
r_{i0}	Initial liner radius
$I_d(t)$	Liner drive current, $I_{\max} \sin(\pi t/t_f)$
I_{\max}	Maximum liner current
$I(t_f)$	Liner current at peak compression, $< I_{\max}$
$V(t)$	Voltage applied to liner assembly
t_f	Time of peak compression, π/ω
W_L	Electrical energy transferred to liner assembly

Table B-I cont'd.

<u>Symbol</u>	<u>Definition</u>
$V(t)$	Voltage applied to liner assembly
t_f	Time of peak compression, π/ω
W_L	Electrical energy transferred to liner assembly
W_C	Kinetic energy imparted to leads conductor (Eq. (B-12))
W_{OHM}	Joule heating in leads conductor (Eq. (B-14))
$v_C(z)$	Leads conductor velocity after pulse
ρ_C	Conductor density
ρ_I	Insulator density
η	Resistivity of conductor
$\bar{\eta}$	Time-averaged resistivity
C_I	Unit cost of insulator
C_C	Unit cost of conductor
C_e	Unit cost of energy
C_I	Total cost of insulator in leads
C_C	Total cost of conductor in leads
C_F	Cost of stored field energy in leads
C_M	Cost of energy associated with leads motion
C_{OHM}	Cost of joule heating in leads
C_L	Total leads cost, object function, $C_I + C_C + C_F + C_M + C_{OHM}$
P_B	Magnetic pressure in coaxial leads = $B_{\theta}^2/2\mu_0 = I^2/8\pi r$
$r(z)$	Shape of generalized leads structure
K_{OHM}	$\bar{\eta}_{\max}^2 t_f/8\pi^2$ (Eq. (B-14))
K_C	$[(\mu_0/8\pi^2)\int_0^{t_f} I^2 dt]^2/2\rho_C$ (Eq. (B-12))
K_1	$2\pi c_I \rho_I \Delta_I$ (Eqs. (B-15), (B-16))
K_2	$4\pi c_C \rho_C$ (Eqs. (B-15), (B-16))
K_3	$c_e [(\Delta_I + \Delta/2)\mu_0 I_f^2/4\pi + \bar{\eta}_{\max}^2 t_f/2\pi\Delta]$ $\approx c_e (\mu_0/4\pi) [I_f^2 \Delta_I + \Delta(I_f^2/2 + \pi I_{\max}^2)]$ (Eqs. (B-15), (B-16))
K_4	$c_e (\mu_0^2/32\pi^3) [(\int_0^{t_f} I^2 dt)^2 + 2I_f^2 \int_0^{t_f} \int_0^t I^2 dt' dt]$ $\approx c_e (\mu_0^2 I_{\max}^2 t_f^2/128\pi^3 \rho_C) (I_{\max}^2 + 2 I_f^2)$ (Eqs. (B-15), (B-16))
F	$K_1 = 2\pi c_I \rho_I \Delta_I$
G	$K_3 + 2(K_2 K_4)^{1/2}$

Defining ds as an element of length along an arbitrarily shaped leads geometry, the total leads cost is composed of the following components.

Insulator Cost

$$C_I = 2 \pi c_I \rho_I \Delta_I \int r ds , \quad (B-2)$$

Conductor Cost

$$C_C = 4 \pi c_C \rho_C \int \Delta_C r ds , \quad (B-3)$$

Energy cost (stored field energy)

$$C_F = 2 \pi c_e \int P_B(t_f) \Delta_B r ds , \quad (B-4)$$

Kinetic energy of conductor motion

$$C_M = 4 \pi c_e \int W_C r ds , \text{ and} \quad (B-5)$$

Joule heating

$$C_{OHM} = 4 \pi c_e \int W_{OHM} r ds , \quad (B-6)$$

where integration is made along the leads from the liner to a nondestructible electrical connection (Fig. B-1).

The objective of this cost optimization is to compute a trajectory $r(z)$, and conductor thickness $\Delta_C(z)$, which minimizes the total cost, $C_T = C_I + C_C + C_F + C_M + C_{OHM}$, for leads connecting a liner connector ring at $(r_{10}, z = 0)$ to an energy supply ring at (r_s, z_s) . The insulator thickness Δ_I (Eq. (B-2)) is determined by the breakdown voltage of the insulator. P_B in Eq. (B-4) refers to the magnetic pressure and energy density between conductors and is given by

$$P_B = B^2/2\mu_0 = \mu_0 I_d^2/8\pi^2 r^2 . \quad (B-7)$$

Although P_B varies slightly as a function of r between conductors, this dependence is neglected, and $r(z)$ is taken as the centerline of the insulator. Only the field energy that remains in the leads at the end of an implosion t is lost; this point is important because $I(t)$ may be much smaller than the peak current. The "energy effective" separation of the conductors, Δ_B , is defined as the equivalent separation of two perfect conductors at t_f . For example, it is assumed that each conductor moves a

distance Δ_M during the pulse. In addition, the field energy is assumed to penetrate a conductor because of its finite resistivity. It is easily shown that this field penetration is equivalent to a conductor motion of $\Delta/4$, where Δ is the electrical skin depth. Combining the above, the apparent separation becomes

$$\Delta_B = \Delta_I + 2\Delta_M + \Delta/2 \quad . \quad (B-8)$$

The skin depth is normally computed for a constant, uniform resistivity and a sinusoidal current of angular frequency ω ,

$$\Delta = \sqrt{2\eta/\mu_0 \omega} \quad . \quad (B-9)$$

For the case of the FLR only a single pulse of duration t_f is of concern, and the resistivity varies in both space and time; joule heating is sufficient to melt a portion of the conductor. For simplicity an averaged value of η is taken and ω is replaced by π/t_f to give

$$\Delta = \sqrt{2 \eta t_f / \pi \mu_0} \quad , \quad (B-10)$$

Conductor motion, including Δ_M , will be discussed subsequently. In the optimized system Δ_M should be the same anyplace along the leads conductor; hence, Δ_B is fixed.

Proceeding to Eq. (B-5), conductor motion is computed using the impulse momentum approximation^{36,37}

$$v_c = (1/\rho_c \Delta_c) \int_0^{t_f} P_B dt \quad . \quad (B-11)$$

The corresponding kinetic energy per unit surface area of conductor is given by

$$\begin{aligned} W_c &= \rho_c \Delta_c v_c^2 / 2 \\ &= \left[(\mu_0 / 8\pi^2 r^2) \int_0^{t_f} I_d^2 dt \right]^2 / 2\rho_c \Delta_c \\ &\equiv K_c / \Delta_c r^4 \quad . \end{aligned} \quad (B-12)$$

Likewise conductor displacement can be computed from

$$\Delta_M = \int_0^{t_f} v_c dt \quad . \quad (B-13)$$

Joule heating is approximated by a simple skin-depth model

$$\begin{aligned}
 W_{\text{OHM}} &\approx \left[\int_0^{t_f} \eta I^2 dt \right] / (4\pi^2 \Delta r^2) \\
 &\approx \bar{\eta} I_{\text{max}}^2 t_f / (8\pi^2 \Delta r^2) \\
 &\equiv K_{\text{OHM}} / r^2
 \end{aligned} \tag{B-14}$$

Equations (B-2)-(B-6) are combined and rewritten to form a single object function for total leads cost

$$\begin{aligned}
 C_L = 2\pi \int &\left[r(c_I \rho_I \Delta_I + 2 c_C \rho_C \Delta_C) \right. \\
 &+ (\mu_0 I^2 \Delta_B / 8\pi^2 + 2K_{\text{OHM}}) / r \\
 &\left. + 2 K_C / r^3 \Delta_C \right] ds .
 \end{aligned} \tag{B-15}$$

Consideration of Eqs. (B-8), (B-11), and (B-13) indicates that the only variables to be optimized in Eq. (B-15) are r and Δ_C ; in this case the object function can be reconstituted as follows

$$C_L = \int \left[r(K_1 + K_2 \Delta_C) + K_3 / r + K_4 / \Delta_C r^3 \right] ds, \tag{B-16}$$

where K_1 , K_2 , K_3 , and K_4 are appropriately defined parameters (Table B-I). For a given leads geometry $r(z)$, the total cost C_L shows a minimum as the conductor thickness increases: for small thicknesses, Δ_C , considerable kinetic energy is imparted to the leads, whereas for large thicknesses the conductor materials cost dominates. More specifically, the K_1 term in Eq. (B-16) represents the insulator and/or refabrication cost, the K_2 term is associated with the conductor and/or refabrication cost, the K_3 term corresponds to joule heating (neglecting inductive energy stored in the leads at time t_f), and the K_4 term represents kinetic energy imparted to the leads (again neglecting stored inductive energy at time t_f). Generally, $I_d(t) \approx I_{\text{max}} \sin \pi t / t_f$, so that at time t_f little current or inductive energy resides in the leads. This leads cost is now optimized with respect to the conductor thickness Δ_C .

On differentiating the integrand of Eq. (B-16) with respect to Δ_c and solving for the optimum conductor thickness Δ_c^*

$$\Delta_c^* = \sqrt{K_4/K_2/r^2} \quad . \quad (B-17)$$

It is easily shown that Eq. (B-17) implies that at $\Delta_c = \Delta_c^*$ the conductor and kinetic energy costs are equal. The object function C_L is reduced to the following expression upon substitution of Δ_c^* for Δ_c

$$\begin{aligned} C_L &= \left[r K_1 + (K_3 + 2\sqrt{K_2 K_4})/r \right] ds \\ &= \int (F r + G/r) ds \quad . \end{aligned} \quad (B-18)$$

A final simplification is to define an optimum radius $r^* \equiv \sqrt{G/F}$, and the object function becomes

$$C_L = F \int (r + r^{*2}/r) ds \quad . \quad (B-19)$$

The designation as "optimum radius" was given to $r^* = \sqrt{G/F}$ because the optimal radius for a long coaxial cable equals r^* , in that this radius minimizes the integrand of Eq. (B-19). For a short coaxial cable, such as connects $(r_o, 0)$ and (r_s, z_s) in Fig. B-1, an optimum trajectory for Eq. (B-19) must be found using the variational principle.

To minimize Eq. (B-19) with respect to r , the variable of integration is changed to z , and the first variation is taken, where r' designates the derivative with respect to z .

$$\begin{aligned} &\delta \int_0^{z_s} (r + r^{*2}/r)(1 + r'^2)^{1/2} dz \\ &= \int_0^{z_s} \left[(1 - r^{*2}/r^2)\delta r + (r + r^{*2}/r)r'\delta r' / (1 + r'^2) \right] (1 + r'^2)^{1/2} dz \\ &= \int_0^{z_s} \left[(1 - r^{*2}/r^2) / (1 + r'^2) \right. \\ &\quad \left. - (1 + r^{*2}/r)r'' / (1 + r'^2)^2 \right] \delta r (1 + r'^2)^{1/2} dz \\ &+ \left[(r + r^{*2}/r)r'\delta r / (1 + r'^2)^{1/2} \right]_0^{z_s} = 0 \quad . \end{aligned} \quad (B-20)$$

The resulting Euler equation is

$$(r + r^{*2}/r)r'' - (1 - r^{*2}/r^2)(1 + r'^2) = 0 \quad (B-21)$$

In solving this equation two boundary conditions are applied when the leads are specified to connect both to the liner at $(r_{10}, 0)$ and to the boundary that delineates the blast zone (r_s, z_s) . Equation (B-21) was solved numerically, and the results are plotted in (r, z) space normalized to the initial liner radius r_{10} (Fig. B-2). Each plot has been constructed for a range of normalized total costs C_L , expressed as $\zeta = C / r_{10}^2 c_I \rho_I \Delta_I$.

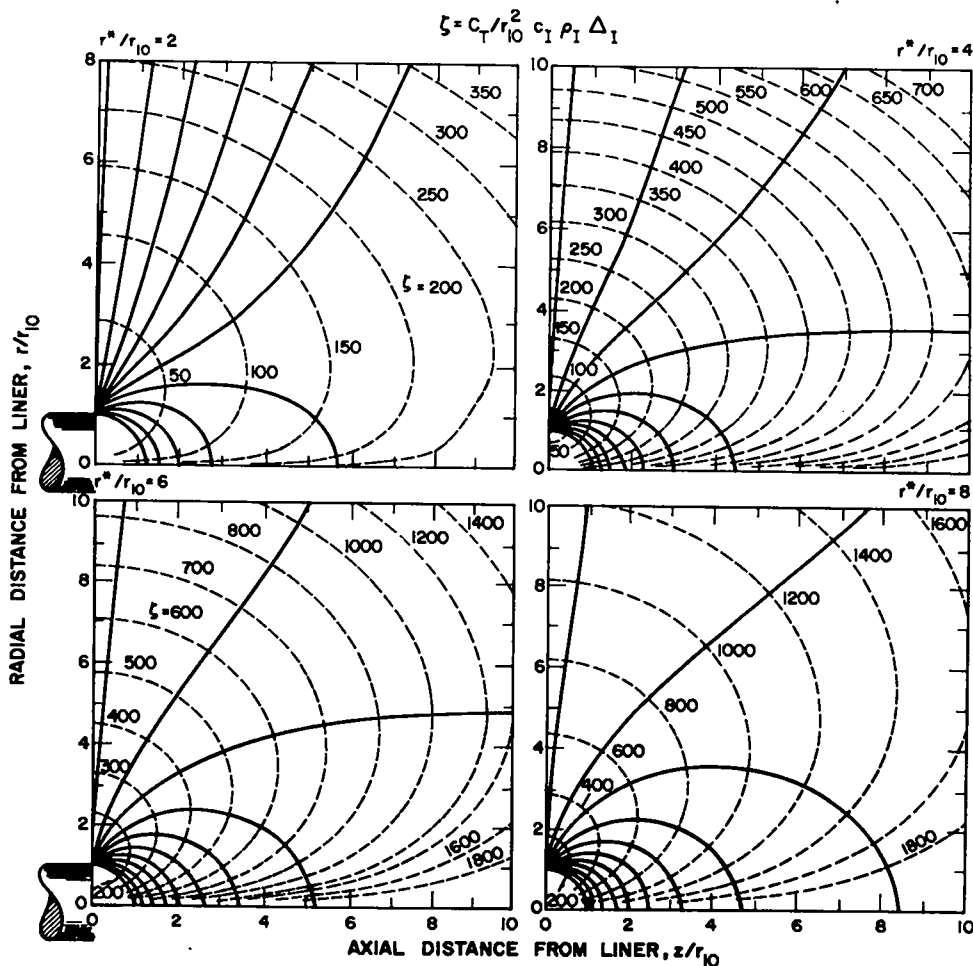


Fig. B-2. Cost-optimized coaxial lead shapes for four values of r^*/r_{10} (Eq. 2 (B-19)). Curves of constant cost, expressed as $\zeta = C_T/r_{10}^2 c_I \rho_I \Delta_I$, are shown.

The remaining cost and physical parameters are embodied in the ratio $r/r_0 = \sqrt{G/F} = [K_3/K_1 + 2(K_2K_4)^{1/2}/K_1]^{1/2}$ (re: Table B-I), which is taken as 2, 4, 6, and 8 in Fig. B-2. The dashed curves in Fig. B-2 are drawn orthogonal to the leads shape curves $r(z)$; these curves represent lines of constant $\zeta = C_L / r_{10}^2 c_I \rho_I \Delta_I$; the iso- ζ curves begin at the $(r/r_{10} = 1, z = 0)$ point and expand outward from this point in constant increments of $\Delta\zeta = 50$. Hence, for the conditions adopted in Sec. III.B.4 and Appendix C ($r_{10} = 0.2$ m, $c_I = 0.10$ \$/kg, $\rho_I = 2.5(10)^3$ kg/m³, $\Delta_I = V/E_D = 2(10)^5$ (V)/4(10)⁷ (V/m) = $5(10)^3$ m) each iso- ζ curve corresponds to an incremental increase in C_L equal to 2.50 \$/shot.

Table B-II summarizes typical cost and physical parameters to give physical significance to the four assumed values of r^*/r_{10} used to generate Fig. (B-2). For the assumed values given on Table B-II, $r^*/r_{10} = 2.9$.

The following points can be made with respect to the trade-offs embodied in this coaxial leads optimization. First, conductor refabrication costs and the cost of imparting parasitic kinetic energy to the leads are equally costly (Eq. (B-17) and associated discussion). By varying the conductor thickness Δ_c , rather than selecting the optimum value Δ_c^* , the total cost C_L will vary to second order with Δ_c (i.e., as Δ_c^2). Second, for the case where $r^*/r_{10} = 1$ (typically, $r^*/r_{10} \approx 2-3$, Table B-II), the leads cost is partitioned as follows: insulator (50%), conductor (18%), joule heating (14%), and kinetic energy (18%). Significantly, half of the cost of the coaxial leads per unit length is associated with insulator cost for $r_{10} = r^*$ (0.57 m for the typical values assumed in Table B-II). For greater initial liner radii, the insulator costs will dominate. As r_{10} is decreased below r^* , the conductor, joule heating, and kinetic energy costs will dominate the leads cost. Third, for straight leads sections with $r_{10} = r^*$, $\partial C_L / \partial r = 0$ and $\partial^2 C_L / \partial r^2 > 0$; hence, C_L increases as r departs significantly from r^* . Last, as seen from Fig. (B-2), the most economical, close access to the liner is provided by radial feedplates. For $r_{10} = 0.2$ m, these figures go to a maximum radial and axial extent of 2 m. Interpolating Figs. (B-2) for $r^*/r_{10} = 2.9$ (Table B-II), using 2.50 \$/shot for every increment of 50 in the parameter ζ , 20 \$/shot would be required to operate a 2-m-radius feedplate or 23 \$/shot would be expended for 2-m-long, shaped coaxial lead with a 0.5-m radius at the outer or power connection.

For larger blast radii the coaxial lead would become more economical than the radial feedplate, whereas the radial feedplate would be the economic choice for smaller blast radii.

Although it has been shown that an optimization of a generalized coaxial feedplate is possible, these optimal leads costs per shot are excessive when realistic blast radii are imposed. Total leads cost on the order of 20-25 \$/shot would be incurred for these cost-optimized cases; these best cases for the coaxial lead structure are about twice as expensive as the "force-reduced" interleaved structure discussed in Sec. III.B.4. In essence, the "force-reduced" design minimizes the liner mass needed to maintain inertially the leads structure intact during the pulse as well as keeping the internal stored energy to a minimum. The interleaved leads may also be confined to a small tube as compared to the bulky, shaped coaxial leads in Fig. B-2. The cost and handling advantages associated with the interleaved leads approach, however, must be weighed against the inherently more complex structure, which was not factored into the analysis in terms of a potentially higher fabrication cost.

TABLE B-II
SUMMARY OF COST AND PHYSICAL PARAMETERS USED TO EVALUATE
THE DEPENDENCE OF THE OPTIMUM LEADS CONFIGURATIONS ON THE
PARAMETER r^*/r USED IN FIG. B-2

Definition	Value
Time to final compression, t_f (s)	$2(10)^{-5}$
Peak voltage, V_{\max} (v)	$2(10)^5$
Peak current, I_{\max} (A)	$2.5(10)^8$
Time-average resistivity, $\bar{\eta}$ (ohm m)	$1.0(10)^{-6}$
Insulator density, ρ_I (kg/m ³)	$2.5(10)^3$
Conductor density, ρ_C (kg/m ³)	$1.0(10)^4$
Dielectric breakdown strength of insulator E_D (V/m)	$4(10)^7$
Insulator thickness, Δ_I (m) = V_{\max}/E_D	$5(10)^{-3}$
Unit cost of insulator, c_I (\$/kg)	0.10
Unit cost of (recycled) conductor, c_C (\$/kg)	0.01
Energy cost c_e (\$/J)	$1.11(10)$ (40 mills/kweh)
Initial liner radius, r_{10} (m)	0.2
Evaluated constraints:	
$F = K_1 = 2 c_I \rho_I \Delta_I = 7.85 \text{ \$/m}^2$	
$K_2 = 4\pi c_C \rho_C = 1257 \text{ \$/m}^3$	
$= (2 \bar{\eta} t_f / \mu_0)^{1/2} = 3.2(10)^{-3} \text{ m}$	
$K_3 = c_e \mu_0 I_{\max}^2 \Delta_I / 4 = 0.70 \text{ \$}$	
$K_4 = c_e \mu_0^2 I_{\max}^2 t_f^2 / (128\pi^3 \rho_C) = 6.9(10)^{-4} \text{ \$/m}^3$	
$r^* = 0.57 \text{ m}$	
$r^*/r_{10} = 2.9$	

APPENDIX C
OPTIMIZATION OF INTERLEAVED LEADS STRUCTURE

Although the FLR study has not progressed to a point where a comprehensive cost optimization can be made, the destruction of liner and leads structure is recognized as a potential and serious economic problem. The relatively complex lead and liner assembly depicted in Fig. III-10 is assumed to be Pb, LiPb, or Li, and once destroyed melts into and becomes a part of the Li or LiPb coolant; the conductor cost is envisaged as one of refabrication by a co-extrusion process rather than a materials cost. The insulator, on the other hand, probably will not be amenable to direct recycle, it will appear as a slag on the coolant surface in the sump (14, Fig. II-1) after each shot, and it will probably represent a major fabrication cost. The simple economic optimization of the interwoven leads structure, therefore, focuses parametrically onto the fabrication cost allowed for the insulator. This optimization uses as an object function the total cost of electricity as a function of major leads parameters and a composite total plant cost; the liner cost is assumed to be a small fraction of the total cost of the leads/liner assembly.

In addition to the cost of leads material destroyed, the ohmic heating in the lead structure represents another cost penalty. Although this ohmic-heating energy requirement per se is reflected in a higher recirculating power requirement and, therefore, is not charged directly to the leads cost, the additional capital investment associated with the added energy transfer and storage (ETS) required to supply the ohmic loss does appear as a direct leads cost. If the voltage V applied to the leads appears primarily to supply resistive-like liner elements (i.e., time-varying liner inductance), then $V \approx I_d \ell \mu_0 / 2\pi t_f$, where ℓ is the length of the liner, I_d is the liner drive current, and t_f is the liner "run-in" time. Hence, the energy delivered to the liner W_L (J) and the liner Q-value are given by

$$W_L \approx I_d^2 \mu_0 \ell / 2 \tag{C-1}$$

$$Q \approx \xi (W_L / \ell)^{1/2} \tag{C-2}$$

where the scaling parameter ξ is obtained from separate analytic and numerical computations of the liner physics described in Sec. III.A and Ref. 17.

If $A = \pi (r_o^2 - r_i^2)$ is the total cross-sectional area of the leads (re: Fig. III-10), λ is the conductor (volume) filling fraction, η is the conductor resistivity, and $\Delta = 2(\eta\tau/\mu_o)^{1/2}$ is the conductor width (two skin depths, Fig. III-10), the energy deposited into the leads as ohmic heating equals

$$W_{OHM}(J) \approx 2\pi W_L \Delta^2 R / \lambda A_C \quad , \quad (C-3)$$

where R is the length of destroyed leads (equal to a fraction, 0.3-0.5, of the blast radius) and $A_C = \lambda A$ is the conductor area.

The virial theorem^{37,38} is used to estimate the blast radius R required to contain any explosive energy release equal to $W_L + W_\alpha$, where W_α is the alpha-particle yield. For a spherical vessel of wall thickness ΔR and allowable (fatigue) stress σ ,

$$R_B^2 \Delta R \geq (W_L + W_\alpha) / 4\pi\sigma \quad . \quad (C-4)$$

Given that $c_{ETS}(\$/J)$ is the amortized, "per-shot" cost of the ETS system, $c_C(\$/kg)$ is the conductor or metal refurbishing cost, and $c_I(\$/kg)$ is a similar cost for insulator, the cost per shot of the leads structure becomes

$$C_L(\$) = 2\pi(W_L/\lambda)(\Delta^2 R/A_C)c_{ETS} + [\rho_C c_C + \rho_I c_I(1-\lambda)/\lambda] A_C R \quad , \quad (C-5)$$

where, if $E_D(V/m)$ is the dielectric strength of the insulator, $\lambda = 1/(1+V/\Delta E_D)$. On the basis of Eq. (C-5) an optimum leads area, A or $A_C = \lambda A$, is evident; small A_C reflects a high ETS cost and large A_C reflects a high materials cost. If $W_E(J)$ represents the net electrical energy generated by each implosion, then the electrical cost associated with the leads is simply C_L/W_E . Given that the total plant capital investment is $P_I(\$/We)$, p_I is the annual return on investment, and that $\sim \pi(10)^7$ seconds equal a year, the total energy cost can be approximated by

$$c_E(\$/J) = [P_I p_I / \pi(10)^7 + C_L / W_{ET}] / (1-\epsilon) \quad , \quad (C-6)$$

where $W_{ET} = W_E / (1-\epsilon)$ is the total electrical energy generated per implosion, and the recirculating power fraction ϵ , according to Fig. III-7, and

Eq. (III-18) is given by

$$1/\varepsilon = Q_E = \eta_T^{EX} \eta_{TH} \left[\eta_T^{INT} Q(0.2 + 0.8 M) + 1 \right] / (1 + f_{PO} + f_{AUX}) \quad (C-7)$$

It is easily shown that the internal transfer efficiency is η_T^{INT} given by

$$W_{OHM}/W_L = 1/\eta_T^{INT} - 1 = 2\pi\Delta^2 R/\ell A_C \quad (C-8)$$

Substitution of Eqs. (C-8), (C-7), and (C-5) into Eq. (C-6) gives the following expression for the cost of energy, c_E (\$/J), which serves here as an object function to be minimized with respect to leads configuration.

$$c_E (\$/J) = \eta_T^{EX} \left[\alpha_1 + \alpha_2 A_C + \alpha_3 A_C^2 \right] / \left[\alpha_4 A - \alpha_5 \right] \quad (C-9)$$

where

$$\alpha_1 = \left[\eta_{TH} P_I P_I / \pi(10)^7 + c_{ETS} \right] 2\pi\Delta^2 R / \ell$$

$$\alpha_2 = \left[\eta_{TH} P_I P_I / \pi(10)^7 \right] \left[1 + (.8 M + 0.2) Q \right]$$

$$\alpha_3 = R \left[\rho_C c_C + \rho_I c_I (1-\lambda) / \lambda \right] \xi^2 / Q^2 \ell$$

$$\alpha_4 = \eta_T^{EX} \eta_{TH} \left[1 + (.8 M + .2) Q \right] - 1$$

$$\alpha_5 = 2\pi\Delta^2 R \left[1 - \eta_T^{EX} \eta_{TH} \right] / \ell$$

Differentiation of Eq. (C-9) with respect to A_C gives the following expression for the cost optimized leads area $A_C = \lambda A$

$$A_C^* = (\alpha_5 / \alpha_4) \left[1 + \sqrt{1 + \alpha_4 (\alpha_4 \alpha_1 + \alpha_2 \alpha_5) / \alpha_3 \alpha_5^2} \right] \quad (C-10)$$

The optimized total energy costs (Eqs. (C-9) and (C-10)), the fraction of these costs associated with the leads, and the associated engineering Q-value Q_E (Eq. (C-7)) are evaluated parametrically as a function of insulator cost c_I (\$/kg) on Fig. C-1 for the fixed parameters given on Table C-I.

Generally, the cost-optimized leads areas given by Eq. (C-10) will result in melting of the lead conductor some time into the energy transfer, and the

appropriate liquid resistivity was used. If on the other hand A_C was specified to assure that melting occurred only after the energy transfer, then A_C is given by

$$A_C = \left[2\pi W_L \Delta^2 / \rho \Delta H_M \rho_C \right]^{1/2}, \quad (C-11)$$

where H_M (J/kg) is the energy required to melt the conductor starting from 300 K. The dependence of c_E (\$/J) and the fraction of c_E (\$/J) attributable to leads cost is also shown on Fig. C-1 as a function of insulator cost. For the range of liner energies W_L and optimization procedures used as a basis for the data on Fig. C-1, it appears that for either melting or non-melting leads options the insulator cost must be kept below $c_I \approx 0.10$ \$/kg if the FLR plant efficiency and economic viability are not to be compromised. Generally, the cost of glass-like insulator fabrication in simple but mass-produced geometries is expected to be near the energy cost associated with melting,⁴⁷ which for methane amounts to 0.02 \$/kg at present costs.

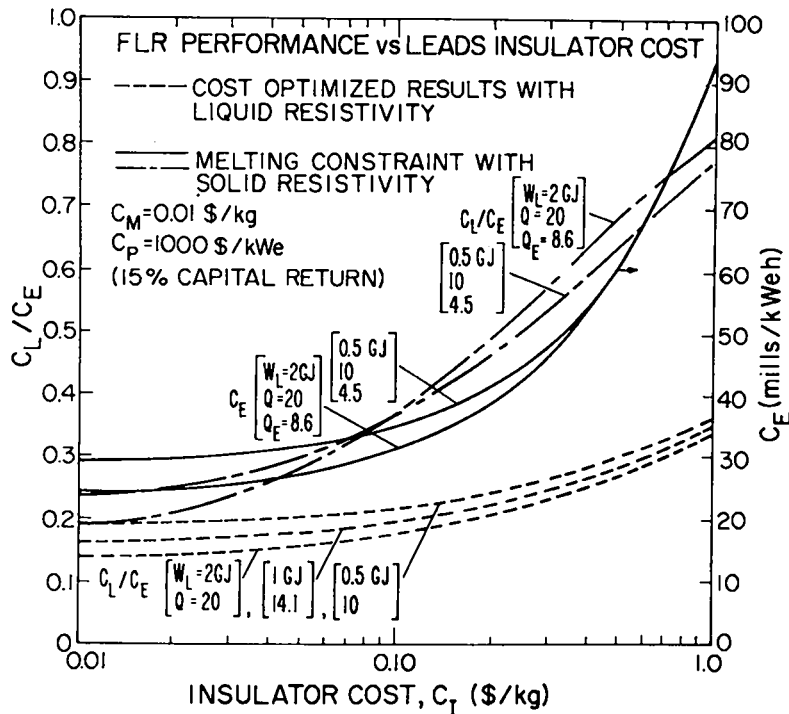


Fig. C-1. Dependence of leads cost relative to power cost on the unit cost of insulator for a fixed cost of conductor recycle (0.01 \$/kg). Cost-optimized and non-melting constraint are imposed. The actual power costs are also shown for the non-melting constraint imposed.

TABLE C-I
FIXED PARAMETERS USED IN "FORCE-REDUCED" LEADS OPTIMIZATION

Conductor (lead) resistivity, η (ohm-m)	$2(10)^{-7}$ (solid), $1(10)^{-6}$ (liquid)
Liner "run-in" time, t_f (s)	$45.(10)^{-6}$
Cycle time, τ_c (s)	10.
Maximum stress in blast vessel, σ (Pa)	$68(10)^6$
Blast vessel thickness, ΔR (m)	0.3
Blast radius fraction, R/R_B	0.5
Liner length, l (m)	0.2
Conductor density, ρ_c (kg/m ³)	$10.5(10)^3$
Insulator density, ρ_I (kg/m ³)	$2.5(10)^3$
Melting energy for conductor, ΔH_{MC} (J/kg)	$6.34(10)^4$
Melting energy for insulator, ΔH_{MI} (J/kg)	$1.41(10)^6$
Insulator dielectric strength, E_D (V/m)	$4.0(10)^7$
Voltage applied to leads, V (V)	2.5×10^5
Conductor volume fraction, λ	0.7
Cost of metal, c_c (\$/kg)	0.01
Installed cost of energy storage, c_{ETS} (\$/J)	0.01
Plant costs, P_I (\$/W _e)	1.0
Return on capital, p_I (1/y)	0.15
Thermal conversion efficiency, η_{TH}	0.4
External ETS transfer efficiency, η_T^{EX}	0.95
Blanket neutron energy multiplication, M	1.25
Scaling parameter for liner yield, ξ (M/J)	$2.0(10)^{-4}$
Auxiliary power fraction, $f_{AUX} = W_{AUX}/W_{ETS}$	0.06
Plasma preparation fraction, $f_{PO} = W_{PO}/W_{ETS}$	0.04

APPENDIX D

DESCRIPTION MCNP MONTE CARLO CALCULATION

The Monte Carlo code is the continuous energy code MCNP.³¹ Any number (limited only by the storage capabilities of the computer) of geometric cells bounded by first- and second-degree surfaces, as well as some fourth-degree surfaces, can be treated by the code. The subdivision of the physical system into cells is not necessarily governed by the different material regions occurring, but may take into consideration the problems of sampling as well as the restrictions necessary to specify a unique geometry.

Included in the code are standard variance-reducing techniques, which are optional. These include particle-splitting and Russian-roulette and path-length stretching techniques. Provision is made to force collisions in designated cells, thereby obtaining flux estimates at point detectors; provisions are also made for calculating reactions in small regions for use as track-length estimators.

Source specification is flexible in MCNP. The specification of a source particle consists of geometry-location, angular description, energy, time, and particle weight. In addition, probability distributions can exist for any of these variables. Considerable detail is possible in describing a neutron or gamma-ray source or both.

One of the advantages of the MCNP code is that neutron data are processed in a continuous energy sense. The cross sections are read into the code in considerable detail in an attempt to use the information with no significant approximations or distortions. Pointwise neutron cross sections are provided at discrete energies and are tabulated in the Monte Carlo library on an energy grid that is tailored to each isotope. Linear interpolation is used between energy points, with a few hundred to several thousand points typically required. Cross sections are added at a sufficient number of points to insure that the linear interpolation constraint reproduces the original cross section tabulation within a specified tolerance. Furthermore, the cross sections are unionized so that all reactions are given the same energy grid.

All reactions given in a particular cross-section evaluation (such as ENDL or ENDF/B) are taken into account. A choice of three sources of cross sections for most isotopes is available: ENDF/B-IV, ENDL from LLL, and the British (AWRE) library. Resonance parameters, if they are given in the

evaluation, are processed at several temperatures and the resulting resonance cross sections are added to the pointwise cross sections.

Data for the energy distribution of secondary neutrons are used directly in terms of the "laws" prescribed in the particular cross-section evaluation. Angular distributions for elastic and inelastic scattering events are stored in the Monte Carlo library for 32 equally probable bins on a fine grid of incident neutron energies.

The MCNP code includes a thermalization routine that employs a free-gas model. Below a thermal cut-in energy, the lighter atoms are assumed to be in thermal motion, with a Maxwellian distribution of velocities determined by the thermal temperature of the region. Each cell of the problem has specified a unique thermal temperature. Scattering from the light nuclei includes the effect of thermal motion. For nuclei belonging to the heavier groups of atoms and for energies in the thermal range, elastic scattering is assumed to occur in the laboratory system with no energy loss.

APPENDIX E

USE OF THE VIRIAL THEOREM AND A SIMPLE SHOCK MODEL TO ESTIMATE BLAST EFFECTS IN VACUUM AND TWO-PHASE MEDIA

Prior to implementation of program PAD³⁹ for blast mitigation modeling (Sec. III.B.6), two simple approaches to the problem were considered. First, the "virial theorem"³⁷ provides the simplest model of blast containment in an evacuated vessel. The second approach describes outgoing and reflected shock waves in "mitigating" media using the Hugoniot relations.⁴⁸ Both of these techniques are applied here to a 1.13-GJ blast energy described earlier.⁹

1. Virial-Theorem Approach. As a preliminary approach to the blast-containment problem a convenient baseline for explosive containment is provided by the "virial theorem."³⁷ One form of this theorem³⁶ predicts that the mass M of a vessel needed to contain a gas or plasma of energy W must satisfy the relationship

$$M \geq 2 W / f \sigma \quad , \quad (E-1)$$

where ρ is the density of the containment vessel, f is the number of stress components in the vessel wall ($f = 2$ for a spherical vessel of radius R and thickness ΔR), and σ is the minimum stress. Taking $M = 4\pi R^2 \Delta R \rho$ and $f = 2$, Eq. (E-1) becomes

$$R \Delta R \geq (W/R) / 4\pi \sigma \quad . \quad (E-2)$$

The relationship between tangential stress σ and strain ϵ for thin-walled spheres, $\Delta R \ll R$, is given by³⁸

$$\sigma = E \epsilon / (1 - \nu) \quad , \quad (E-3)$$

where ν is Poisson's ratio, and E is Young's modulus. Substituting Eq. (E-3) into Eq. (E-2) gives the following expressions for the virial theorem if ϵ is expressed as microstrain

$$\begin{aligned}
 (\Delta R/R) \epsilon &\geq (1-\nu) (W/R^3) 10^6 / 4 \pi E \\
 &\geq 2.93 (10)^{-7} (W/R^3) \\
 &\geq 1.85 (M_{HE}/R^3)
 \end{aligned}
 \tag{E-4}$$

where $\nu = 0.3$, $E = 1.9(10)^{11}$ Pa ($28(10)^6$ psi), and M_{HE} has the units of kg-equivalent high explosive (HE, 1.5 times the TNT equivalent, 4.2 MJ/kg). Equation (E-4) is compared to experimental data³⁵ in Fig. E-1; these data were obtained at the inception of failure of spherical, steel vessels that were subjected to gradually increased high-explosive charges up to ~ 20 -kg mass. As seen from Fig. E-1, the presence of blast-mitigating or shock-transmitting material within the vessel has a significant effect on the vessel response. The virial theorem shows good agreement with the vacuum case, as is expected; the presence of air or other fluid media leads to shock formation, whereas the pulverization of vermiculite gives an important dissipative channel for blast energy.

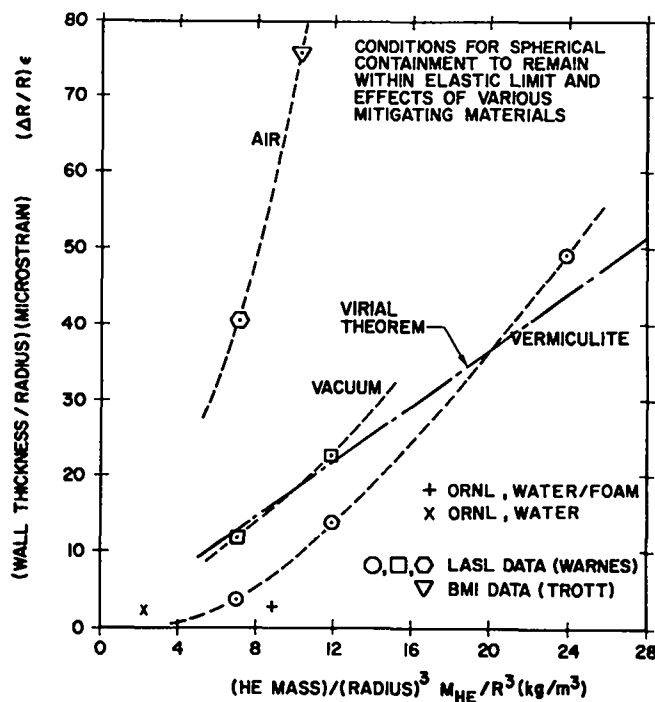


Fig. E-1. Virial-theorem scaling of blast-confinement data using high-explosive (HE) detonations with spherical vessels. All data represent tests which measured only the onset of plastic deformation of the blast-containment vessel. ORNL (Ref. 33), LASL (Ref. 35), BMI (Ref. 49).

As seen from the analyses in Secs. III.A.4 and III.B.6, energy releases equivalent to ~ 350 kg of TNT (~ 230 kg HE) are expected for recirculating power fractions ~ 0.25 . Taking $R = 2.5$ m, $M_{HE} = 230$ kg, and $\epsilon = 3000$ (failure limit for the steel vessels considered in Fig. E-1, failure generally indicated by beginning of plastic deformation), the required single-shot vessel thickness would be ~ 20 - 25 mm for a "vacuum" or "vermiculite" response.

2. Cyclic Fatigue Constraints. Although some of the data points on Fig. E-1 represent as many as 10 detonations of increasing magnitude, the vessels were always exposed to blast intensities that were sufficiently close to the failure threshold to preclude a serious investigation of many-cycle fatigue limits. Fatigue limits should dramatically alter the "single-shot" predictions given above.

The microstrain $\epsilon = 3000$ selected for the above evaluation of ΔR for $R \sim 2.5$ m generally assures the plastic limit is not exceeded, but this microstrain is too large from the viewpoint of cyclic fatigue. The microstrain must be determined from the fatigue characteristics and desired fatigue life of the containment vessel. Coffin⁴⁰ has correlated the plastic strain $\Delta\epsilon_p$ and elastic strain $\Delta\epsilon_e$ with material properties and the number of cycles to failure N_f according to

$$\Delta\epsilon_p = C_2 v_c^{B(1-k)} / N_f^\beta \quad (E-5)$$

$$\Delta\epsilon_e = (A'/E) v_c^{k'} / N_f^{\beta'} \quad , \quad (E-6)$$

where $\epsilon \approx \Delta\epsilon_p + \Delta\epsilon_e$, and the constraints for 304 stainless steel at 800 K and 923 K are summarized in Table E-I. The last two entries in Table E-I are the microstrains evaluated at the respective temperatures for failure after one year ($N_f = 2.5(10)^6$) and ten years of operation for $\tau_c = 10$ s ($v_c = 6 \text{ min}^{-1}$) and an 80% plant factor. Taking the 800 K values, based upon corrosion limits, a ten-year lifetime would require $\Delta R \geq 75$ mm for the above FLR conditions ($R = 2.5$ m, $M_{HE} = 230$ kg).

The use of the virial theorem in conjunction with an idealized spherical geometry provides a lower limit for the blast-confinement problem, although the agreement with the experimental "vacuum" data on Fig. E-1 lends confidence to this approach. Consideration of the vessel geometry anticipated for a real

TABLE E-I
 SUMMARY PARAMETERS USED TO FIT ANALYTICALLY 304 STAINLESS
 STEEL FATIGUE DATA,⁴⁰ EQS. (E-5) AND (E-6)

CONSTANT	800 K	900 K
C_2	$0.300(10)^6$	$1.108(10)^6$
	0.410	0.707
k	0.93	0.81
A'	$5.29(10)^{11}$	$2.26(10)^{11}$
E'	$23.4(10)^6$	$21.6(10)^6$
k'	-0.02	0.089
	0.20	0.187
$N_f = 2.5(10)^6$	1898	823
$N_f = 2.5(10)^7$	1016	516

engineering structure (i.e., stress concentration points, penetrations, acoustical responses, etc.) in conjunction with the formation of shocks will undoubtedly lead to larger vessel dimensions. The effect of shock generation in an intervening medium is examined approximately in the following section. Generally, however, the vessel dimensions based on the predictions of the virial theorem should be viewed as lower limits, and a detailed structural design is required before the containment problem can be further quantified.

3. Blast Confinement in a LiPb/He Bath. The original conceptualization⁵ of the FLR envisaged the use of a He-bubble-impregnated LiPb bath to attenuate the post-implosion blast. This system is shown schematically in Fig. III-23. Also shown are systems which operate in vacuum and in a fluidized bed of blast-mitigating material. For the former case the blanket must surround the vacuum vessel, whereas the fluidized bed might contain a lithium-bearing oxide with shock-mitigating properties similar to vermiculite (Fig. E-1). Only the LiPb/He containment scheme, which, as will be shown at best will respond according to the virial-theorem predictions (Sec.E-1), is addressed here.

3.1. Development of Shock Model. A simple model was developed to consider spherical shocks in liquid-gas mixtures. Specifically, a lead-lithium mixture is considered for the primary coolant and tritium breeding, and helium bubbles are used for shock mitigation. Dresner³² has suggested that shock mitigation would be enhanced by creating helium bubbles in the liquid metal.

The lead-lithium mixture is treated as an incompressible fluid and the helium as an ideal gas. Initially the helium occupies a fraction f_{He} of the mixture volume. For $f_{\text{He}} \ll 1$ the helium is simply considered as a fine dispersion of bubbles, and for $f_{\text{He}} \leq 1$ the lead-lithium is assumed to be in the form of a shower or mist of droplets. This latter case is treated in Sec. III.B.6.

The 14.1-MeV neutron heating will form a substantial shock in pure lithium for the fusion yields considered here, but a small fraction of helium bubbles should easily mitigate that shock.³² Most of this neutron energy heats the liquid-metal coolant/breeder. When bubbles are present, the thermal expansion of the liquid metal is easily taken up by the bubbles with little accompanying pressure-volume work, and most of the neutron energy remains as thermal energy in the lithium breeder. The post-burn energy which remains in the plasma and vaporized liner debris is of primary concern. The decompression of hot gas and plasma can perform far more work than a corresponding decompression of the neutron-heated coolant.

An energy $W \sim (W_L + W_\alpha)$ is assumed to heat an ideal gas or plasma of radius r_{10} equal to the initial liner radius. For the $\ell = 0.2$ -m-long liner this explosive energy is ~ 1.0 GJ. For this computation r_{10} is taken to be 0.20 m. An adiabatic expansion of the plasma is assumed. Setting the specific-heat ratio $\gamma = 5/3$ for this hot gas and defining r_i as the time-dependent inner radius of the post-implosion cavity created in the liquid-metal, the plasma pressure P_i as a function of r_i becomes

$$P_i = P_0 (r_{10}/r_i)^5, \quad P_0 = W/2\pi r_{10}^3. \quad (\text{E-7})$$

It is further assumed that a single shock travels from r_{10} to the radius of the vessel wall, R , where a second shock is formed and returns to the plasma/liquid-metal interface. During this inward motion of the reflected shock the highest pressures on the vessel wall would occur. In order to model the shock motion, the following definitions are made.

- r_s = radial position of shock (m)
 u_s = radial velocity of shock (m)
 u_p = fluid velocity behind shock (m/s)
 P_a = ambient pressure of LiPb-He mixture (Pa)
 V_L = specific volume of liquid LiPb = $1/\rho_{L3}$ (m^3/kg)
 V_a = specific volume of ambient LiPb-He (m^3/kg)
 f_{He} = initial helium fraction = $1 - V_L/V_a$
 P_s = pressure directly behind shock (Pa)
 V_s = specific volume behind shock (m^3/kg)
 E_a = ambient specific energy (J/kg)
 E_s = specific energy behind shock (J/kg)

Figure E-2 depicts the geometry and associated notation.

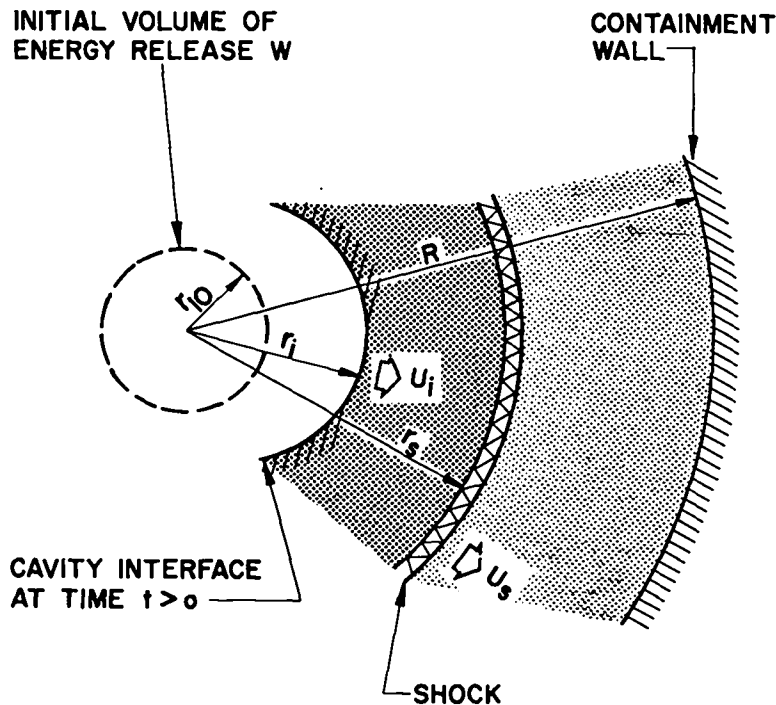


Fig. E-2. Schematic diagram of simple shock model used to describe the pressure loading of a thin spherical containment shell subjected to the reflection of a coherent shock generated in a liquid/gas mixture. Refer to text for notation.

Conservation of energy and momentum are used to derive the Hugoniot equations⁴⁸ that relate pressure, volume, energy, and velocity on one side of the shock to similar quantities on the other side

$$u_s = V_a \sqrt{(P_s - P_a)/(V_a - V_s)} \quad (E-8)$$

$$u_p = u_s(1 - V_s/V_a) \quad (E-9)$$

$$E_s - E_a = (P_a + P_s)(V_a - V_s)/2 \quad (E-10)$$

An equation of state (EOS) completes the relationship between properties on each side of this shock. Two EOS models are used; the first requires that the total increase in specific energy across the shock heats the helium bubbles

$$P_s V_s^\gamma = P_a V_a^\gamma \quad (\gamma = 5/3) \quad (E-11)$$

The second EOS model assumes that the shock heats the liquid metal, and the helium bubbles are adiabatically compressed

$$E_s - E_a = (3/2) [P_s(V_s - V_L) - P_a(V_a - V_L)] \quad (E-12)$$

These two models represent significantly different physics and will be discussed later.

To complete the equation of motion for the shock, the equations for acceleration and conservation of mass are introduced.

$$\rho_s (du_p/dt) + \nabla P_s = 0 \quad \text{and} \quad (E-13)$$

$$\Delta \cdot (\rho u_p) + \partial \rho / \partial t = 0 \quad (E-14)$$

At this point the simplifying assumption is made that once a volume element is compressed by passage of the shock the specific volume, V_s , does not change thereafter (i.e., $d\rho/dt = dV_s/dt = 0$). This assumption enables Eq. (E-14) to be replaced with the relation

$$r^2 u_p = r'^2 u'_p \quad (E-15)$$

where r and r' represent any two points behind the shock. Since fluid velocities and accelerations at all points are now related to one point (e.g., at the shock), Eq. (E-13) can be integrated over radius to yield an ordinary differential equation rather than a partial differential equation; this assumption greatly simplifies the numerical solution.

Undoubtedly a number of shortcomings and inconsistencies can be found with the assumption that $d\rho_s/dt = 0$ after passage of the shock. For instance, the resulting model does not apply to shocks in purely gaseous media, where compressed gas behind a shock would expand as the driving pressure decreases (Eq. (E-7)). When a liquid-gas mixture is shocked, such an expansion will certainly be reduced if not reversed. The hot, compressed gas would lose heat to the liquid and be less able to expand as described above.

Defining the following quantities

$$G = r_s \int_{r_i}^{r_s} (\rho_s / r_s^2) dr \quad \text{and} \quad (E-16)$$

$$H = r_s^4 \int_{r_i}^{r_s} (\rho_s / r_s^5) dr \quad , \quad (E-17)$$

and combining Eqs. (E-8), (E-9), (E-10), (E-13), (E-16), and (E-17) results in the following expression for the particle velocity u_p .

$$du_p/dt = - \left[(P_s - P_i)/G + 2u_p^2 (1-H/G - 1/(1-V_a/V_s)) \right] / r_s \quad (E-18)$$

A computer code was written to combine Eqs. (E-7), (E-8), (E-9), (E-10), (E-11), and (E-18) and to solve for $r_s(t)$.

The description of the reflected shock is greatly simplified here to give an average pressure during its reverse transit across the fluid. This model is coupled with the appropriate EOS (Eq. (E-11)) to solve for an average pressure during reflection, \bar{P}_r . The quantity t_{ra} is defined as the time for the outgoing shock to impact the vessel wall and t_{rb} as the time the reflected shock reaches the inner surface of the fluid. The average specific volume of the reflected shock is $V_r = 4/3\pi [R^3 - r^3(t_{rb})] / M_L$ where M_L is the total fluid mass. It is easily shown that

$$\bar{P}_r \approx \frac{u_p(t_{ra}) [R^2/r^2(t_{rb}) - 1]}{V_r(t_{rb} - t_{ra})} \quad (E-19)$$

Equation (E-19) is combined with Eq. (E-11) or Eq. (E-12) to solve for \bar{P}_r .

3.2. Computational Results. The results of several computations are shown in Fig. E-3. The tension in the vessel wall, $T = \bar{P}_r/R$ is compared to the virial-theorem result (Sec. E.1), $T_v = W/2\pi R^2$. The ratio T/T_v is equal to the ratio of respective tangential stresses σ/σ_v and is given in Fig. E-3 as a function of the helium fraction f_{He} for the following conditions:

$$W = 1.13 \text{ GJ}$$

$$\rho_L = 9400 \text{ kg/m}^3$$

$$R = 2.3 \text{ m}$$

$$r_{10} = 0.2 \text{ m and } 2 \text{ m}$$

The two EOS (Eqs. (E-11) and (E-12)) models give surprisingly similar results, as shown in Fig. E-3. A shock-heated gas is compressed to no less than 25% of its original volume; however, a much greater compression occurs when a portion of the shock heat is also delivered to the liquid metal. Typically the shocked helium would then occupy only a few percent of its original volume. Even with this significant difference the results agree to within an order of magnitude for any given value of f_{He} and $r_{10} = 0.2 \text{ m}$.

The results given here do not show a stress reduction such as that given by vermiculite (Fig. E-1). Although computed results show that shock heating can dissipate over 98% of the blast energy, sufficient momentum is generated in the liquid metal to produce substantial wall stresses compared to the predictions of the virial theorem. Two complementary phenomena appear to be in effect. When the helium is highly compressed, as for the EOS model of Eq. (E-12), a larger amount of energy is dissipated in the shock. When this more dense mixture (as compared to the EOS model of Eq. (E-11)) strikes the wall, the shock reversal is more sudden because of the smaller second compression that can occur.

The hydrodynamic computations of program PAD (Sec. III.B.6) do not support the predictions of an increase in wall stress, corresponding to the reduction of γ . The maximum stresses given in Fig. III-19 for a 1.46-GJ blast with $R = 2.6 \text{ m}$ were converted in terms of σ/σ_v and incorporated into Fig. E-3.

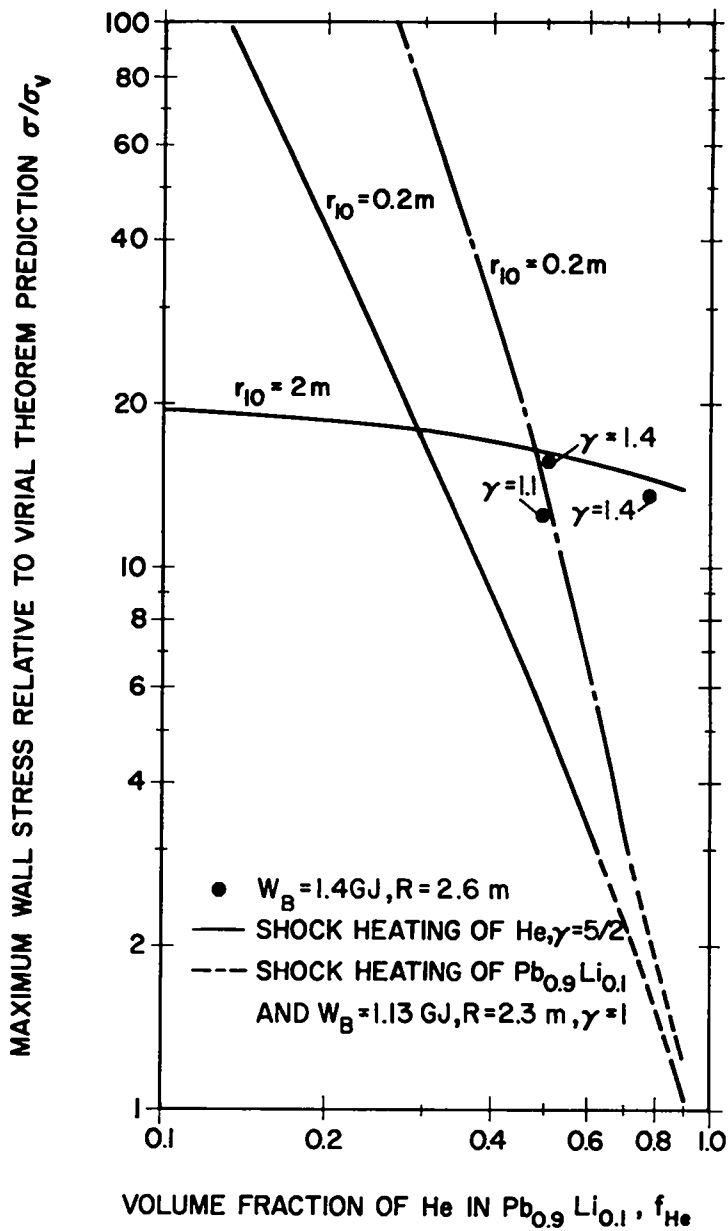


Fig. E-3. Dependence of maximum wall stress relative to predictions of the virial theorem as a function of the bubble void fraction. The energy released at the center of the spherical vessel is W , the vessel radius is R , and the specific heat ratio of the gas is γ . Shown also are results for similar conditions from the hydrodynamic code PAD.³⁹

Since W and R differ slightly between the two computations, comparison is not entirely justified, but trends are indicated. The PAD results with $f_{\text{He}} = 0.5$ fall close to the $\gamma = 1$ curve of the simple shock model; however, stresses increase with γ according to the PAD model, rather than decrease. Also, the PAD results do not show the sharp decrease in σ/σ_v as f_{He} approaches unity, as illustrated by the $f_{\text{He}} = 0.8$, $\gamma = 1.4$ point on Fig. E-3. Most of the discrepancies seen here probably arise because the simple shock model does not allow for expansion of shocked gas (i.e., $d\rho_s/dt = 0$).

Serious shortcomings of the simple models upon which Fig. E-3 is based are:

(a) The simple shock approach does not allow for expansion of a shocked gas (i.e., $d\rho_s/dt = 0$).

(b) Program PAD allows post-shock expansion according to an ideal gas law. In fact the liquid would be heated by irreversible processes, reducing expansion behind the shock to a level between the PAD and simple shock models.

(c) Although PAD incorporates an artificial viscosity to affect a shock, no detailed empirical knowledge of shocked gas-fluid mixtures is used. It may be necessary to wait for experimental results to improve this part of the model.

4. Conclusion. For 1.13 GJ of explosive energy released by a liner, the virial theorem predicts for a containment vessel radius $R = 2.0$ m that the wall thickness $\Delta R \approx 28$ mm based upon a "single-shot" criterion (microstrain $\epsilon = 3000$). Consideration of cyclic fatigue constraints (for 304 stainless steel) leads to a 2.5-m-radius vessel with $\Delta R = 75$ -mm wall thickness ($\tau_c = 10$ -s cycle time for a 10-year life at an 80% plant factor). The virial theorem predicts surprisingly well experimental data from vacuum detonations in spherical steel vessels. Using the virial theorem to scale experimental data from detonations in air-filled vessels results in significantly increased vessel wall thicknesses presumably because of momentum amplification by shock propagation in the gaseous medium.

A simple shock-propagation model was developed to investigate the shock mitigation properties of He-bubble containing lead-lithium liquid alloy. No reasonable bubble fraction could be found which resulted in containment-vessel wall stresses that are below the predictions of the virial theorem (vacuum medium); the acceleration of the lead-lithium mass causes significant pressure amplification for all He-bubble fractions considered and for two extreme EOS models used to describe the two-phase system.

A one-dimensional hydrodynamic code, PAD,³⁹ was used to model gas-liquid mitigators more carefully. Good agreement was seen between PAD and the simple shock model for equal initial volume fractions of gas and liquid, but wide discrepancies occur for small liquid fractions. Until more complete theoretical and/or empirical data are available, the most reliable results are for equal liquid-gas mixtures.

APPENDIX F
COSTING GUIDELINES, ACCOUNTING SYSTEM, AND DATA BASE

The comparison of the economic merits of one fusion concept with another can be made only if the basic cost estimates are performed on a uniform and normalized basis. Although the DOE/OFE is in the process of generating such a normalized basis,^{41,42} the required information is not complete and available to the fusion community. This study has adopted these procedures as they exist in interim form^{41,42} and when necessary has provided the missing components, again on an interim basis, in order that a complete cost estimation of the FLR concept could be completed within FY 1978. Presented here is a summary of the costing guidelines⁴¹ as they existed in early 1978; the cost accounting system and the cost data base used by this study are also included.

Table F-I summarizes the costing guidelines, whereas Table F-II summarizes the cost data bases that have been assembled from a number of sources indicated. If "0" is entered into the "unit cost" column in Table F-II, the cost of this item has been agglomerated into a higher level cost. If a "1" is entered into the "number of units" column, this item is acknowledged, but has been taken into account at a higher level. If a "0" is entered instead, that item does not exist or does not pertain to the concept. If the entry is other than "0" or "1," the number of units is specified. A "-1" entered into this column indicates a fractional unit is required, but usually its cost is taken into account at a higher level. Last, Table F-III presents a detailed cost breakdown upon which Table III-III in Sec. III.D.2 is based.

TABLE F-I

SUMMARY OF GUIDELINES USED IN COMMON COSTING PROCEDURE^{41,42}

- Although a maximum, practical plant size of 5000 MWe is established, the actual plant size and associated number of units per power plant is established on the basis of specific cost optimization. In this context, approximately 8 FLR units were selected to give a net electrical output of ~1000 MWe, primarily because of turbine and steam-generator costs.
- The costing of design and engineering activities assumes the existence of a mature industry for all major reactor and balance-of-plant components.
- All labor, materials, equipment-during-construction, plant startup, and plant operating costs are based on January 1, 1978 dollar values.
- The costing methodology is based upon similar schemes used by investor-owned (private) utilities rather than for a public utility project.
- The capital cost accounts are given in Table F-II and are composed of direct, indirect, and time-related costs.
 - Direct costs are determined by the best estimates of component costs on the basis of a detailed, well-documented conceptual design.
 - Indirect costs are determined as a percentage of the direct costs: 15% for construction facilities, equipment, and services; 5% for taxes, insurance, and plant startup; 15% for engineering and management.
 - Time-related costs are composed of only interest during construction. Although numerous methods exist for computing the time-related costs,⁵⁰ the particular method selected here applies for an integrated cash flow that is skewed towards the back end of the construction period, leading to a half-cash-flow at 60% of the construction period. Hence, escalation and interest are computed as a percentage of the direct plus indirect costs assuming a 10-yr construction period; aggregate percentages of 33.8% and 64.4%, respectively, result for an escalation rate of 5% and an interest ratio of 10%.
- Operating and maintenance costs reflect the daily, routine expenditures incurred during plant operation and are specified in detail by Ref. 41. Nuclear liability insurance, licenses and fees, and working capital are not included. Generally, operating and maintenance costs equal 2% of the total capital (direct plus indirect plus interest during construction). If an exceptional operating and maintenance cost is incurred, such as the leads and liner cost for the FLR, this cost is computed by a separate optimization procedure (Appendix C) and added to the "normal" operating maintenance costs.

The following assumptions are used to compute the power costs (mills/kWeh)

- plant power factor is 0.85

TABLE F-I cont'd.

- plant operating life is 30 yr
- cost of debt is 10% per year
- cost of equity is 15% per year
- escalation is 5% per year

TABLE F-II

COST DATA BASE

DESIGNATION: FAST LINER REACTOR LY

DATE: 78/10/11.

ACC. NO.	ACCOUNT TITLE	UNIT COST	NO. OF UNITS	REFERENCE
20. 1. 0. 0	LAND & PRIVILEGE ACQUISITION	0.	.1000E+01	
20. 2. 0. 0	RELOCATION OF BUILDINGS, UTILITIES, HIGHWAYS, ETC.	0.	.1000E+01	
20. 0. 0. 0	LAND & LAND RIGHTS	.2500E+04 \$/ACRE	.1000E+04	1
21. 1. 1. 0	GENERAL YARD IMPROVEMENTS	0.	.1000E+01	
21. 1. 2. 0	WATERFRONT IMPROVEMENTS	0.	.1000E+01	
21. 1. 3. 0	TRANSPORTATION ACCESS (OFF SITE)	0.	.1000E+01	
21. 1. 0. 0	SITE IMPROVEMENTS & FACILITIES	.1100E+08 \$.1000E+01	2
21. 2. 1. 0	BASIC BUILDING STRUCTURES	.8200E+03 \$/M3	.1257E+05	3, 4, 5
21. 2. 2. 0	BUILDING SERVICES	.8000E+02 \$/M3	.1257E+05	3, 4, 5
21. 2. 3. 0	CONTAINMENT STRUCTURES	0.	.1000E+01	
21. 2. 4. 0	REACTOR BUILDING	0.	.1000E+01	
21. 3. 1. 0	BASIC BUILDING STRUCTURES	.1010E+03 \$/M3	.1600E+06	6, 7
21. 3. 2. 0	BUILDING SERVICES	.9000E+01 \$/M3	.1600E+06	6, 7
21. 3. 0. 0	TURBINE BUILDING	0.	.1000E+01	
21. 4. 1. 0	INTAKE STRUCTURES	0.	.1000E+01	
21. 4. 2. 0	DISCHARGE STRUCTURES	0.	.1000E+01	
21. 4. 3. 0	UNPRESSURIZED INTAKE & DISCHARGE CONDUITS	0.	.1000E+01	
21. 4. 4. 0	RECIRCULATING STRUCTURES	0.	.1000E+01	
21. 4. 5. 0	COOLING TOWER SYSTEMS	0.	.1000E+01	
21. 4. 0. 0	COOLING SYSTEM STRUCTURES	.3500E+04 \$/MWTM	.3400E+04	2
21. 5. 1. 0	BASIC BUILDING STRUCTURES	.4500E+03 \$/M3	.1257E+05	3
21. 5. 2. 0	BUILDING SERVICES	.5000E+02 \$/M3	.1257E+05	3
21. 5. 0. 0	POWER SUPPLY & ENERGY STORAGE BUILDING	0.	.1000E+01	
21. 6. 1. 0	REACTOR AUXILIARIES BUILDING (INCL. SWITCHGEAR BAY)	.5000E+03 \$/M3	.1250E+06	3
21. 6. 2. 0	RADIOACTIVE WASTE BUILDING	.5000E+03 \$/M3	.1500E+05	3
21. 6. 3. 0	FUEL STORAGE BUILDING	0.	.1000E+01	
21. 6. 4. 0	CONTROL ROOM BUILDING	.3750E+03 \$/M3	.8500E+04	7
21. 6. 5. 0	DIESEL GENERATOR BUILDING	.3750E+03 \$/M3	.3800E+04	7
21. 6. 6. 0	ADMINISTRATION BUILDING	.2500E+03 \$/M3	.8500E+04	7
21. 6. 7. 0	SERVICE BUILDING	.2500E+03 \$/M3	.1000E+05	7
21. 6. 8. 0	HELIUM STORAGE BUILDING	.1100E+03 \$/M3	.4000E+04	3
21. 6. 9. 0	MISCELLANEOUS STRUCTURES & BUILDING WORK	.7500E+07 \$.1000E+01	3
21. 6. 0. 0	MISCELLANEOUS BUILDINGS	0.	.1000E+01	
21. 7. 0. 0	VENTILATION STACK	.8000E+06 \$.1000E+01	3
21. 98. 0. 0	SPARE PARTS ALLOWANCE	0.	.1000E+01	
21. 99. 0. 0	CONTINGENCY ALLOWANCE	.1500E+00 FRACTION	-.1000E+01	
21. 0. 0. 0	STRUCTURES & SITE FACILITIES	0.	.1000E+01	
22. 1. 1. 1	BREEDING MATERIAL (INCL. TRITIUM BREEDING)	.3900E+05 \$/M3	0.	8
22. 1. 1. 2	FIRST WALL & STRUCTURAL MATERIAL	.1181E+06 \$/M3	.2283E+03	9
22. 1. 1. 3	ATTENUATORS, REFLECTORS, & MULTIPLIERS	.9000E+03 \$/M3	0.	8
22. 1. 1. 4	WALL MODIFIERS (COATINGS, LINERS, LIMITERS, ETC.)	0.	0.	
22. 1. 1. 5	OTHERS	0.	.1000E+01	
22. 1. 1. 0	BLANKET & FIRST WALL	0.	.1000E+01	
22. 1. 2. 1	PRIMARY	.1120E+05 \$/M3	0.	8
22. 1. 2. 2	SECONDARY	0.	0.	
22. 1. 2. 0	SHIELD	0.	.1000E+01	
22. 1. 3. 1	PRINCIPAL FIELD MAGNET	.1000E+06 \$/M3	0.	4, 8
22. 1. 3. 2	SECONDARY FIELD MAGNET	.1000E+06 \$/M3	0.	4, 8
22. 1. 3. 0	MAGNETS	0.	.1000E+01	
22. 1. 4. 1	BEAM HEATING (NEUTRAL, ION OR ELECTRON)	0.	.1000E+01	
22. 1. 4. 2	RF HEATING	0.	.1000E+01	
22. 1. 4. 3	LASER HEATING	0.	.1000E+01	
22. 1. 4. 4	OTHER HEATING SYSTEMS	0.	.1000E+01	

22	1	4	0	SUPPLEMENTAL HEATING SYSTEMS	0.	0.	
22	1	5	1	REACTOR STRUCTURE	0.	0.	
22	1	5	2	EQUIPMENT SUPPORT STRUCTURE	0.	1000E+01	
22	1	5	0	PRIMARY STRUCTURE & SUPPORT	0.	2283E+03	
22	1	6	1	PLASMA CHAMBER VACUUM(INCL. PUMPS/COMP./PIPE)	.1250E+06	1000E+01	
22	1	6	2	MAGNET DEWAR VACUUM(INCL. PUMPS/COMP./PIPE)	0.	1000E+01	
22	1	6	3	SUPPLEMENTAL HEATING VACUUM(INCL. PUMPS/COMP./PIPE)	0.	1000E+01	
22	1	6	4	DIRECT CONVERTOR VACUUM(INCL. PUMPS/COMP./PIPE)	0.	1000E+01	
22	1	6	5	REACTOR VACUUM SYSTEM(LOW GRADE)	0.	1000E+01	
22	1	6	6	REACTOR VACUUM WALL	0.	1000E+01	
22	1	6	0	REACTOR VACUUM SYSTEMS(UNLESS INTEGRAL ELSEWHERE)	.3300E+05 \$/M3	.2011E+01	8
22	1	7	1	HEATING	.2500E+00 \$/J	.3930E+09	
22	1	7	2	CONFINEMENT	.1000E-01 \$/J	.3930E+09	4,10,11
22	1	7	3	CONTROL SYSTEM	0.	0.	
22	1	7	4	CENTRAL ENERGY STORAGE	0.	0.	
22	1	7	5	OTHER	.1000E+00 \$/J	0.	
22	1	7	0	POWER SUPPLY, SWITCHING & ENERGY STORAGE	0.	.1000E+01	
22	1	8	0	IMPURITY CONTROL	0.	.1000E+01	
22	1	9	1	VACUUM TANK	0.	.1000E+01	
22	1	9	2	DIRECT CONVERTOR MODULES	0.	.1000E+01	
22	1	9	3	THERMAL PANELS	0.	.1000E+01	
22	1	9	4	POWER CONDITIONING EQUIPMENT	0.	.1000E+01	
22	1	9	0	DIRECT ENERGY CONVERSION SYSTEM	0.	0.	
22	1	0	0	REACTOR EQUIPMENT	0.	.1000E+01	
22	2	1	1	PUMPS & MOTOR DRIVES(MODULAR & NONMODULAR)	0.	.1000E+01	
22	2	1	2	PIPING	0.	.1000E+01	
22	2	1	3	HEAT EXCHANGERS	0.	.1000E+01	
22	2	1	4	TANKS(INCL. DUMP,MAKE-UP,CLEAN-UP,TRIT.,HOT STORAGE)	0.	.1000E+01	
22	2	1	5	CLEAN-UP SYSTEM	0.	.1000E+01	
22	2	1	6	THERMAL INSULATION, PIPING & EQUIPMENT	0.	.1000E+01	
22	2	1	7	TRITIUM EXTRACTION	0.	.1000E+01	
22	2	1	0	PRIMARY COOLANT SYSTEM	.3370E+05 \$/MWTM	.3400E+04	2
22	2	2	1	PUMPS & MOTOR DRIVES(MODULAR & NONMODULAR)	0.	.1000E+01	
22	2	2	2	PIPING	0.	.1000E+01	
22	2	2	3	HEAT EXCHANGERS	0.	.1000E+01	
22	2	2	4	TANKS(INCL. DUMP,MAKE-UP,CLEAN-UP,TRIT.,HOT STORAGE)	0.	.1000E+01	
22	2	2	5	CLEAN-UP SYSTEM	0.	.1000E+01	
22	2	2	6	THERMAL INSULATION, PIPING & EQUIPMENT	0.	.1000E+01	
22	2	2	7	TRITIUM EXTRACTION	0.	.1000E+01	
22	2	2	0	INTERMEDIATE COOLANT SYSTEM	.2800E+05 \$/MWTM	.3400E+04	2
22	2	0	0	MAIN HEAT TRANSFER & TRANSPORT SYSTEMS	0.	.1000E+01	
22	3	1	1	REFRIGERATION	0.	.1000E+01	
22	3	1	2	PIPING	0.	.1000E+01	
22	3	1	3	FLUID CIRCULATION DRIVING SYSTEM	0.	.1000E+01	
22	3	1	4	TANKS	0.	.1000E+01	
22	3	1	5	PURIFICATION	0.	.1000E+01	
22	3	1	0	MAGNET COOLING SYSTEM	0.	.1000E+01	
22	3	2	1	REFRIGERATION	0.	.1000E+01	
22	3	2	2	PIPING	0.	.1000E+01	
22	3	2	3	FLUID CIRCULATION DRIVING SYSTEM	0.	.1000E+01	
22	3	2	4	TANKS	0.	.1000E+01	
22	3	2	5	PURIFICATION	0.	.1000E+01	
22	3	3	0	SHIELD & STRUCTURE COOLING SYSTEM	0.	.1000E+01	
22	3	3	1	REFRIGERATION	0.	.1000E+01	
22	3	3	2	PIPING	0.	.1000E+01	
22	3	3	3	FLUID CIRCULATION DRIVING SYSTEM	0.	.1000E+01	
22	3	3	4	TANKS	0.	.1000E+01	
22	3	3	5	PURIFICATION	0.	.1000E+01	
22	3	3	0	SUPPLEMENTAL HEATING SYSTEM COOLING SYSTEM	0.	.1000E+01	
22	3	4	1	REFRIGERATION	0.	.1000E+01	

22.3.4.2	PIPING	0.	.1000E+01	
22.3.4.4	FLUID CIRCULATION DRIVING SYSTEM	0.	.1000E+01	
22.3.4.4	TANKS	0.	.1000E+01	
22.3.4.4	PURIFICATION	0.	.1000E+01	
22.3.4.5	POWER SUPPLY COOLING SYSTEM	0.	.1000E+01	
22.3.4.5	OTHER COOLING SYSTEMS	0.	.1000E+01	
22.3.0.0	AUXILIARY COOLING SYSTEMS	0.	.1000E+01	
22.4.1.0	LIQUID WASTE PROCESSING & EQUIPMENT	.6700E+03 \$/MWTB	.3400E+04	2
22.4.2.0	GASEOUS WASTES & OFF-GAS PROCESSING SYSTEM	0.	.1000E+01	
22.4.3.0	SOLID WASTE PROCESSING EQUIPMENT	0.	.1000E+01	
22.4.4.0	RADIOACTIVE WASTE TREATMENT & DISPOSAL	.2300E+04 \$/MWTB	.3400E+04	3
22.5.1.0	FUEL PURIFICATION SYSTEMS	0.	.1000E+01	
22.5.2.0	LIQUEFACTION	0.	.1000E+01	
22.5.3.0	FUEL PREPARATION	0.	.1000E+01	
22.5.4.0	FUEL INJECTION	0.	.1000E+01	
22.5.5.0	FUEL STORAGE	0.	.1000E+01	
22.5.6.0	TRITIUM RECOVERY	0.	.1000E+01	
22.5.0.0	EMERGENCY AIR DETRITIATION	0.	.1000E+01	
22.6.0.0	FUEL HANDLING & STORAGE SYSTEMS(FUEL INJECTION)	.3600E+03 \$/MWTB	.3400E+04	3
22.6.1.1	BLANKET & COIL MAINTENANCE EQUIPMENT	0.	.1000E+01	
22.6.1.2	COMPONENTS ROTATED INTO SERVICE TO ALLOW MAINT.	0.	.1000E+01	
22.6.1.3	OTHER MAINTENANCE EQUIPMENT	0.	.1000E+01	
22.6.1.0	MAINTENANCE EQUIPMENT	0.	.1000E+01	
22.6.2.0	SPECIAL HEATING SYSTEMS(START-UP TRACE, ETC.)	0.	.1000E+01	
22.6.3.0	COOLANT RECEIVING, STORAGE & MAKE-UP SYSTEMS	0.	.1000E+01	
22.6.4.0	GAS SYSTEMS	0.	.1000E+01	
22.6.5.0	BUILDING VACUUM SYSTEMS	0.	.1000E+01	
22.6.0.0	OTHER REACTOR PLANT EQUIPMENT	.3650E+04 \$/MWTB	.3400E+04	2
22.7.1.0	REACTOR I&C EQUIPMENT(BURN CONTROL, DIAGNOSTICS, ETC.)	0.	.1000E+01	
22.7.2.0	RADIATION MONITORING SYSTEMS	0.	.1000E+01	
22.7.3.0	ISOLATED INDICATING & RECORDING GAUGES, ETC.	0.	.1000E+01	
22.7.0.0	INSTRUMENTATION & CONTROL(I&C)	.1600E+08 \$.1000E+01	2
22.98.0.0	SPARE PARTS ALLOWANCE	.5000E-01 FRACTION	-.1000E+01	
22.99.0.0	CONTINGENCY ALLOWANCE	.1500E+00 FRACTION	-.1000E+01	
23.0.0.0	REACTOR PLANT EQUIPMENT	0.	.1000E+01	
23.1.1.0	TURBINE-GENERATORS & ACCESSORIES	0.	.1000E+01	
23.1.2.0	FOUNDATIONS	0.	.1000E+01	
23.1.3.0	STANDBY EXCITERS	0.	.1000E+01	
23.1.4.0	LUBRICATING SYSTEM	0.	.1000E+01	
23.1.5.0	GAS SYSTEMS	0.	.1000E+01	
23.1.6.0	REHEATERS	0.	.1000E+01	
23.1.7.0	SHIELDING	0.	.1000E+01	
23.1.8.0	WEATHER-PROOF HOUSING	0.	.1000E+01	
23.1.0.0	TURBINE-GENERATORS	.1790E+05 \$/MWTB	.3400E+04	2
23.2.0.0	MAIN STEAM (OR OTHER FLUID) SYSTEM	0.	.1000E+01	
23.3.1.0	WATER INTAKE COMMON FACILITIES	0.	.1000E+01	
23.3.2.0	CIRCULATING WATER SYSTEMS	0.	.1000E+01	
23.3.3.0	COOLING TOWERS	0.	.1000E+01	
23.3.4.0	OTHER SYSTEMS WHICH REJECT HEAT TO THE ATMOSPHERE	0.	.1000E+01	
23.3.0.0	HEAT REJECTION SYSTEMS	.3730E+04 \$/MWTB	.3400E+04	2
23.4.1.0	CONDENSERS	0.	.1000E+01	
23.4.2.0	CONDENSATE SYSTEM	0.	.1000E+01	
23.4.3.0	GAS REMOVAL SYSTEM	0.	.1000E+01	
23.4.4.0	TURBINE BY-PASS SYSTEMS(EXCL. PIPING)	0.	.1000E+01	
23.4.0.0	CONDENSING SYSTEMS	.2060E+04 \$/MWTB	.3400E+04	2
23.5.1.0	REGENERATORS & RECUPORATORS	0.	.1000E+01	
23.5.2.0	PUMPS	0.	.1000E+01	
23.5.3.0	TANKS	0.	.1000E+01	
23.5.0.0	FEED HEATING SYSTEM	.3060E+04 \$/MWTB	.3400E+04	2
23.6.1.0	TURBINE AUXILIARIES	0.	.1000E+01	

23.	6.	2.	0	AUXILIARIES COOLING SYSTEM(EXCL. PIPING)	0.					
23.	6.	3.	0	MAKE-UP TREATMENT SYSTEM(EXCL. PIPING)	0.			.1000E+01		
23.	6.	4.	0	CHEMICAL TREATMENT & CONDENSATE PURIFICATION SYSTEMS	0.			.1000E+01		
23.	6.	5.	0	CENTRAL LUBRICATION SERVICE SYSTEM(EXCL. PIPING)	0.			.1000E+01		
23.	6.	0.	0	OTHER TURBINE PLANT EQUIPMENT	0.			.1000E+01		
23.	7.	0.	0	INSTRUMENTATION & CONTROL(I&C) EQUIPMENT	.1880E+05	\$/MWTB		.3400E+04		
23.	99.	0.	0	SPARE PARTS ALLOWANCE	.5800E+03	\$/MWTB		.3400E+04		2
23.	99.	0.	0	CONTINGENCY ALLOWANCE	.1000E-02	FRACTION		.1000E+01		2
23.	0.	0.	0	TURBINE PLANT EQUIPMENT	0.			.1000E+01		
24.	1.	1.	0	GENERATOR CIRCUITS	0.			.1000E+01		
24.	1.	2.	0	STATION SERVICE	0.			.1000E+01		
24.	1.	0.	0	SWITCHGEAR	0.			.1000E+01		
24.	2.	1.	0	STATION SERVICE & STARTUP TRANSFORMERS	.3500E+04	\$/MWEQ		.1360E+04		2
24.	2.	2.	0	LOW VOLTAGE UNIT SUBSTATION & LIGHTING TRANSFORMERS	0.			.1000E+01		
24.	2.	3.	0	BATTERY SYSTEM	0.			.1000E+01		
24.	2.	4.	0	DIESEL ENGINE GENERATORS	0.			.1000E+01		
24.	2.	5.	0	GAS TURBINE GENERATORS	0.			.1000E+01		
24.	2.	6.	0	MOTOR GENERATOR SETS	0.			.1000E+01		
24.	2.	0.	0	STATION SERVICE EQUIPMENT	0.			.1000E+01		
24.	3.	1.	0	MAIN CONTROL BOARD FOR ELECTRIC SYSTEM	.6900E+04	\$/MWEQ		.1360E+04		2
24.	3.	2.	0	AUXILIARY POWER & SIGNAL BOARDS	0.			.1000E+01		
24.	3.	0.	0	SWITCHBOARDS (INCL. HEAT TRACING)	0.			.1000E+01		
24.	4.	1.	0	GEN. STATION GROUNDING SYSTEM & CATHODIC PROTECTION	.2300E+04	\$/MWEQ		.1360E+04		2
24.	5.	1.	0	PROTECTIVE EQUIPMENT	0.			.1000E+01		
24.	5.	1.	0	CONCRETE CABLE TUNNELS, TRENCHES & ENVELOPES	.8000E+02	\$/MWEQ		.1360E+04		2
24.	5.	2.	0	CABLE TRAYS & SUPPORT	0.			.1000E+01		
24.	5.	3.	0	CONDUIT	0.			.1000E+01		
24.	5.	4.	0	OTHER STRUCTURES	0.			.1000E+01		
24.	5.	0.	0	ELECTRICAL STRUCTURES & WIRING CONTAINERS	0.			.1000E+01		
24.	6.	1.	0	GENERATOR CIRCUITS WIRING	.9300E+03	\$/MWEQ		.1360E+04		2
24.	6.	2.	0	STATION SERVICE POWER WIRING	0.			.1000E+01		
24.	6.	3.	0	CONTROL WIRING	0.			.1000E+01		
24.	6.	4.	0	INSTRUMENT WIRING	0.			.1000E+01		
24.	6.	5.	0	CONTAINMENT PENETRATIONS	0.			.1000E+01		
24.	6.	0.	0	POWER & CONTROL WIRING	.6960E+04	\$/MWEQ		.1360E+04		2
24.	7.	1.	0	REACTOR BUILDING LIGHTING	0.			.1360E+04		
24.	7.	2.	0	TURBINE BUILDING LIGHTING	0.			.1000E+01		
24.	7.	3.	0	REACTOR AUXILIARIES BUILDING LIGHTING	0.			.1000E+01		
24.	7.	4.	0	RADIOACTIVE WASTE BUILDING LIGHTING	0.			.1000E+01		
24.	7.	5.	0	FUEL STORAGE BUILDING LIGHTING	0.			.1000E+01		
24.	7.	6.	0	MISCELLANEOUS BUILDINGS LIGHTING	0.			.1000E+01		
24.	7.	7.	0	YARD LIGHTING	0.			.1000E+01		
24.	7.	0.	0	ELECTRICAL LIGHTING	0.			.1000E+01		
24.	99.	0.	0	SPARE PARTS ALLOWANCE	.4200E+05	\$/MWEQ		.1360E+04		2
24.	99.	0.	0	CONTINGENCY ALLOWANCE	0.		FRACTION	.1000E+01		2
24.	0.	0.	0	ELECTRIC PLANT EQUIPMENT	0.		FRACTION	.1000E+01		2
25.	1.	1.	0	CRANES, HOISTS, MONORAILS, & CONVEYORS	0.			.1000E+01		
25.	1.	2.	0	RAILWAY	0.			.1000E+01		
25.	1.	3.	0	ROADWAY EQUIPMENT	0.			.1000E+01		
25.	1.	4.	0	WATERCRAFT	0.			.1000E+01		
25.	1.	5.	0	VEHICLE MAINTENANCE EQUIPMENT	0.			.1000E+01		
25.	3.	1.	0	TRANSPORTATION & LIFTING EQUIPMENT	.4150E+07	\$.1000E+01		2
25.	3.	1.	0	AIR SYSTEMS(EXCL. PIPING)	0.			.1000E+01		
25.	3.	2.	0	WATER SYSTEMS(EXCL. PIPING)	0.			.1000E+01		
25.	3.	3.	0	AUXILIARY HEATING BOILERS(EXCL. PIPING)	0.			.1000E+01		
25.	3.	0.	0	AIR & WATER SERVICE SYSTEMS	0.			.1000E+01		
25.	3.	1.	0	LOCAL COMMUNICATIONS SYSTEMS	.7700E+07	\$.1000E+01		2
25.	3.	2.	0	SIGNAL SYSTEMS	0.			.1000E+01		
25.	3.	0.	0	COMMUNICATIONS EQUIPMENT	0.			.1000E+01		
25.	4.	1.	0	SAFETY EQUIPMENT	.3000E+06	\$.1000E+01		2

25. 4. 2. 0	SHOP, LABORATORY, & TEST EQUIPMENT	0.	.1000E+01	
25. 4. 3. 0	OFFICE EQUIPMENT & FURNISHINGS	0.	.1000E+01	
25. 4. 4. 0	CHANGE ROOM EQUIPMENT	0.	.1000E+01	
25. 4. 5. 0	ENVIRONMENTAL MONITORING EQUIPMENT	0.	.1000E+01	
25. 4. 6. 0	DINING FACILITIES	0.	.1000E+01	
25. 4. 0. 0	FURNISHINGS & FIXTURES	.6530E+06 \$.1000E+01	2
25. 98. 0. 0	SPARE PARTS ALLOWANCE	.5000E-01 FRACTION	-.1000E+01	
25. 99. 0. 0	CONTINGENCY ALLOWANCE	.1500E+00 FRACTION	-.1000E+01	
25. 0. 0. 0	MISCELLANEOUS PLANT EQUIPMENT	0.	.1000E+01	
26. 1. 0. 0	REACTOR COOLANT	.4960E+04 \$/MWH	.3400E+04	2
26. 2. 0. 0	INTERMEDIATE COOLANT	.2860E+04 \$/MWH	.3400E+04	2
26. 3. 0. 0	TURBINE CYCLE WORKING FLUIDS	0.	.1000E+01	
26. 4. 0. 0	OTHER MATERIALS	.4330E+03 \$/MWH	.3400E+04	2
26. 98. 0. 0	SPARE PARTS ALLOWANCE	0.	-.1000E+01	
26. 99. 0. 0	CONTINGENCY ALLOWANCE	0.	-.1000E+01	
26. 0. 0. 0	SPECIAL MATERIALS	0.	.1000E+01	
90. 0. 0. 0	TOTAL REACTOR DIRECT CAPITAL COST	0.	-.1000E+01	1
91. 1. 0. 0	TEMPORARY FACILITIES	0.	.1000E+01	1
91. 2. 0. 0	CONSTRUCTION EQUIPMENT	0.	-.1000E+01	1
91. 3. 0. 0	CONSTRUCTION SERVICES	0.	-.1000E+01	1
91. 0. 0. 0	CONSTRUCTION FACILITIES EQUIPMENT & SERVICES (15%)	.1500E+00 FRACTION	-.1000E+01	1
92. 0. 0. 0	ENGINEERING & CONSTRUCTION MANAGEMENT SERVICES (15%)	.1500E+00 FRACTION	-.1000E+01	1
93. 1. 0. 0	TAXES & INSURANCE	0.	-.1000E+01	1
93. 2. 0. 0	STAFF TRAINING & PLANT STARTUP	0.	-.1000E+01	1
93. 3. 0. 0	OWNER'S G&A	0.	-.1000E+01	1
93. 0. 0. 0	OTHER COSTS (5%)	.5000E-01 FRACTION	-.1000E+01	1
94. 0. 0. 0	INTEREST DURING 10 YEAR CONSTRUCTION (10% /YR. = 64.4%)	.6440E+00 FRACTION	-.1000E+01	1
95. 0. 0. 0	ESCALATION DURING 10 YEAR CONSTRUCTION (5% /YR. = 33.8%)	.3380E+00 FRACTION	-.1000E+01	1
99. 0. 0. 0	TOTAL REACTOR CAPITAL COST	0.	.1016E+04	1

1ER
1EF

TABLE F-III

FUSION REACTOR ECONOMIC EVALUATION

DESIGNATION: FAST LINER REACTOR LY		DATE: 78/10/11.	
ACC. NO.	ACCOUNT TITLE	MILLION DOLLARS	
20. 1.	LAND & PRIVILEGE ACQUISITION		
20. 2.	RELOCATION OF BUILDINGS, UTILITIES, HIGHWAYS, ETC.		
20.	LAND & LAND RIGHTS		2.500
21. 1. 1.	GENERAL YARD IMPROVEMENTS		
21. 1. 2.	WATERFRONT IMPROVEMENTS		
21. 1. 3.	TRANSPORTATION ACCESS (OFF SITE)		
21. 1.	SITE IMPROVEMENTS & FACILITIES	11.000	
21. 2. 1.	BASIC BUILDING STRUCTURES		
21. 2. 2.	BUILDING SERVICES	10.307	
21. 2. 3.	CONTAINMENT STRUCTURES	1.006	
21. 2.	REACTOR BUILDING		11.313
21. 3. 1.	BASIC BUILDING STRUCTURES		
21. 3. 2.	BUILDING SERVICES	16.160	
21. 3.	TURBINE BUILDING	1.440	
21. 3.			17.600
21. 4. 1.	INTAKE STRUCTURES		
21. 4. 2.	DISCHARGE STRUCTURES		
21. 4. 3.	UNPRESSURIZED INTAKE & DISCHARGE CONDUITS		
21. 4. 4.	RECIRCULATING STRUCTURES		
21. 4. 5.	COOLING TOWER SYSTEMS		
21. 4.	COOLING SYSTEM STRUCTURES		11.900
21. 5. 1.	BASIC BUILDING STRUCTURES		
21. 5. 2.	BUILDING SERVICES	5.657	
21. 5.	POWER SUPPLY & ENERGY STORAGE BUILDING	.629	
21. 5.			6.285
21. 6. 1.	REACTOR AUXILIARIES BUILDING (INCL. SWITCHGEAR BAY)	62.500	
21. 6. 2.	RADIOACTIVE WASTE BUILDING	7.500	
21. 6. 3.	FUEL STORAGE BUILDING		
21. 6. 4.	CONTROL ROOM BUILDING		
21. 6. 5.	DIESEL GENERATOR BUILDING	3.188	
21. 6. 6.	ADMINISTRATION BUILDING	1.425	
21. 6. 7.	SERVICE BUILDING	2.125	
21. 6. 8.	HELIUM STORAGE BUILDING	2.500	
21. 6. 9.	MISCELLANEOUS STRUCTURES & BUILDING WORK	.440	
21. 6.	MISCELLANEOUS BUILDINGS	7.500	
21. 6.			87.178
21. 7.	VENTILATION STACK		.800
21.98.	SPARE PARTS ALLOWANCE		
21.99.	CONTINGENCY ALLOWANCE		
21.99.		21.911	
21.	STRUCTURES & SITE FACILITIES		167.987

22.	1.	1.	1	BREEDING MATERIAL(INCL. TRITIUM BREEDING)	0.000	
22.	1.	1.	2	FIRST WALL & STRUCTURAL MATERIAL	26.962	
22.	1.	1.	3	ATTENUATORS, REFLECTORS, & MULTIPLIERS	0.000	
22.	1.	1.	4	WALL MODIFIERS(COATINGS, LINERS, LIMITERS, ETC.)	0.000	
22.	1.	1.	5.	OTHERS		
22.	1.	2.	1	BLANKET & FIRST WALL		26.962
22.	1.	2.	2	PRIMARY	0.000	
22.	1.	2.	2	SECONDARY	0.000	
22.	1.	2.		SHIELD		
22.	1.	3.	1	PRINCIPAL FIELD MAGNET	0.000	
22.	1.	3.	2	SECONDARY FIELD MAGNET	0.000	
22.	1.	3.		MAGNETS		
22.	1.	4.	1.	BEAM HEATING(NEUTRAL, ION OR ELECTRON)		
22.	1.	4.	2.	RF HEATING		
22.	1.	4.	3.	LASER HEATING		
22.	1.	4.	4.	OTHER HEATING SYSTEMS		
22.	1.	4.		SUPPLEMENTAL HEATING SYSTEMS		0.000
22.	1.	5.	1	REACTOR STRUCTURE	0.000	
22.	1.	5.	2.	EQUIPMENT SUPPORT STRUCTURE		
22.	1.	5.		PRIMARY STRUCTURE & SUPPORT		28.538
22.	1.	6.	1.	PLASMA CHAMBER VACUUM(INCL. PUMPS/COMP./PIPE)		
22.	1.	6.	2.	MAGNET DEWAR VACUUM(INCL. PUMPS/COMP./PIPE)		
22.	1.	6.	3.	SUPPLEMENTAL HEATING VACUUM(INCL. PUMPS/COMP./PIPE)		
22.	1.	6.	4.	DIRECT CONVERTOR VACUUM(INCL. PUMPS/COMP./PIPE)		
22.	1.	6.	5.	REACTOR VACUUM SYSTEM(LOW GRADE)		
22.	1.	6.	6.	REACTOR VACUUM WALL		
22.	1.	6.		REACTOR VACUUM SYSTEMS(UNLESS INTEGRAL ELSEWHERE)		.066
22.	1.	7.	1	HEATING	98.250	
22.	1.	7.	2	CONFINEMENT	3.930	
22.	1.	7.	3	CONTROL SYSTEM	0.000	
22.	1.	7.	4	CENTRAL ENERGY STORAGE	0.000	
22.	1.	7.	5	OTHER	0.000	
22.	1.	7.		POWER SUPPLY, SWITCHING & ENERGY STORAGE		102.180
22.	1.	8.		IMPURITY CONTROL		
22.	1.	9.	1.	VACUUM TANK		
22.	1.	9.	2.	DIRECT CONVERTOR MODULES		
22.	1.	9.	3.	THERMAL PANELS		
22.	1.	9.	4.	POWER CONDITIONING EQUIPMENT		
22.	1.	9.		DIRECT ENERGY CONVERSION SYSTEM		0.000
22.	1.			REACTOR EQUIPMENT		157.746
22.	2.	1.	1.	PUMPS & MOTOR DRIVES(MODULAR & NONMODULAR)		
22.	2.	1.	2.	PIPING		
22.	2.	1.	3.	HEAT EXCHANGERS		
22.	2.	1.	4.	TANKS(INCL. DUMP, MAKE-UP, CLEAN-UP, TRIT., HOT STORAGE)		
22.	2.	1.	5.	CLEAN-UP SYSTEM		
22.	2.	1.	6.	THERMAL INSULATION, PIPING & EQUIPMENT		
22.	2.	1.	7.	TRITIUM EXTRACTION		
22.	2.	1.		PRIMARY COOLANT SYSTEM		114.580
22.	2.	2.	1.	PUMPS & MOTOR DRIVES(MODULAR & NONMODULAR)		
22.	2.	2.	2.	PIPING		
22.	2.	2.	3.	HEAT EXCHANGERS		
22.	2.	2.	4.	TANKS(INCL. DUMP, MAKE-UP, CLEAN-UP, TRIT., HOT STORAGE)		
22.	2.	2.	5.	CLEAN-UP SYSTEM		
22.	2.	2.	6.	THERMAL INSULATION, PIPING & EQUIPMENT		
22.	2.	2.	7.	TRITIUM EXTRACTION		
22.	2.	2.		INTERMEDIATE COOLANT SYSTEM	95.200	
22.	2.	2.		MAIN HEAT TRANSFER & TRANSPORT SYSTEMS		209.780

22.	3.	1.	1.	REFRIGERATION	
22.	3.	1.	2.	PIPING	
22.	3.	1.	3.	FLUID CIRCULATION DRIVING SYSTEM	
22.	3.	1.	4.	TANKS	
22.	3.	1.	5.	PURIFICATION	
22.	3.	2.	1.	MAGNET COOLING SYSTEM	
22.	3.	2.	2.	REFRIGERATION	
22.	3.	2.	3.	PIPING	
22.	3.	2.	4.	FLUID CIRCULATION DRIVING SYSTEM	
22.	3.	2.	5.	TANKS	
22.	3.	2.	6.	PURIFICATION	
22.	3.	3.	1.	SHIELD & STRUCTURE COOLING SYSTEM	
22.	3.	3.	2.	REFRIGERATION	
22.	3.	3.	3.	PIPING	
22.	3.	3.	4.	FLUID CIRCULATION DRIVING SYSTEM	
22.	3.	3.	5.	TANKS	
22.	3.	3.	6.	PURIFICATION	
22.	3.	3.	7.	SUPPLEMENTAL HEATING SYSTEM COOLING SYSTEM	
22.	3.	4.	1.	REFRIGERATION	
22.	3.	4.	2.	PIPING	
22.	3.	4.	3.	FLUID CIRCULATION DRIVING SYSTEM	
22.	3.	4.	4.	TANKS	
22.	3.	4.	5.	PURIFICATION	
22.	3.	4.	6.	POWER SUPPLY COOLING SYSTEM	
22.	3.	5.	1.	OTHER COOLING SYSTEMS	
22.	3.	5.	2.	AUXILIARY COOLING SYSTEMS	2.278
22.	4.	1.	1.	LIQUID WASTE PROCESSING & EQUIPMENT	
22.	4.	2.	1.	GASEOUS WASTES & OFF-GAS PROCESSING SYSTEM	
22.	4.	3.	1.	SOLID WASTE PROCESSING EQUIPMENT	
22.	4.	3.	2.	RADIOACTIVE WASTE TREATMENT & DISPOSAL	7.820
22.	5.	1.	1.	FUEL PURIFICATION SYSTEMS	
22.	5.	2.	1.	LIQUEFACTION	
22.	5.	3.	1.	FUEL PREPARATION	
22.	5.	4.	1.	FUEL INJECTION	
22.	5.	5.	1.	FUEL STORAGE	
22.	5.	6.	1.	TRITIUM RECOVERY	
22.	5.	7.	1.	EMERGENCY AIR DETRITIATION	
22.	5.	7.	2.	FUEL HANDLING & STORAGE SYSTEMS(FUEL INJECTION)	1.224
22.	6.	1.	1.	BLANKET & COIL MAINTENANCE EQUIPMENT	
22.	6.	1.	2.	COMPONENTS ROTATED INTO SERVICE TO ALLOW MAINT.	
22.	6.	1.	3.	OTHER MAINTENANCE EQUIPMENT	
22.	6.	2.	1.	MAINTENANCE EQUIPMENT	
22.	6.	2.	2.	SPECIAL HEATING SYSTEMS(START-UP, TRACE, ETC.)	
22.	6.	3.	1.	COOLANT RECEIVING, STORAGE & MAKE-UP SYSTEMS	
22.	6.	4.	1.	GAS SYSTEMS	
22.	6.	5.	1.	BUILDING VACUUM SYSTEMS	
22.	6.	5.	2.	OTHER REACTOR PLANT EQUIPMENT	12.410
22.	7.	1.	1.	REACTOR I&C EQUIPMENT(BURN CONTROL, DIAGNOSTICS, ETC.)	
22.	7.	2.	1.	RADIATION MONITORING SYSTEMS	
22.	7.	3.	1.	ISOLATED INDICATING & RECORDING GAUGES, ETC.	
22.	7.	3.	2.	INSTRUMENTATION & CONTROL(I&C)	16.000
22.	98.			SPARE PARTS ALLOWANCE	20.363
22.	99.			CONTINGENCY ALLOWANCE	61.089
22.				REACTOR PLANT EQUIPMENT	488.710

23. 1. 1.	TURBINE-GENERATORS & ACCESSORIES	
23. 1. 2.	FOUNDATIONS	
23. 1. 3.	STANDBY EXCITERS	
23. 1. 4.	LUBRICATING SYSTEM	
23. 1. 5.	GAS SYSTEMS	
23. 1. 6.	REHEATERS	
23. 1. 7.	SHIELDING	
23. 1. 8.	WEATHER-PROOF HOUSING	
23. 1.	TURBINE-GENERATORS	60.860
23. 2.	MAIN STEAM (OR OTHER FLUID) SYSTEM	
23. 3. 1.	WATER INTAKE COMMON FACILITIES	
23. 3. 2.	CIRCULATING WATER SYSTEMS	
23. 3. 3.	COOLING TOWERS	
23. 3. 4.	OTHER SYSTEMS WHICH REJECT HEAT TO THE ATMOSPHERE	
23. 3.	HEAT REJECTION SYSTEMS	12.682
23. 4. 1.	CONDENSERS	
23. 4. 2.	CONDENSATE SYSTEM	
23. 4. 3.	GAS REMOVAL SYSTEM	
23. 4. 4.	TURBINE BY-PASS SYSTEMS(EXCL. PIPING)	
23. 4.	CONDENSING SYSTEMS	7.004
23. 5. 1.	REGENERATORS & RECUPORATORS	
23. 5. 2.	PUMPS	
23. 5. 3.	TANKS	
23. 5.	FEED HEATING SYSTEM	10.404
23. 6. 1.	TURBINE AUXILIARIES	
23. 6. 2.	AUXILIARIES COOLING SYSTEM(EXCL. PIPING)	
23. 6. 3.	MAKE-UP TREATMENT SYSTEM(EXCL. PIPING)	
23. 6. 4.	CHEMICAL TREATMENT & CONDENSATE PURIFICATION SYSTEMS	
23. 6. 5.	CENTRAL LUBRICATION SERVICE SYSTEM(EXCL. PIPING)	
23. 6.	OTHER TURBINE PLANT EQUIPMENT	63.920
23. 7.	INSTRUMENTATION & CONTROL(I&C) EQUIPMENT	1.972
23. 98.	SPARE PARTS ALLOWANCE	.157
23. 99.	CONTINGENCY ALLOWANCE	
23.	TURBINE PLANT EQUIPMENT	156.999

24. 1. 1.	GENERATOR CIRCUITS	
24. 1. 2.	STATION SERVICE	
24. 1.	SWITCHGEAR	4.760
24. 2. 1.	STATION SERVICE & STARTUP TRANSFORMERS	
24. 2. 2.	LOW VOLTAGE UNIT SUBSTATION & LIGHTING TRANSFORMERS	
24. 2. 3.	BATTERY SYSTEM	
24. 2. 4.	DIESEL ENGINE GENERATORS	
24. 2. 5.	GAS TURBINE GENERATORS	
24. 2. 6.	MOTOR GENERATOR SETS	
24. 2.	STATION SERVICE EQUIPMENT	9.384
24. 3. 1.	MAIN CONTROL BOARD FOR ELECTRIC SYSTEM	
24. 3. 2.	AUXILIARY POWER & SIGNAL BOARDS	
24. 3.	SWITCHBOARDS (INCL. HEAT TRACING)	3.128
24. 4. 1.	GEN. STATION GROUNDING SYSTEM & CATHODIC PROTECTION	
24. 4.	PROTECTIVE EQUIPMENT	.109
24. 5. 1.	CONCRETE CABLE TUNNELS, TRENCHES & ENVELOPES	
24. 5. 2.	CABLE TRAYS & SUPPORT	
24. 5. 3.	CONDUIT	
24. 5. 4.	OTHER STRUCTURES	
24. 5.	ELECTRICAL STRUCTURES & WIRING CONTAINERS	1.265
24. 6. 1.	GENERATOR CIRCUITS WIRING	
24. 6. 2.	STATION SERVICE POWER WIRING	
24. 6. 3.	CONTROL WIRING	
24. 6. 4.	INSTRUMENT WIRING	
24. 6. 5.	CONTAINMENT PENETRATIONS	
24. 6.	POWER & CONTROL WIRING	9.466
24. 7. 1.	REACTOR BUILDING LIGHTING	
24. 7. 2.	TURBINE BUILDING LIGHTING	
24. 7. 3.	REACTOR AUXILIARIES BUILDING LIGHTING	
24. 7. 4.	RADIOACTIVE WASTE BUILDING LIGHTING	
24. 7. 5.	FUEL STORAGE BUILDING LIGHTING	
24. 7. 6.	MISCELLANEOUS BUILDINGS LIGHTING	
24. 7. 7.	YARD LIGHTING	
24. 7.	ELECTRICAL LIGHTING	57.120
24. 98.	SPARE PARTS ALLOWANCE	
24. 99.	CONTINGENCY ALLOWANCE	
24.	ELECTRIC PLANT EQUIPMENT	85.231

25. 1. 1.	CRANES, HOISTS, MONORAILS, & CONVEYORS	
25. 1. 2.	RAILWAY	
25. 1. 3.	ROADWAY EQUIPMENT	
25. 1. 4.	WATERCRAFT	
25. 1. 5.	VEHICLE MAINTENANCE EQUIPMENT	
25. 1.	TRANSPORTATION & LIFTING EQUIPMENT	4.150
25. 2. 1.	AIR SYSTEMS(EXCL. PIPING)	
25. 2. 2.	WATER SYSTEMS(EXCL. PIPING)	
25. 2. 3.	AUXILIARY HEATING BOILERS(EXCL. PIPING)	
25. 2.	AIR & WATER SERVICE SYSTEMS	7.700
25. 3. 1.	LOCAL COMMUNICATIONS SYSTEMS	
25. 3. 2.	SIGNAL SYSTEMS	
25. 3.	COMMUNICATIONS EQUIPMENT	.300
25. 4. 1.	SAFETY EQUIPMENT	
25. 4. 2.	SHOP, LABORATORY, & TEST EQUIPMENT	
25. 4. 3.	OFFICE EQUIPMENT & FURNISHINGS	
25. 4. 4.	CHANGE ROOM EQUIPMENT	
25. 4. 5.	ENVIRONMENTAL MONITORING EQUIPMENT	
25. 4. 6.	DINING FACILITIES	
25. 4.	FURNISHINGS & FIXTURES	.653
25.98.	SPARE PARTS ALLOWANCE	
25.99.	CONTINGENCY ALLOWANCE	1.920
25.	MISCELLANEOUS PLANT EQUIPMENT	15.364
26. 1.	REACTOR COOLANT	16.864
26. 2.	INTERMEDIATE COOLANT	9.724
26. 3.	TURBINE CYCLE WORKING FLUIDS	
26. 4.	OTHER MATERIALS	1.472
26.98.	SPARE PARTS ALLOWANCE	
26.99.	CONTINGENCY ALLOWANCE	
26.	SPECIAL MATERIALS	28.060

FUSION REACTOR ECONOMIC EVALUATION (VER. 1.2)

DESIGNATION: FAST LINER REACTOR LY

DATE: 78/10/11.

ACC. NO.	ACCOUNT TITLE	MILLION DOLLARS
20.	LAND & LAND RIGHTS	2.500
21.	STRUCTURES & SITE FACILITIES	167.987
22.	REACTOR PLANT EQUIPMENT	488.710
23.	TURBINE PLANT EQUIPMENT	156.999
24.	ELECTRIC PLANT EQUIPMENT	85.231
25.	MISCELLANEOUS PLANT EQUIPMENT	15.364
26.	SPECIAL MATERIALS	28.060
90.	TOTAL REACTOR DIRECT CAPITAL COST	944.850
91. 1.	TEMPORARY FACILITIES	
91. 2.	CONSTRUCTION EQUIPMENT	
91. 3.	CONSTRUCTION SERVICES	
91.	CONSTRUCTION FACILITIES, EQUIPMENT & SERVICES (15%)	141.728
92.	ENGINEERING & CONSTRUCTION MANAGEMENT SERVICES (15%)	141.728
93. 1.	TAXES & INSURANCE	
93. 2.	STAFF TRAINING & PLANT STARTUP	
93. 3.	OWNER'S G&A	
93.	OTHER COSTS (5%)	47.243
94.	INTEREST DURING 10 YEAR CONSTRUCTION (10% /YR. = 64.4%)	821.453
95.	ESCALATION DURING 10 YEAR CONSTRUCTION (5% /YR. = 33.8%)	431.135
99.	TOTAL REACTOR CAPITAL COST	2528.136

THERMAL POWER (Mwth)	= 3400.00	DIRECT INVESTMENT COST (\$/KWE)	= 929.97
GROSS ELECTRIC POWER (MWE)	= 1360.00	TOTAL INVESTMENT COST (\$/KWE)	= 2488.32
NET ELECTRIC POWER (MWE)	= 1016.00	CAPITAL RETURN 15% (MILLS/KWEH)	= 50.33
1/RECIRCULATING POWER FRACTION	= 3.95	OPERATING 2% (MILLS/KWEH)	= 6.71
PLANT FACTOR	= .85	POWER COST (MILLS/KWEH)	= 57.04

REFERENCES

1. J. W. Shearer and W. C. Condit, "Magnetically Driven Liner for Plasma Compression," Energy Storage, Compression and Switching (1976) (Plenum Publishing Corporation, NY, 1977), p.105.
2. S. G. Alikhanov, V. P. Bakhtin, W. M. Brusnikin, I. S. Glushkov, R. Kh. Kurtmullaev, and A. L. Lunin, "Studies of Models of Thermonuclear Systems," Proc. 6th International Conf. on Plasma Physics and Controlled Nuclear Fusion, IAEA-CN-35/14, Berchtesgaden, FRG October 1976.
3. D. L. Book, A. L. Copper, R. Ford, D. Hammer, D. J. Jenkins, A. E. Robson, and P. J. Turchi, "Stabilized Imploding Liner Fusion Systems," Proc. 6th Int. Conf. on Plasma Physics and Controlled Nuclear Fusion Research, Berchtesgaden, FRG, October 1976 (IAEA, Vienna, to be published).
4. C. Rioux and C. Jablon, "Losses of a Thermonuclear Plasma Imploded by a High-Velocity Wall," Nucl. Fusion 15, 425 (1975).
5. A. R. Sherwood, B. L. Freeman, R. A. Gerwin, T. R. Jarboe, R. A. Krakowski, and R. C. Malone, "Fast Liner Proposal," Los Alamos Scientific Laboratory report LA-6707-P (August 1977).
6. S. G. Alikhanov, V. G. Belan, A. I. Ivanchenko, V. N. Karasjuk, and G. N. Kichigin, "The Production of Pulsed Megagauss Fields by Compression of the Metallic Cylinder in Z-Pinch Configuration," J. Scientific Instruments (J. Phys. E.), Series 2 1, 543 (1963).
7. A. Barcilon, D. L. Book, and A. L. Cooper, "Hydrodynamic Stability of a Rotating Liner," Phys. Fluids 17, 9, 1707 (1974).
8. B. R. Suydam, "Another Look at the Buckling Instability," personal communication, Los Alamos Scientific Laboratory (1977).
9. R. A. Krakowski and R. W. Moses, "Energy-Balance and Blast Containment Considerations for FLR," Los Alamos Scientific Laboratory (unpublished data) (1977).
10. R. A. Krakowski, R. W. Moses, R. L. Miller, and R. A. Gerwin, "Fusion Power from Fast Imploding Liners," IAEA Conf. and Workshop on Fusion Reactor Design, Madison, WI, October 10-21, 1977.
11. R. W. Moses, R. A. Krakowski, and R. L. Miller, "Fast-Imploding-Liner Fusion Power," Proc. 3rd ANS Meeting on the Technology of Controlled Nuclear Fusion, Santa Fe, NM, May 9-11, 1978.
12. R. J. Burke, "Outline for a Large-Pulse Electron-Beam Ignited Fusion Reactor," Los Alamos Scientific Laboratory internal document (1974).
13. T. A. Oliphant and G. E. Gryczkowski, personal communication, Los Alamos Scientific Laboratory (1977).
14. S. I. Braginskii, "Transport Phenomena in a Completely Ionized Two-Temperature Plasma," Sov. Phys. JETP 6 (33), 358-369 (February 1958).

15. S. Glasstone and R. H. Lovberg, Controlled Thermonuclear Reactions: An Introduction to Theory and Experiment (Van Nostrand Reinhold Co., New York, 1960) p. 31.
16. T. R. Jarboe, personal communication, Los Alamos Scientific Laboratory (May 1977).
17. R. A. Gerwin and R. C. Malone, "Theory of Plasma Heating by Fast Liner Implosion," submitted to Nucl. Fusion (1977).
18. V. N. Mineev and E. V. Savinov, "Viscosity and Melting Point of Aluminum, Lead, and Sodium Chloride Subjected to Shock Compression," Sov. Phys. JETP 25, 411 (1967).
19. A. R. Sherwood, personal communication, Los Alamos Scientific Laboratory (1978).
20. M. L. Wilkins and M. W. Guinan, "Impact of Cylinders on a Rigid Boundary," J. Appl. Phys. 44, 1200 (1973).
21. C. M. Fowler, W. B. Garn, and R. S. Caird, "Production of Very High Magnetic Fields by Implosion," J. Appl. Phys. 31, 588 (1960).
22. C. M. Fowler, R. S. Caird, W. B. Garn, and D. B. Thomson, "The Los Alamos Flux Compression Program from its Origin," R. S. Caird, W. B. Garn, D. B. Thomson, and C. M. Fowler, "A Cylindrical Explosive Flux-Compression System," D. B. Thomson, R. S. Caird, W. B. Garn, and C. M. Fowler, "Plasma Compression by Explosively Produced Magnetic Fields, all in Proceedings of the Conference on Megagauss Magnetic Field Generation by Explosives and Related Experiments, H. Knoepfel and F. Herlack, Eds., Frascati, Italy, September 1965 (Euratom, Brussels, 1966, report EUR 2750.e).
23. R. A. Gerwin, personal communication, Los Alamos Scientific Laboratory (March 1978).
24. R. A. Gerwin and R. W. Moses, "Plasma Heating and Fusion Energy Production by a Z-Pinch Driven Compressible Liner," Los Alamos Scientific Laboratory, to be published.
25. J. Marshall and I. Hennins, "Fast Plasma from a Coaxial Gun," Plasma Phys. and Controlled Nucl. Fusion Res. II, 449, IAEA, Vienna (1966).
26. R. A. Gross, Y. G. Chen, E. Halmoy, and R. Moriette, "Strong Shock Waves," Phys. Rev. Lett. 25, 575 (1970).
27. T. R. Jarboe and W. R. Baker, "Apparatus for Producing Laser Targets of 50 Micron Deuterium Pellets," Rev. Sci. Instrum. 45, 431 (1974).
28. G. C. Vlases, personal communication, University of Washington (1978).
29. L. E. Thode, personal communication, Los Alamos Scientific Laboratory (1978).

30. R. E. Stillwagon, "Design Study of Reversible Energy Storage and Transfer for the Reference Theta-Pinch Reactor," Westinghouse Electric Corporation Report EM-4620 (September 1974).
31. LASL Group TD-6, "MCNP-A General Monte Carlo Code for Neutron or Photon Transport, Los Alamos Scientific Laboratory report LA-7396-M (July 1978).
32. L. Dresner, "Mechanical Stress in the Pressure Vessel of a Lithium-Filled, Exploding Pellet, Thermonuclear Reactor," Oak Ridge National Laboratory report ORNL-TM-4050 (1973).
33. A. P. Fraas, "The BLASCON - An Exploding Pellet Reactor," Oak Ridge National Laboratory report ORNL-TM-3231 (July 1971).
34. I. Q. Bohachevsky, personal communication, Los Alamos Scientific Laboratory (1978).
35. T. R. Neal and R. H. Barnes, personal communication, Los Alamos Scientific Laboratory (1977).
36. R. W. Moses, "Flywheel Energy Storage," Phys. Today 15 (October 1975).
37. C. L. Longmire, Elementary Plasma Physics (Interscience Publishers, NY, 1963).
38. S. Timoshenko and J. N. Goodier, Theory of Elasticity, 2nd Ed. (McGraw-Hill Book Co., Inc., 1951).
39. W. Fickett, "PAD, A One-Dimensional Lagrangian Hydrocode," Los Alamos Scientific Laboratory report LA-5910-MS (April 1975).
40. L. F. Coffin, "Fatigue at High Temperature - Predictions and Interpretation," Proc. Interim. Mech. Engrs. (London) 188, 109 (1974).
41. S. C. Schulte and J. R. Young, "Fusion Reactor Design Studies-Economic Evaluation Guidelines," Battelle Pacific Northwest Laboratories report PNL-SA-6648 (November 1977).
42. S. C. Schulte and T. L. Willke, "Normalized Fusion Reactor Power Plant Cost Estimates," 3rd ANS Topical Meeting on the Technology of Controlled Nuclear Fusion, Santa Fe, NM May 9-11, 1978.
43. S. C. Schulte, personal communication, (1978).
44. C. A. Kot, "Shock and Blast Loads in Large Pulse, Inertial Confinement Fusion Reactors," Argonne National Laboratory report ANL/CTR/TM-44 (June 1975).
45. N. A. Amherd, "EPRI Alternative Fusion Concepts Evaluation," to be published as EPRI report, 1979).
46. I. R. Lindemuth and T. R. Jarboe, "Initial Numerical Studies of the Behavior of Z-Pinch Plasma Under Liner Implosion Conditions," Nucl. Fusion, 18, 929 (1978).

47. R. Blewett, personal communication, Glenshaw Glass Co., Glenshaw, PA (1977).
48. M. H. Rice, R. G. McQueen, and J. M. Walsh, "Compression of Solids by Strong Shock Waves," in 6 Solid State Physics (Academic Press, Inc., NY, 1958) pp. 1-60.
49. B. D. Trott, J. E. Backofen, J. J. White, III, "The Design, Evaluation and Delivery of a Prototype, Trailer-Mounted Chamber Capable of Complete Containment of the Blast from Forty Pounds of TNT," Final Report Contract No. N00174-74-C-0218, Battelle Columbus Laboratories, September 1975.
50. D. L. Phung, "A Method for Estimating Escalation and Interest During Construction," personal communication, Oak Ridge National Laboratory (October 1977).

Printed in the United States of America. Available from
 National Technical Information Service
 US Department of Commerce
 5285 Port Royal Road
 Springfield, VA 22161

Microfiche \$3.00

001-025	4.00	126-150	7.25	251-275	10.75	376-400	13.00	501-525	15.25
026-050	4.50	151-175	8.00	276-300	11.00	401-425	13.25	526-550	15.50
051-075	5.25	176-200	9.00	301-325	11.75	426-450	14.00	551-575	16.25
076-100	6.00	201-225	9.25	326-350	12.00	451-475	14.50	576-600	16.50
101-125	6.50	226-250	9.50	351-375	12.50	476-500	15.00	601-up	

Note: Add \$2.50 for each additional 100-page increment from 601 pages up.